UC Riverside
UC Riverside Electronic Theses and Dissertations

Title
Physical Layer Characteristics and Techniques for Visible Light Communications

Permalink
https://escholarship.org/uc/item/4q24841s

Author
Cui, Kaiyun

Publication Date
2012

Peer reviewed|Thesis/dissertation

UNIVERSITY OF CALIFORNIA
RIVERSIDE

Physical Layer Characteristics and Techniques for Visible Light Communications

A Dissertation submitted in partial satisfaction
of the requirements for the degree of

Doctor of Philosophy

in

Electrical Engineering

by

Kaiyun Cui

September 2012

Dissertation Committee:

    Dr. Zhengyuan Xu , Chairperson
    Dr. Jay Farrell
    Dr. Jianlin Liu

The Dissertation of Kaiyun Cui is approved:

_____

_____

_____

Committee Chairperson

University of California, Riverside

Acknowledgments

I would like to take this opportunity to express my sincere gratitude to my research advisor, Dr. Zhengyuan Xu, for his persistent support, continuous guidance, and invaluable advice during my Ph.D. study. His rigorous attitude toward scientific research and his approach to solving unexpected problems have helped me formulate my own way of doing research. Without his suggestion, encouragement, patience, and conscientiousness, I wouldn't be able to successfully complete this dissertation. It's been a great pleasure for me to have him as my advisor.

I would like to thank the Department of Electrical Engineering at UC Riverside, especially the members of my dissertation committee, Dr. Jay Farrell and Dr. Jianlin Liu, for their generous support on my dissertation research. Through many discussion sessions with Dr. Farrell, I have learned a lot from his superior talent of grasping the essence of problems and proposing systematic solutions step by step. It has been a valuable experience for me to develop the capability of dealing with problems efficiently. I'm grateful to Dr. Liu's sharp insight and helpful suggestions during my oral qualifying exam which helped me to make this dissertation better.

I would also like to thank Dr. Gang Chen for the joint efforts. During our collaboration, I have learned valuable lessons from his experience in the system integration. I would thank all the team members of the Wireless Information Technology Lab with whom I have shared my happy time, Dr. Ning Liu, Qunfeng He, Dr. Haipeng Ding, Dr. Leijie Wang, Dr. Yiyang Li, Zongyu Dong, Bo Bai, and Li Wang.

Last but not least, I would like to express my deepest gratitude to my family. Thanks for their generous and endless love to me. They are always with me when I go through tough situations and provide encouragement and support to me. Without their

support, this research work would not happen. My dissertation is dedicated to them.

To my parents for all the support.

ABSTRACT OF THE DISSERTATION

Physical Layer Characteristics and Techniques for Visible Light Communications

by

Kaiyun Cui

Doctor of Philosophy, Graduate Program in Electrical Engineering
University of California, Riverside, September 2012
Dr. Zhengyuan Xu , Chairperson

With the rapid development of semiconductor lighting technologies, the light emitting diodes (LEDs) are promising to eventually replace traditional incandescent and fluorescent lamps for their high energy efficiency, environmental friendliness, and long lifetime. Visible light communication (VLC) utilizing lighting LEDs as transmitters has been an emerging research area since its first proposal. Ubiquitous communication coverage will become possible with wide deployment of lighting LEDs.

This thesis studies physical layer characteristics of VLC systems based on either indoor LED lighting or outdoor LED traffic signaling infrastructure. Advanced communication techniques are proposed to cope with LED bandwidth limitations and grant multiple accesses. Their performance is comprehensively analyzed in typical lighting and signaling environments. Firstly, communication link issues are studied. A conversion method from photometric parameters for illumination to radiometric parameters for communication is developed. Two typical VLC links, the line-of-sight (LOS) link and non-line-of-sight (NLOS) diffuse link, are characterized both experimentally and numerically. Some optional reverse link provisions are evaluated for a full duplex system. Different noise sources and background interferences are analyzed, and dominant noises

are identified under typical application scenarios. With identified signal propagation and noise characteristics, link performance is then evaluated. Secondly, transceiver design techniques to increase the data rate are proposed, including digital pre-equalization techniques and the optical orthogonal frequency division multiplexing (O-OFDM) whose peak to average power ratio (PAPR) issue is investigated. Thirdly, the capacity of the multiple-input multiple-output (MIMO) VLC system exploring inherent multiple LED transmitters and multiple photodetectors is evaluated. The effects of some system parameters involved in non-imaging and imaging transceivers are analyzed. Finally, a combined wavelength-division and code-division multiple access (WD-CDMA) scheme for indoor VLC scenario is proposed. Its performance is analyzed theoretically and then evaluated using the Monte-Carlo simulation.

Contents

List of Figures

List of Tables

Chapter 1

Introduction

1.1 Background

With the demand for ubiquitous connectivity–wireless data delivery anytime and anywhere for everyone, there has been an explosive increase of handheld devices for information exchange. Hundreds of millions of people send and receive messages and files via laptops, PDAs and other digital devices using Wi-Fi or cellular networks, the radio-frequency (RF) based wireless access technology. More and more users enjoy the convenience of employing wireless mobile devices anywhere, both indoors and outdoors. At the same time, manufacturers are installing wireless communication capabilities in stationary electronic devices and appliances to enable consumers to communicate with them remotely. Increasingly, these users also want to access broadband services without the fixed wire links. But traditional RF technologies suffer from insufficient transmission rate and channel capacity because of the limited availability of radio bandwidth in desired frequency ranges [1], while the volume and size of data files continue to increase exponentially, such as the wireless access of Web-based multimedia services, as well as television and movies on demand [2].

1

An intriguing alternative is the optical wireless technology. Rather than transmitting radio waves, optical wireless local area networks send data in modulated beams of white or infrared light–the latter being the same invisible wavelength found in TV remote controls. Optical systems can connect wireless digital devices to a data port on the infrastructure, which in turn can be hooked into whatever high-speed broadband data network serves a house or building. Compared with its radio wave counterpart, the optical wireless band is unlicensed and free of charge. The available bandwidth is much larger than that in traditional radio frequency communication systems and therefore high data rate communication can be achieved. Besides, since the optical wireless communication utilizes carrier in the optical frequency band, which has no overlap with the traditional radio frequency band, no electromagnetic interference is introduced to the existing radio frequency communication systems.

1.1.1 Comparison between optical wireless and RF systems

The optical waves are absorbed by dark objects, diffusely reflected by light-colored objects, and directionally reflected from shiny surfaces. Also it could penetrate through glass, but not through walls or other opaque barriers. So the indoor transmissions are confined to a room. This signal confinement makes it easy to secure transmissions against casual eavesdropping, and prevents interference between links operating in different rooms. Thus, the indoor communication systems can potentially achieve a very high aggregate capacity, and their design may be simplified, since transmissions in different rooms need not be coordinated.

Different from traditional RF systems where phase or frequency modulation with coherent detection is adopted widely, the short range optical wireless communication systems we focus on usually utilize intensity modulation / direct detection (IM/DD).

Table 1.1: Comparison of radio and optical wireless links.

Property of medium	Radio	Optical wireless
Bandwidth regulated?	Yes	No
Capability to pass through opaque objects	Yes	No
Multipath fading?	Yes	No
Multipath distortion	Yes	Yes
Path loss	High	High
Input $X(t)$ represents	Amplitude	Power
SNR proportional to	$\int |X(t)|^2 dt$	$\int |X(t)|^2 dt$
Average power proportional to	$\int |X(t)|^2 dt$	$\int |X(t)| dt$

This is mainly determined by the nature of optical carriers generated at the transmitting devices, for example light emitting diodes (LED). Compared with the single-frequency radio wave carriers, the adopted optical carriers are often incoherent light waves with a certain optical bandwidth, lacking a determined phase or frequency. Detailed characteristics of such IM/DD channels are illustrated in Section 1.1.3. For such IM/DD systems, the short carrier wavelength and large-area, square-law detector lead to efficient spatial diversity that prevents multipath fading. By contrast, radio links are typically subject to large fluctuations in received signal magnitude and phase. Freedom from multipath fading greatly simplifies the design of the optical wireless links. However, the signal to noise ratio (SNR) of a direct detection receiver is proportional to the square of the received optical power, implying that IM/DD links can tolerate only a comparatively limited path loss. The characteristics of radio and optical wireless links are compared in Tab. 1.1.

Radio and optical wireless are complementary transmission media, with different applications favoring the use of one medium over the other. Radio is favored in applications where user mobility must be maximized or transmission through walls or over a long range is desired. Optical wireless is favored for short to medium-range applications in which per-link bit rate and aggregate system capacity must be maximized at minimal cost or receiver signal-processing complexity.

1.1.2 Typical optical wireless links

An optical wireless link can be classified into two categories, as shown in Fig. 1.1 [3]. The first category is the line-of-sight (LOS) link, where a transmitter is within the receiver field of view (FOV). The directed link design adopts narrow beam angle transmitters and small FOV receivers, maximizing the power efficiency by minimizing the path loss and reception of ambient light noise. On the other hand, the nondirected link design adopts wide beam angle transmitters and large FOV receivers, alleviating a need for accurate pointing as in the directed link, while at the expense of large path loss. The second category is the non-line-of-sight (NLOS) link, relying generally upon the reflection of the light from the ceiling or some other diffusely reflecting surfaces. Compared with the LOS link, the path loss of the NLOS link is generally much larger, while link robustness and ease of use increase, allowing the link to operate even when barriers, such as people or cubicle partitions, stand between the transmitter and receiver.

1.1.3 IM/DD channel characteristics

Modulation techniques for radio wireless systems include amplitude, phase, and frequency modulation (AM, PM, and FM), as well as some generalizations of these
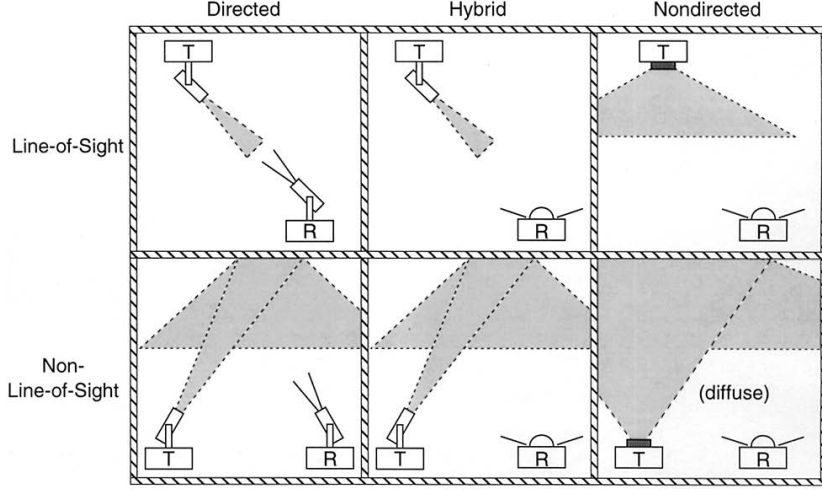
Figure 1.1: Optical wireless communication links.

techniques [4]. A single electromagnetic mode is usually adopted for such modulation and the receiver front-end output is an electrical signal whose voltage is linear in the amplitude of the received carrier electric field. Compared with the RF systems, for the short- and medium-range optical wireless communication systems we considered, it is extremely difficult to collect appreciable signal power in a single electromagnetic mode. Commonly, the IM/DD is adopted, where the desired waveform is modulated onto the instantaneous power of the carrier and a current proportional to the received instantaneous power (proportional to the square of the received electric field) is produced at the receiver.

If we denote the instantaneous optical power of the emitter as the transmitted waveform $X(t)$, the instantaneous current at the receiver as the received waveform $Y(t)$, and the channel impulse response as $h(t)$, the system model could be summarized as

$$Y(t) = RX(t) \otimes h(t) + n(t), \tag{1.1}$$

where $\otimes$ denotes the convolution, R represents the detector responsivity (A/W) and $n(t)$ represents the noise at the receiver. Here the channel is modeled as a baseband

5

linear system, with frequency response represented as

$$H(f) = \int_{-\infty}^{\infty} h(t)e^{-j2\pi ft}dt, \tag{1.2}$$

which is the Fourier transform of $h(t)$. The IM/DD channel differs from conventional RF channels in several aspects. Because the channel input $X(t)$ represents instantaneous optical power, the channel input is nonnegative:

$$X(t) \geq 0 \tag{1.3}$$

and the average transmitted optical power P_t is given by

$$P_t = \lim_{T \to \infty} \frac{1}{2T} \int_{-T}^{T} X(t)dt. \tag{1.4}$$

The average received optical power is given by

$$P = H(0)P_t, \tag{1.5}$$

where the channel dc gain is $H(0) = \int_{-\infty}^{\infty} h(t)dt$. The electrical SNR of a digital link at bit rate R_b can be represented by

$$SNR = \frac{R^2 P^2}{R_b N_0} = \frac{R^2 H^2(0)P_t^2}{R_b N_0} \tag{1.6}$$

assuming that $n(t)$ is dominated by a white Gaussian component having double-sided power spectrum density N_0.

1.2 Motivation

With the development of semiconductor technologies, the cost of optical transmitting and receiving devices has been reduced greatly, providing opportunities for optical wireless communication to be used in daily lives. Commercial-off-the-shelf (COTS) optical transmitters (e.g. light emitting diodes and laser diodes) and receivers (e.g.
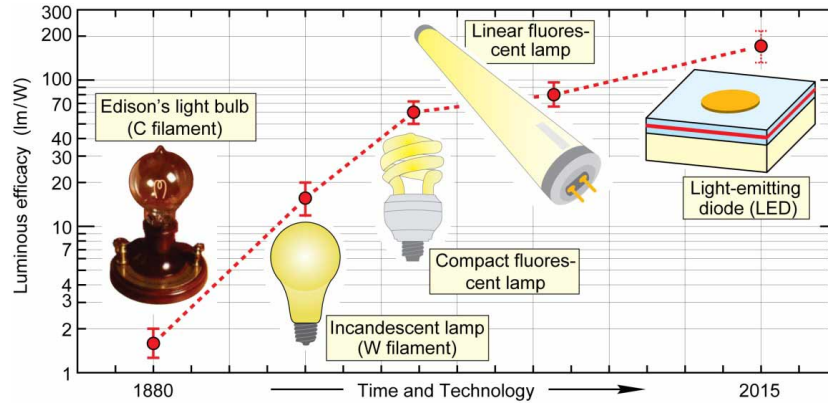
Figure 1.2: Comparison of the luminous efficacy (source efficacy) of conventional lighting technologies with the light-emitting diode technology.

photodiodes, avalanche photodiodes, photomultiplier tubes, and image sensors), have become economically available. Among those semiconductor devices, one important category is LED, especially high power lighting LEDs. It's anticipated that LED will replace the existing incandescent and fluorescent lamps to be the fourth generation light source in the near future [5], as shown in Fig. 1.2. Compared with traditional light sources, LEDs have the advantages of longer life expectancy, high lighting efficacy, no out-of-visible band optical spectrum (unlike incandescent lamps with huge infrared spectrum light and fluorescent lamps with additional ultraviolet spectrum), easy maintenance, and environmental friendliness.

One unique characteristic of the LEDs that differentiates them from the traditional light sources is that it can be modulated at a relatively high rate, enabling data transmission by the LED transmitters. With the popularization of LED lighting fixtures to provide both indoor and outdoor illumination and traffic signaling, visible light communicatoin (VLC) piggybacked on those systems can be realized to provide ubiquitous internet access for mobile users or communication among vehicles and roadside infrastructure. With the combination of the lighting or signaling and the communication

systems, the cost of setting up a VLC system can be largely reduced because no other transmitting devices need to be installed.

Besides the cost effectiveness, VLC has another advantage compared with the infrared communication. It's required that a certain limit for the transmission power of the infrared light sources is set in order to guarantee human skin safety for people residing in the infrared communication area. In comparison, no transmission power limit is set for the visible light LED sources because no potential hazard is introduced by the visible light to the human body. Meanwhile, because the VLC system is usually piggybacked on an illumination or signaling system, a minimum transmitted optical power is usually required to maintain a certain illumination level. This could result in a high SNR at the receiver, an advantage that can be taken to boost the communication data rate and improve the communication system performance.

Since its first proposal in 1999 using visible light LED for audio transmission [6], VLC has been an emerging research area, attracting more and more interests from academic researchers. A visible light communication consortium (VLCC) was established in Japan in November 2003 to promote the VLC applications [7]. Recently, a corresponding IEEE standard has also been published regulating some of the PHY and MAC layer specifications [8]. Based on its application scenarios, two different VLC systems with different physical layer characteristics are promising in the future. The first is the indoor lighting combined VLC with the intention to provide high speed internet access for mobile users inside an office or home. The second is the LED traffic light based VLC for the development of intelligent transportation systems (ITSs).

The indoor lighting combined VLC was firstly proposed by Komine *et. al.* in 2004 [9], with fundamental analysis of the receiver SNR in a typical indoor lighting environment. Following Komine's work, investigation of the potentials for high-speed

transmission using commercially available "single-chip" white-light LEDs in a moderate-size office, with both baseband and discrete multitone (DMT) modulation was carried out [10]. The problem of non-uniform time of arrival (TOA) of all transmitting light sources was investigated and a cooperative transmission scheme was proposed [11]. The feasibility of optical wireless communication links using high-brightness illumination LEDs was then experimentally verified [12, 13, 14, 15]. Simulation software was also developed for basic system design of the indoor lighting combined VLC [16].

The indoor VLC channel characteristics have been studied theoretically in [10, 17, 18]. To improve the limited modulation bandwidth of a white LED, analog pre-equalization techniques have been proposed [19, 20, 21]. Post-equalization at the receiver to overcome the intersymbol interference (ISI) and improve the data rate has also been discussed [17, 22, 23]. With the desire for high data rate communication capability, orthogonal frequency division multiplexing (OFDM) has been applied [24, 25, 26, 27, 28, 29]. LED nonlinearity effects on the OFDM systems have been investigated as well [30, 31, 32, 33]. As an alternative approach to boost the communication data rate, optical multiple-input multiple-output (MIMO) applied in the indoor lighting combined VLC systems was also proposed, including both a non-imaging MIMO system and an imaging MIMO system [34].

The outdoor LED traffic light based VLC was first proposed by Akanegawa *et. al.* in 2001 [35], where the performance of the link between an LED traffic light and a vehicle-equipped photodiode receiver was investigated. Optimization of the design parameters was discussed in [36]. A receiver to mitigate the effects of background solar radiation was proposed [37]. An implementation of an outdoor VLC system utilizing LED traffic lights and a photodiode was carried out [38]. Besides using a photodiode as the detector, an image sensor based outdoor VLC system has also been proposed and

investigated [39, 40, 41]. A new receiving front-end combining both an image sensor and a photodiode was also proposed in [42, 43].

1.3 Challenges

In spite of the advantages as mentioned in the previous sections, several challenges exist impeding VLC from being applied widely in real scenarios. The first challenge is to achieve high data rates using a lighting LED with limited modulation bandwidth. The second is the selection of an appropriate uplink solution to achieve full duplex communication, as a VLC channel is a natural broadcast channel. Several options have been proposed [44, 45, 46], and their properties need to evaluated in order to determine the best choice in different application scenarios. In addition, there are specific challenges of standardization and regulation for VLC. VLC systems must be compatible with standards for lighting and control of lighting systems under development, as communication is a subsidiary function. During the system design, such a lighting control function must be taken into consideration.

1.4 Contributions and Thesis Organization

The major contributions of this dissertation focus on the physical layer characterization of both indoor lighting combined and outdoor LED traffic light based VLC systems, as well as corresponding transceiver design techniques based on the physical layer characteristics. For indoor lighting combined VLC systems, the major contributions can be summarized as follows.

First, systematic characterization of indoor VLC channels is conducted, including both the LOS and the NLOS channels. For the LOS channel, a theoretical

model is proposed with experimental validation. The NLOS diffuse channel is mainly characterized using the experimental measurements to validate the computer simulation results. Up to now, the indoor NLOS VLC channels have been characterized only through Monte Carlo computer simulation. Corresponding experimental validation is absent from the literature. In this thesis, experimental characterization of the channel impulse response is introduced and the obtained results are reported compared with corresponding simulation results.

Second, the capacities of both the non-imaging and imaging MIMO channels in a typically illuminated office environment are investigated. Although both systems were proposed for indoor VLC in [34], the capacity analysis was absent, which is a vital parameter in evaluating the performance improvement against the single-input single-output (SISO) link.

Third, a combined wavelength division and code division multiple access (WD-CDMA) scheme is proposed for simultaneous multiuser access. To the author's best knowledge, most of the research work on the indoor VLC system design has been focused on the single user link. Little effort has been devoted to the investigation of an appropriate multiuser access scheme.

For the outdoor LED traffic light based VLC, this dissertation focuses on the photodiode receiver front-end based link. The major contribution includes empirical link characterization, comprised of the transmitter performance, background interference, LOS link validation, as well as link performance analysis based on the measurement results. Most of the related work so far has addressed issues in theoretical system design using ideal models [35, 36, 37]. No systematic empirical link characterization using commercial-off-the-shelf (COTS) LED traffic lights has been carried out.

The remainder of this thesis is organized as follows.

In Chapter 2, a typical indoor single-user VLC link is characterized from several aspects. The conversion is first introduced from a set of LED photometric parameters, common for lighting performance evaluation, to that of radiometric parameters for communication performance evaluation. Indoor channels are then characterized, including both the LOS channel and NLOS diffuse channel. The typical noise sources in a VLC system are introduced, facilitating to identify the dominant noise sources in different application scenarios. Several potential options for the system uplink to achieve full duplex communication are then discussed, comparing their performance from different aspects. Finally, a point-to-point demonstration system is shown to validate the feasibility of the VLC system.

In Chapter 3, some data rate improvement techniques are discussed, including transmitter equalization, OFDM modulation, and optical MIMO. A new pre-equalization technique using digital filters with performance evaluation is introduced and compared with previously proposed analog pre-equalization techniques [19, 20, 21]. The probability distribution of the peak to average power ratio (PAPR) is investigated for the application of OFDM in VLC systems, aiding the design of the modulation parameters. At last, the capacities of both the non-imaging and imaging indoor VLC MIMO systems are investigated, revealing the effects of different system parameters on the channel capacity, such as receiver antenna separation and the number of transmitting and receiving antennas.

In Chapter 4, a combined wavelength- and code- division multiple access (WD-CDMA) scheme is proposed for simultaneous multi-user access. Here the indoor VLC is also proposed as the physical layer of the emerging femtocell systems, defined as the optical femtocell. Its general system structure is introduced, followed by the theoretical analysis of the system performance. At last, the proposed system performance in a

typically illuminated office environment is revealed by computer simulation, together with the effects of different parameter variations.

In Chapter 5, an LED traffic light based outdoor VLC link utilizing a photodiode receiver front-end is characterized empirically, with the link performance evaluated in practical scenarios. Firstly, the ambient light interference, a major challenge for the outdoor VLC, is characterized empirically by field measurements. Secondly, the performance of COTS LED traffic lights as communication transmitters is characterized, including the input-output relation and the frequency response. Thirdly, the LOS link path loss model we propose is validated by empirical measurements. Finally, the link performance is evaluated based on the measurement results, revealing the range-rate tradeoffs for such a link.

Chapter 6 summarizes the contents of the dissertation and the major results.

Chapter 2

Indoor VLC Link

Characterization

The fundamental element determining the communication system performance and the corresponding transceiver design techniques is the link between a transmitter and a receiver. Such link includes several parts, such as the transceiving device properties, the propagation channel characteristics, the uplink properties, and the typical noise sources. In this chapter, the basic indoor VLC link characteristics are investigated, and a point-to-point demonstration system for feasibility validation is introduced.

2.1 Photometric to Radiometric Parameters Conversion

Photometric parameters are used for the measurement of light in terms of its perceived brightness to the human eye. The human eye can be treated as a photodetector with specific responsivity at different wavelengths, known as the relative luminous efficiency function $V(\lambda)$ to model brightness sensitivity (Fig. 2.1). This function follows the CIE's definition within the visible light spectrum at wavelengths from 380nm
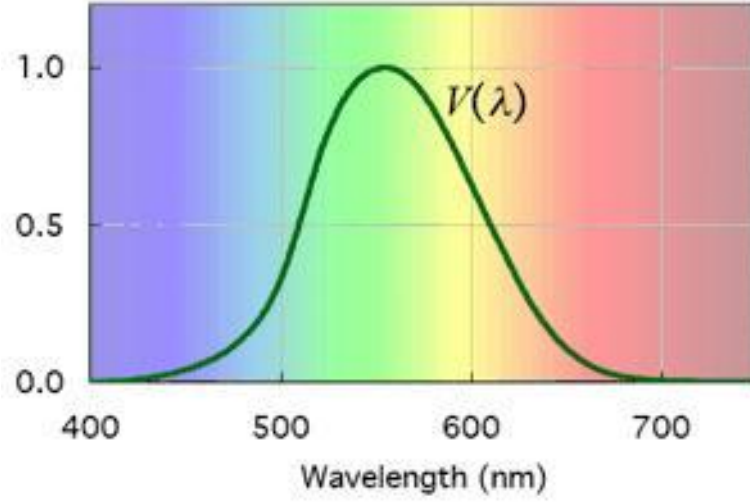
Figure 2.1: Relative luminous efficiency function defined by CIE.

Table 2.1: Photometric Parameters.

Symbol	Quantity	SI unit	Abbr.
F	luminous flux	lumen	lm
I_v	luminous intensity	candela(=lm/sr)	cd
L_v	luminance	candela per square meter	cd/m^2
E_v	illuminance	lux(=lm/m^2)	lx
M	luminous efficiency	lumen per watt	lm/W

to 780nm [47]. One basic photometric parameter is luminous flux F which is just the radiant power weighted by the luminous efficiency function. Many photometric parameters which are listed in Tab. 2.1 are related to the luminous flux that indicates the illumination capability of a light source.

Radiometric parameters of LEDs characterize energy radiation capabilities in terms of absolute power. They do not depend on the specific sensitivity of human eye

15

Table 2.2: Radiometric Parameters.

Symbol	Quantity	SI unit	Abbr.
P	radiant power	watt	W
I	radiant intensity	watt per solid angle	W/sr
E	irradiance	watt per square meter	W/m^2
L	radiance	watt per steradian per square meter	W/(sr·m^2)

and therefore represent the light transmitting capability of a light source spanning wide spectrum. They are distinct from the photometric parameters that only account for the visible band with different weights for various wavelengths. For a communication system using a commercial photodetector at the receiver with a responsivity function different from that of the human eye, we need the radiometric parameters to characterize the receiver output, as detailed in Tab. 2.2. As mentioned earlier, luminous flux F is the radiant power weighted by the luminous efficiency function $V(\lambda)$. Thus the relation between two sets of parameters can be represented as:

$$F = 683 \int_{380nm}^{780nm} S(\lambda)V(\lambda)d\lambda, \tag{2.1}$$

$$P = \int_{\lambda_L}^{\lambda_H} S(\lambda)d\lambda, \tag{2.2}$$

where $S(\lambda)$ is the radiant power spectrum density of the light, λ_L and λ_H are the lower and upper wavelength bounds of the light spectrum, 683 is a scaling factor, F is the luminous flux, and P is the radiant power. The integration limits in eq. (2.1) are determined by the range of $V(\lambda)$ which is only defined in the visible band.

2.2 Indoor Channel Characterization

There exist diverse link connectivity scenarios. For example there is a single LOS link for point to point VLC between PDAs, multiple LOS links from multiple sources to a single spot, a NLOS link for indoor diffused lighting communication and mixed LOS/NLOS link for information broadcasting. In summary, two fundamental links comprising these diverse link connectivity scenarios are the LOS link and the NLOS diffuse link, which will be characterized in this section.

2.2.1 LOS link characterization

The channel impulse response of an LOS link is a time delayed delta function,

$$h(t) = \delta(t - \tau), \tag{2.3}$$

where $\tau = D/c$, D is the distance between the transmitter and receiver and c is the speed of light. The LOS link therefore can be fully characterized by its path loss. We model a general LOS VLC scenario in Fig. 2.2 and evaluate the corresponding path loss that will be used for the communication receiver performance study. Some parameters are defined as follows. The receiver distance to the source is D and the receiver aperture radius is r. The angle from the source-receiver line and receiver normal is α and to the source beam axis is β (viewing angle). Ω_r is the receiver solid angle seen by the transmitter and A_r is the receiver area. They satisfy the relation $A_r \cos(\alpha) \approx D^2 \Omega_r$.

We assume the transmitter LED has the spatial luminous intensity distribution $I_0 g_s(\theta)$, where I_0 is the axial intensity with unit candela and $g_s(\theta)$ is the normalized spatial distribution function usually provided by an LED datasheet from a vendor. If we denote the total transmitted luminous flux of the transmitter LED as F_s, then we

17
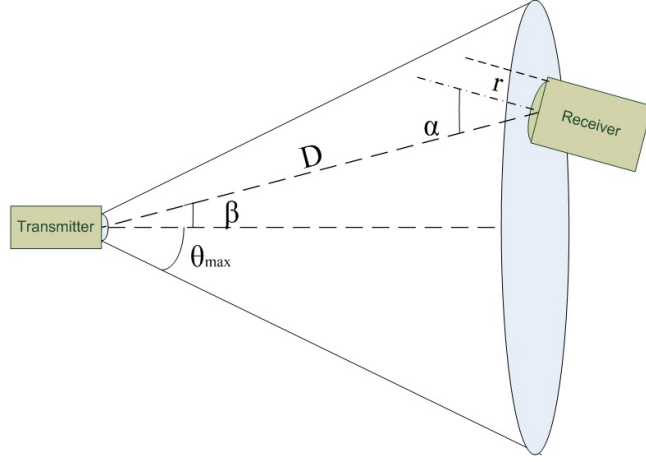
Figure 2.2: LOS link model.

have the relation:

$$F_s = \int_0^{\Omega_{max}} I_0 g_s(\theta) d\Omega = I_0 \int_0^{\theta_{max}} 2\pi g_s(\theta) \sin\theta d\theta, \tag{2.4}$$

where Ω_{max} is the LED beam solid angle, which is related to the LED beam maximum half angle θ_{max} as $\Omega_{max} = 2\pi(1 - \cos\theta_{max})$. Denote the receiver ingested luminous flux as $F_r = I_0 g_s(\beta)\Omega_r$. Thus we can express the luminous path loss as follows:

$$L_L = \frac{F_r}{F_s} = \frac{I_0 g_s(\beta)\Omega_r}{I_0 \int_0^{\theta_{max}} 2\pi g_s(\theta) \sin\theta d\theta} \approx \frac{g_s(\beta) A_r \cos\alpha}{D^2 \int_0^{\theta_{max}} 2\pi g_s(\theta) \sin\theta d\theta}. \tag{2.5}$$

The above path loss is derived in the photometric domain. For short range LOS free space propagation, power path loss is reasonably assumed independent of wavelength λ within the spectrum of interest. Thus it can be written as $L_p = S_r(\lambda)/S_s(\lambda)$ according to eq. (2.2). Then we can conclude from eq. (2.1) that $L_p = L_L$ for fixed $V(\lambda)$.

Many commercial lighting LEDs without any beam shaping component can be treated as Lambertian sources with spatial distribution function $g_s(\theta) = \cos^m(\theta)$, where m is the order of Lambertian emission and is related to the semi-angle at half illuminance of an LED $\Phi_{1/2}$ as $m = -ln2/ln(\cos\Phi_{1/2})$ [48]. If we substitute $g_s(\theta)$ with

the Lambertian emission pattern into eq. (2.5) and set $\theta_{max} = \pi/2$, we can obtain the LOS path loss for the Lambertian source:

$$L_L \approx \frac{(m+1)A_r}{2\pi D^2} \cos\alpha \cos^m(\beta). \tag{2.6}$$

In some lighting applications, a light source is required to have directional emitted light with a narrow beam angle. Beam shaping lens may be mounted in front of the LED core to change the spatial distribution $g_s(\theta)$ of the LED light. In those cases, the Lambertian emission pattern no longer holds and one has to know the reshaped beam spatial distribution function $g_s(\theta)$ in order to calculate the path loss based on eq. (2.5).

The typical set of LED parameters that a vendor provides on the datasheets usually includes total transmitted luminous flux F_s or axial intensity I_0, normalized spatial distribution function $g_s(\theta)$, and normalized radiant power spectrum density $S'_s(\lambda)$. Given the relation between F_s and I_0 in eq. (2.4), they are convertible to each other.

First let's determine the source radiant power spectrum density $S_s(\lambda) = \xi S'_s(\lambda)$, where ξ is the scaling factor. Substituting $S_s(\lambda)$ into eq. (2.1) we find

$$\xi = \frac{F_s}{683 \int_{\lambda_{sL}}^{\lambda_{sH}} S'_s(\lambda)V(\lambda)d\lambda}, \tag{2.7}$$

where λ_{sH} and λ_{sL} are the upper and lower wavelength bounds of the optical source in the visible range. Therefore the power spectrum density at the receiver is $S_r(\lambda) = L_p S_s(\lambda) = \xi L_p S'_s(\lambda)$. Suppose an optical filter with spectral response $R_f(\lambda)$ is placed in front of the photodetector. The received optical power becomes

$$P_r = \int_{\lambda_{rL}}^{\lambda_{rH}} S_r(\lambda)R_f(\lambda)d\lambda, \tag{2.8}$$

where λ_{rH} and λ_{rL} are the upper and lower wavelength bounds of an optical filter at the receiver.

Indoor VLC systems commonly use the intensity-modulation and direct-detection (IM/DD) scheme. When multiple LOS links exist, spatially connecting distributed LEDs to a single receiver, we can easily obtain the total received optical power by summing the received power of all single LOS links within the receiver field of view (FOV), which could be written as:

$$P_{rm} = \sum_{i=1}^{N} P_{ri}, \qquad (2.9)$$

where i denotes the single LOS link index and N is the number of single LOS links determined by the receiver FOV and the relative position and orientation of the transmitter and receiver.

Measurements have been conducted to verify the above derived theoretical results. An LED was chosen from OSRAM Opto Semiconductors with product number LUW W5SM-JYKY-4P7R-Z. Its typical luminous flux is 66 lm at 350 mA under 3.2 V forward voltage. This LED is claimed to be a Lambertian emitter and comparison between the vendor supplied actual radiation pattern and the ideal Lambertian emission pattern with $m = 1$ is shown in Fig. 2.3. The graph reveals great conformity between them except a slight deviation at the tail which may be caused by the package of the LED.

The transmitter LED was mounted on the ceiling with light core facing downward and a receiver was placed on the horizontal plane about 1.9 m under the ceiling, a typical desk height. The calculated received optical power is then compared with the measurement results on the receiver surface for different off-axis angle β in Fig. 2.4. A slight deviation between calculation results based on the vendor datasheets and measurement results may be because the LED's actual performance may offset the datasheets' description.
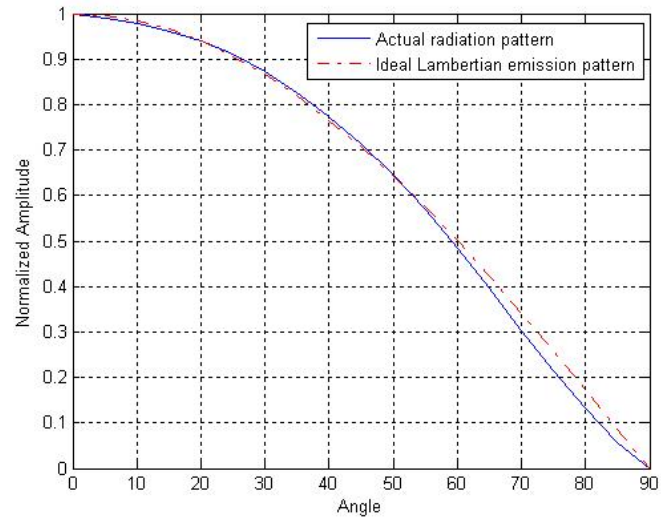
Figure 2.3: Comparison between the actual and ideal Lambertian emission pattern.
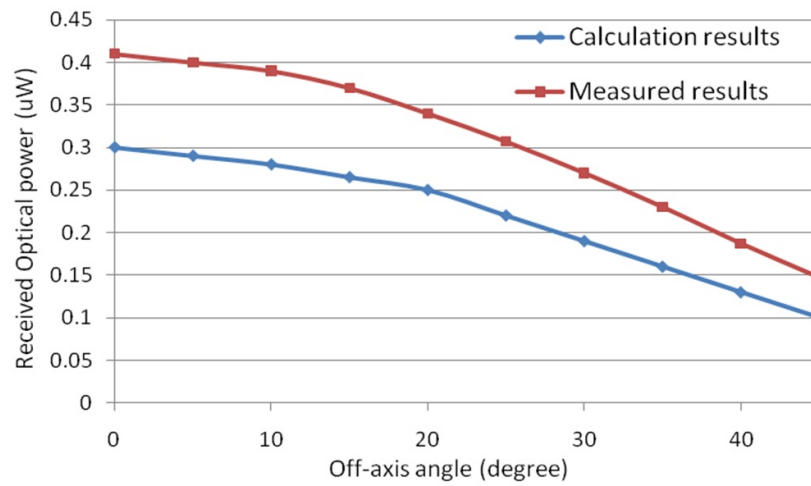
Figure 2.4: Comparison of the calculation and measurement results.

2.2.2   NLOS link characterization

The LOS link has been characterized in the previous section with derivation and validation of its path loss. The LOS channel could provide large bandwidth while maintaining a relatively small path loss. However, such LOS links are susceptible to blockage. Any object between the transmitter and the receiver will cause failure of the communication link. The so called "shadowing" effect of an LOS channel for indoor infrared communication systems has been discussed [49].

In comparison, non-line-of-sight (NLOS) diffuse channels do not suffer from such a blockage problem, because surface diffused light comes from various directions into the receiver. The effect of shadowing on NLOS diffuse channels has been proved to be far less significant than their LOS counterparts for indoor infrared communication [49]. For optical wireless communication employing intensity modulation and direct detection (IM/DD), the much shorter carrier wavelength with large-area, square-law detector leads to efficient spatial diversity that prevents multipath fading [3]. However, the existence of multiple propagation paths introduced by surface reflection does lead to temporal dispersion. Thus drawbacks of NLOS diffuse channels include much larger path loss and smaller bandwidth due to temporal dispersion. For indoor high data rate communication, such temporal dispersion will cause ISI and limit the maximum achievable data rate. Elegant pre- and post-equalization techniques have been designed to both increase the LED bandwidth and mitigate ISI [17, 19, 20, 21, 22, 23]. Therefore characterization of the NLOS diffuse channel is of vital importance for transmitter signaling, design of corresponding post-equalization techniques, and system performance improvement.

NLOS channel characterization can be achieved by two different approaches,

the computer simulation [18, 50, 51] and the experimental measurement. The focus of this section is on the experimental characterization of the NLOS channels, although computer simulation results are also adopted for comparison with the measurement results. Such experimental characterization has been carried out in [49] for indoor infrared communication. Those studies provide adequate guidance to experimental channel characterization for indoor visible light communication, which hasn't been widely studied in the literature yet.

Our experimental characterization procedures will be based on the short pulse technique, which is complementary to that adopted in [49], the CW swept-frequency technique. The remainder of this section is organized as follows. The experimental setup is first introduced. Next, the experimental impulse response results of a typical empty office room are presented. These results are then compared with those obtained from the ray tracing computer simulation [50]. Parameters of the transceiver together with room properties that possibly have an impact on the impulse response are discussed. Subsequently, more experimental results in different real application scenarios are provided, such as an office room with furniture inside, a hallway and a lobby, with the intention to gain an intuitive understanding of the temporal dispersion effects of these channels.

2.2.2.1   Experimental setup

We adopted the most straightforward method in our measurement campaign, a short pulse technique, to characterize the impulse response of the indoor NLOS diffuse channels, i.e., it uses a very short transmitted pulse to directly probe a channel. The system diagram is shown in Fig. 2.5 [52].
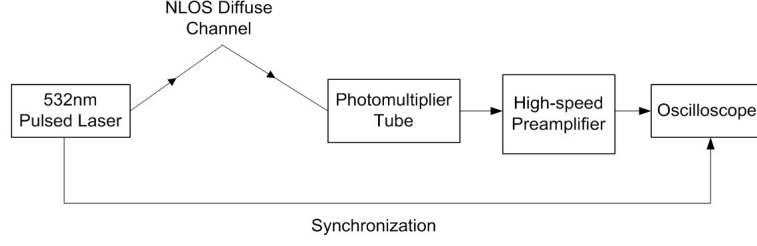
Figure 2.5: System diagram of the experimental setup.

The transmitter was a compact Q-switched fourth harmonic Nd:YAG laser at 532nm. It can emit optical pulses with full width at half maximum (FWHM) of 3~5 ns and energy up to 3~5 mJ per pulse. Pulse shaping components were mounted right in front of the laser output port to reshape the pulse to a desired spatial distribution. At the receiver side, a photomultiplier tube (PMT, Hamamatsu H10304) with a very high gain ($10^5 \sim 10^7$) and an active receiving area of 0.5cm^2 was deployed to receive the diffused optical signal. The output electrical signal was then amplified by a high-speed transimpedance preamplifier with a gain of 34dB and bandwidth of 1.5GHz. The amplified signal was monitored and recorded by a high speed oscilloscope, which was triggered by the synchronization signal from the transmitter laser.

In order to calibrate our NLOS measurement results, a reference LOS channel was created by placing the receiver next to and directly aiming at the transmitter. Since the LOS channel induces a negligible pulse broadening effect in this case, the measured LOS system impulse response can thus well approximate the overall impulse response of involved system components including the laser, PMT and preamplifier. The measured LOS response result is shown in Fig. 2.6. The trough following the main peak was primarily due to the electric discharge in the circuit. This impulse response with FWHM of 6.2ns is mainly introduced by the temporal dispersion of the original laser pulse, the multiple electrode structure of the PMT at high gain, and minor broadening
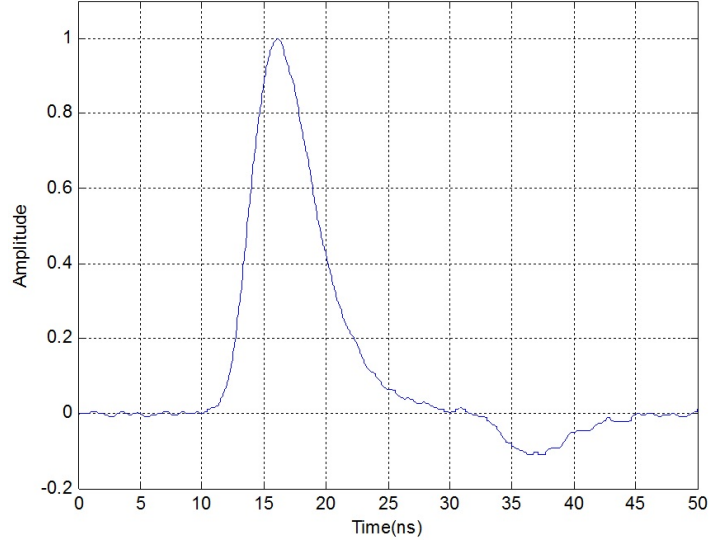
Figure 2.6: Reference system impulse response under a direct LOS channel.

of the preamplifier.

The divergence angle of the transmitted laser beam could be adjusted using a beam shaping component in front of the laser output. With combination of the beam expander and various diffusers and lenses, we were able to control the laser beam pattern and divergence angle. The effects of varying beam patterns and beam angles will be explored in the next part. Meanwhile, the receiver FOV, defined as the full acceptance angle at the receiver in this work, was also controllable by a length-adjustable empty tube in front of the PMT active sensing window. During the experiment, we tested two different (narrow and wide) but representative FOVs of 40^0 and 132^0 respectively, and their effects on the measured impulse response.

2.2.2.2 Typical office room measurement and analysis

In this section, we take a typical empty office room as an example to show some measured impulse response results. The transmitter and receiver configuration

in this less-complex environment allows us to carry out intuitive geometric analyses of the dominant signal reflections that lead to temporal pulse dispersion. The ray tracing computer simulation results are also reported to compare with the measurement results and verify our analysis.

Experimental results

The room configuration is shown in Fig. 2.7. It is a typical office room with length, width, and height of 11.3m, 4m, and 3.06m respectively. The ceiling, one front wall, one back wall, and two side walls are covered with white paint with similar reflectivity, which is measured to be around 80%. There is one big window on one side wall and one glass door on the other side wall, but they are both covered with white blinds, the reflectivity of which was measured to be similar to that of the white wall. The floor is covered with grey carpet with reflectivity measured to be approximately 30%. For ray tracing computer simulation discussed later on, we idealized this room as a cuboid with five faces of the same reflectivity 80% and one face of the reflectivity 30%.

The transmitter and receiver were placed as shown in Fig. 2.7. If we take the lower inner-left corner as the origin as the 3-dimensional Cartesian coordinate system in the figure, the transmitter and receiver (x,y,z) coordinates could be written as (7.74, 1.52, 1.94)m and (4.36, 3.08, 0.87)m respectively. The transmitter and receiver were both set to point directly upward. At this stage the collimated beam of the laser was directed to the ceiling without any beam shaping. It was then diffusely reflected with nearly Lambertian beam characteristics. The measured system impulse responses with receiver FOV of 40^0 (Rx1) and 132^0 (Rx2) are shown below in Fig. 2.8. We can observe that the FWHMs of the impulse responses with Rx1 and Rx2 are 15.3ns and 30.4ns respectively. Compared with the FWHM of 6.2ns of the impulse response induced by
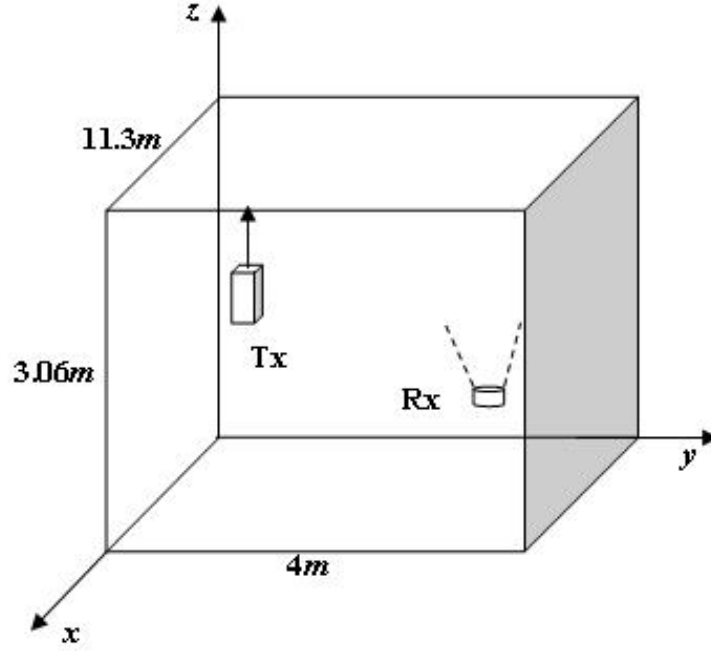
Figure 2.7: One typical office room configuration.

system components, the temporal dispersion induced by the NLOS diffuse channel is significant.

Ray tracing simulation results

Based on geometric calculations, for Rx1 with FOV of 40^0, the receiver FOV cone only intersects with the ceiling outside the beam impinging spot on the ceiling, which can be treated as a near Lambertian diffusion light source. If we define rays emitted from the light spot as the directly diffused beam and further reflections by the room surface as the first reflection, the second reflection, and so on, then no direct diffusion and first order reflection could be accounted for the temporal dispersion. Among those diffused beams from the second and higher order reflections, the third and higher order reflections have much smaller energy, and the temporal dispersion is mainly due to the second reflection.
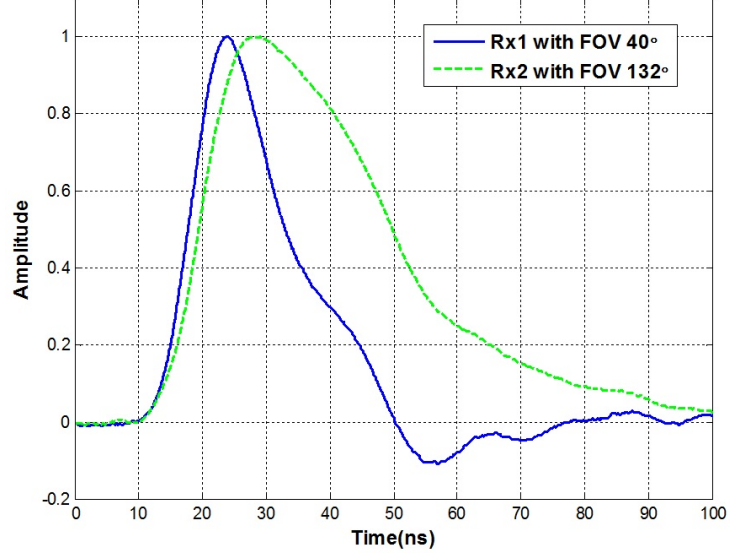
Figure 2.8: System impulse responses with receiver Rx1 and Rx2.

Next, the ray tracing simulation is adopted to verify the analysis. A block diagram showing the process of the ray tracing simulation is shown in Fig. 2.9. A simulated impulse response contributed by the NLOS channel only and without system component effect is shown in Fig. 2.10. The figure clearly reveals the second, third and fourth reflections. We can conclude from this figure that the third and fourth reflections contribute little to the overall impulse response except for the large tail following the main lobe. The amplitude of the tail is negligible. In order to compare with the experimental results that took into account the effects of system components, the simulated channel impulse response was convoluted with the measured LOS system impulse response presented before. The generated result represents the system impulse response including the laser source, NLOS channel, detector and preamplifier, as shown in Fig. 2.11.
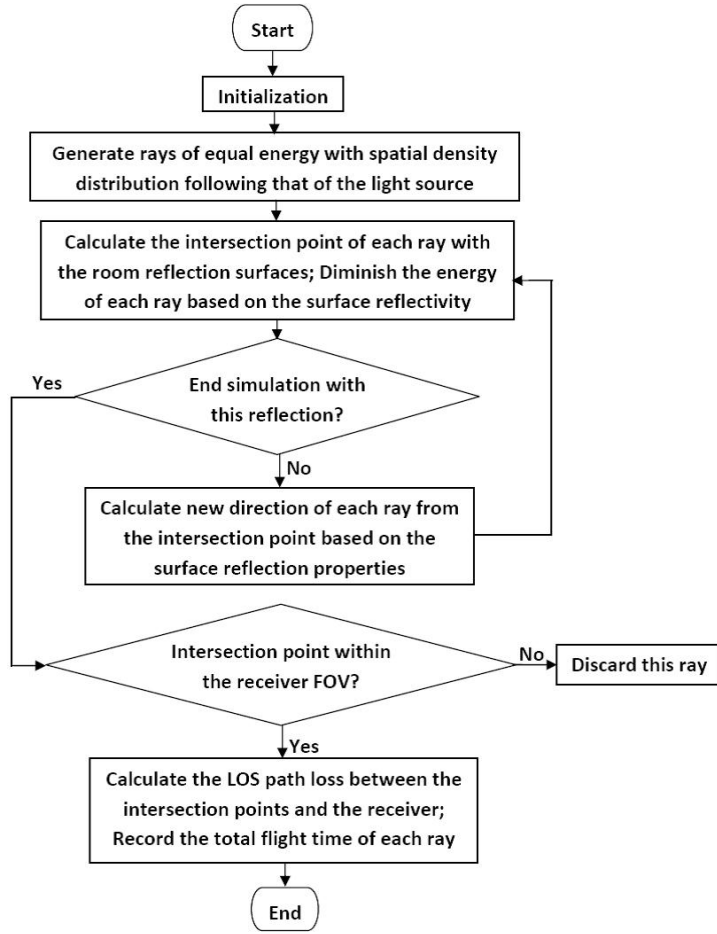
Figure 2.9: Block diagram of the process of the ray tracing simulation.
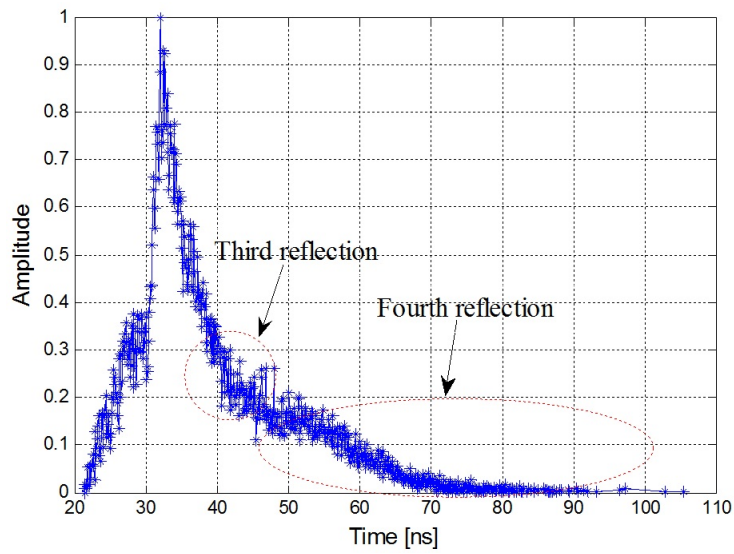
Figure 2.10: Ray tracing simulated NLOS channel impulse response with Rx1.
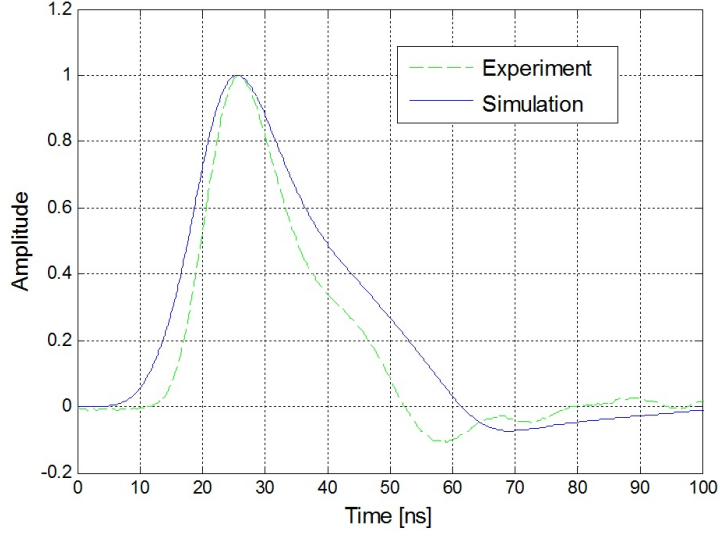
Figure 2.11: Simulated and experimental system impulse response results with Rx1.

For Rx2 with FOV of 132^0, the receiver ROV cone is very wide and can intersect with both the walls and the ceiling. Therefore the channel impulse response contains effects from direct diffusion (between the light spot on the ceiling and the receiver) to the first, second, and higher order reflections by surrounding surfaces. However, because the active receiving area is very small and the angle between the line from the light source to the receiver and the vertical line is large, the received optical power for the directly diffused (following the Lambertian pattern) path is much smaller than that from the NLOS reflected paths. The ray tracing simulated channel impulse response results are shown in Fig. 2.12. No obvious directly diffused component is observed. The first, second, third and fourth reflections are explicitly marked. Following the same method as before, we obtained the NLOS system impulse response by convolving this NLOS channel impulse response with measured LOS channel impulse response. The comparison with the experimental result is demonstrated in Fig. 2.13. Small deviations are observed between the simulation and experimental results, which may be caused by the idealization of the room interior surface properties and additional reflections
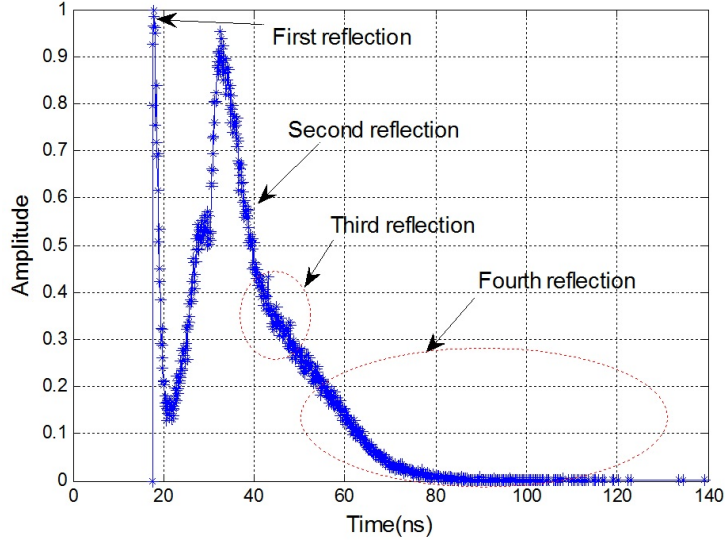
Figure 2.12: Simulated impulse response for Rx2.

introduced by the testbed platform within the receiver FOV.

Influence of transceiver parameters on the pulse shape

We have observed from the previous part that the receiver FOV jointly with the room configuration has a substantial influence on the NLOS channel impulse response. If the receiver FOV covers only a certain area on the ceiling excluding the beam spot, then an impulse response with only one dominant peak was mostly observed, as in Fig. 2.10. However, if the FOV can intersect both the ceiling and some walls, we may expect an impulse response with multiple peaks or a single peak but much larger FWHM. The positions of the transmitter and receiver also have significant impact. The impulse response varies significantly when the receiver moves toward the wall or toward the transmitter to include the beam spot on the ceiling within the receiver FOV. Thus the influence of the receiver FOV, transmitter and receiver locations, and the room configurations should be considered jointly based on geometric calculations.
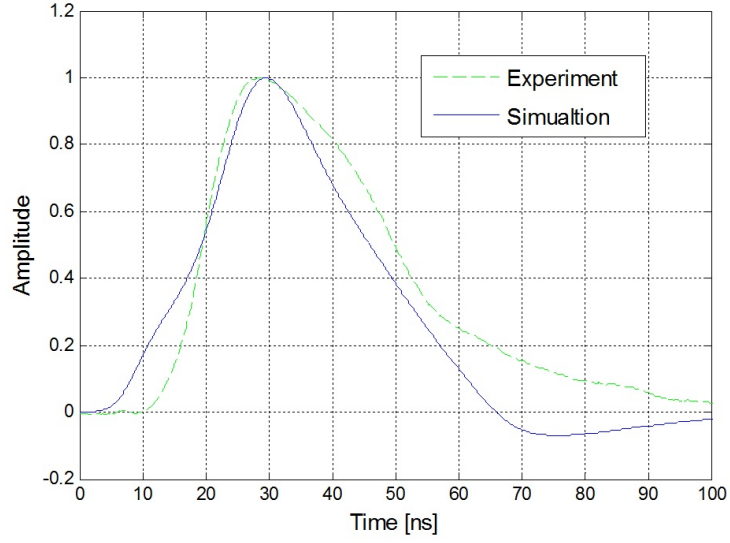
Figure 2.13: Comparison of simulation and experimental results for Rx2.

So far we have shown the impulse response results with the nearly collimated transmitter laser beam directly incident on the ceiling. We also carried out experiments to reveal the effects of varying the beam pattern and beam divergence angle. With the Thorlabs' engineered diffusers in front of the laser output port, we could reshape the beam into different beam patterns and divergence angles, including 50^0 circular, 50^0 square, and line patterns. The experimental results with Rx1 and Rx2 are shown in Fig. 2.14 and Fig. 2.15 respectively. It is observed that for a small FOV receiver, the beam pattern and angle have little effect on the impulse response. While for a large receiver FOV, the impulse response varies only slightly for the circle, square, and direct laser beam, but large variation occurs for the line pattern because the line on the ceiling extends to a large length and therefore the directly diffused component becomes significant.
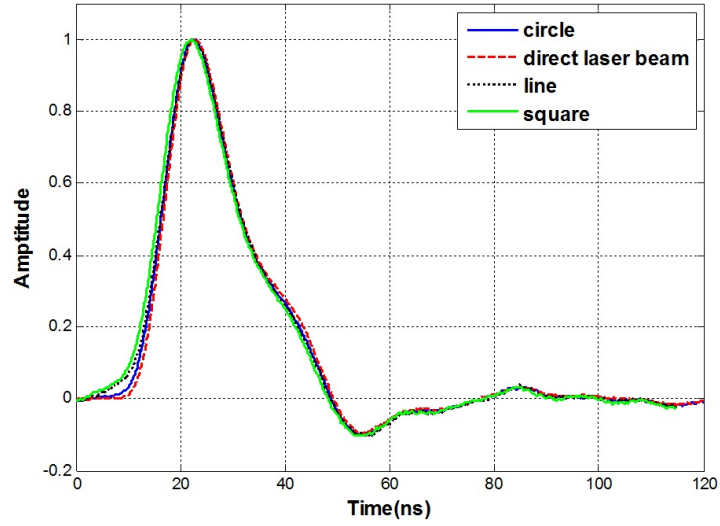
Figure 2.14: Effects of different incident laser beam patterns and angles for Rx1.
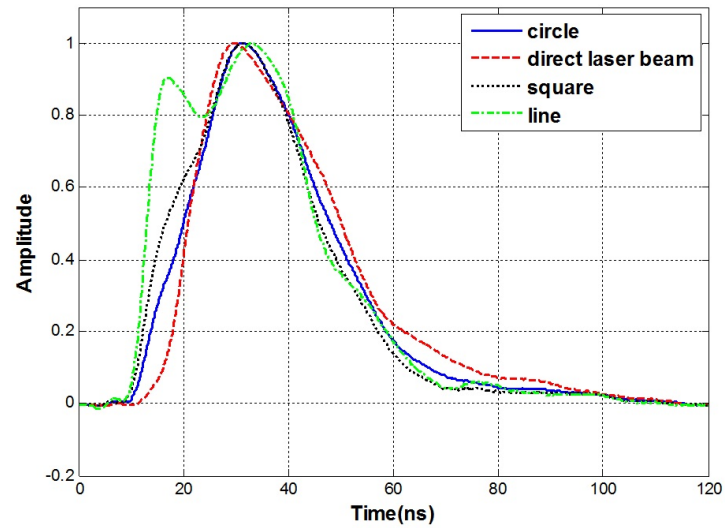
Figure 2.15: Effects of different incident laser beam patterns and angles for Rx2.
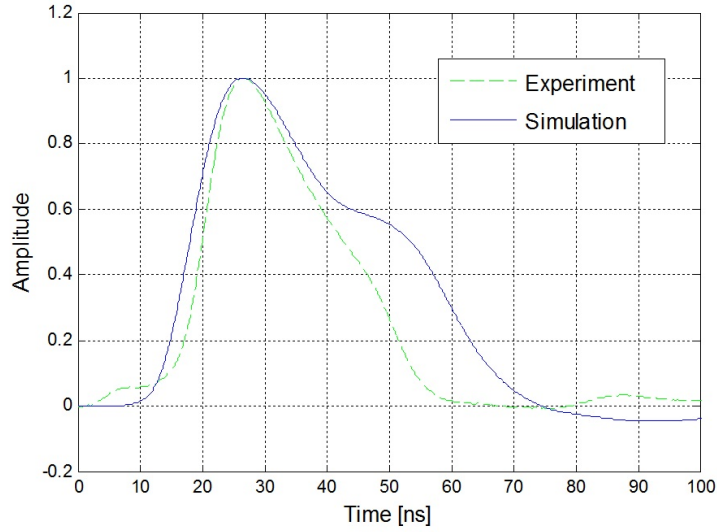
Figure 2.16: Comparison of the simulation and experimental results in a real office.

2.2.2.3 Experimental results in different scenarios

Next we provide more experimental results under different application scenarios other than an empty office. We measured the system impulse response in an office environment with desks, chairs, and computers inside. And using the typical room configuration parameters (length 10.3m, width 8.1m, and height 3.4m), we implemented the ray tracing computer simulation assuming an empty room for simplicity. The comparison with Rx2 is then shown in Fig. 2.16. Observed differences appear not substantial, indicating a reliable prediction using an empty room model.

The impulse response in a typical hallway with width of 3.5m and height of 3.1m was also measured. The horizontal distance between the transmitter and the receiver was 7m. In this case, there lack reflection walls on front and back sides, but only side walls and a floor. The impulse responses for Rx1 and Rx2 are quite similar (Fig. 2.17).

Next, we switched the measurement environment to a big lobby. We placed the

34
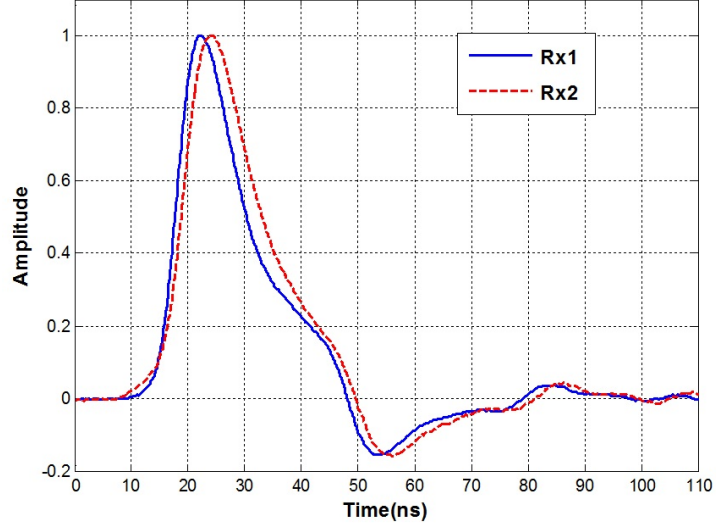
Figure 2.17: Measured impulse responses with Rx1 and Rx2 in a hallway.

transmitter and the receiver in the center of the lobby with horizontal distance of 5.85m and therefore the main reflections occur between the ceiling and the floor. Because the floor is covered with bright tiles that have large reflectivity, multiple reflections may occur and lead to the observed small peaks following the main peak in Fig. 2.18.

2.3 Noise Analysis

The noise that limits the communication system performance is mainly introduced by the channel and the receiver. Fig. 2.19 shows six major contributors to the noise present in the channel and receiver [53]. Here we will analyze each noise source that exists in an indoor VLC system to figure out their corresponding noise power spectral densities (PSD).

For an indoor VLC system using a white LED as the transmitter light source and a photodiode as the photodetector, the noise sources that should be considered
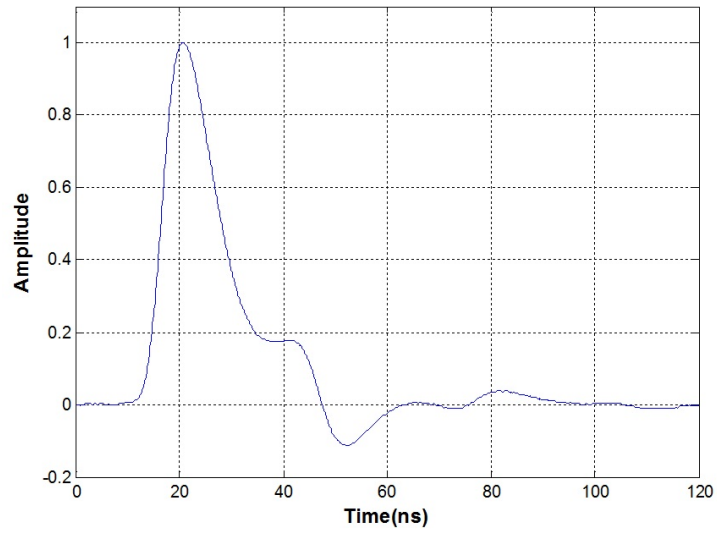
Figure 2.18: Measured impulse response in a lobby.
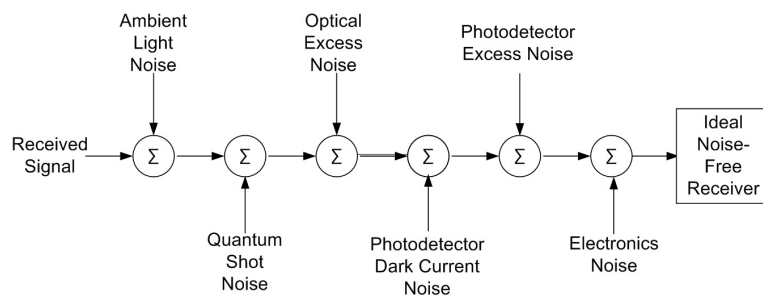
Figure 2.19: Various noise sources.

include ambient light noise, photodetector dark current noise, quantum shot noise, and electronics noise, which will be explained in detail later. Optical excess noise is defined as any noise that appears along with the received signal other than quantum shot noise and is usually prominent when a laser is used as the transmitter light source. Photodetector excess noise is induced by the gain multiplication process internal to the photodetector. This excess noise only exists in photodetectors with internal gain like an avalanche photodiode (APD) or a photomultiplier tube (PMT). Both of these two latter kinds of noise are excluded from our analysis for a VLC system with an LED and photodiode.

Since the input signal to the receiver circuit is a photodetected current, it is convenient to first characterize the noise at the input rather than at the output. Due to the fact that the electrical power of the current signal is proportional to the square of the current, we will express the signal and noise power with unit squared ampere A^2.

Ambient Light Noise

The ambient light contains radiation from various sources, such as the background sunlight through windows and emitted light from some common artificial light sources like incandescent and fluorescent lamps (Fig. 2.20) [54]. The background sunlight and incandescent lamps represent essentially unmodulated sources and result in mainly DC photodetector output current. This noise has negligible power at higher frequencies and therefore can be easily eliminated by a highpass filter. The unmodulated noise power spectral density (A^2/Hz) can then be represented as:

$$S_b(f) = \Big[\frac{e}{hc}\int_{\lambda_{rL}}^{\lambda_{rH}}\eta(\lambda)\lambda S_b(\lambda)R_f(\lambda)d\lambda\Big]^2\delta(f), \qquad (2.10)$$

where $\eta(\lambda)$ is the detector quantum efficiency, $S_b(\lambda)$ is the power spectrum density of the unmodulated background light, e is the electron charge, h is the Planck's constant,
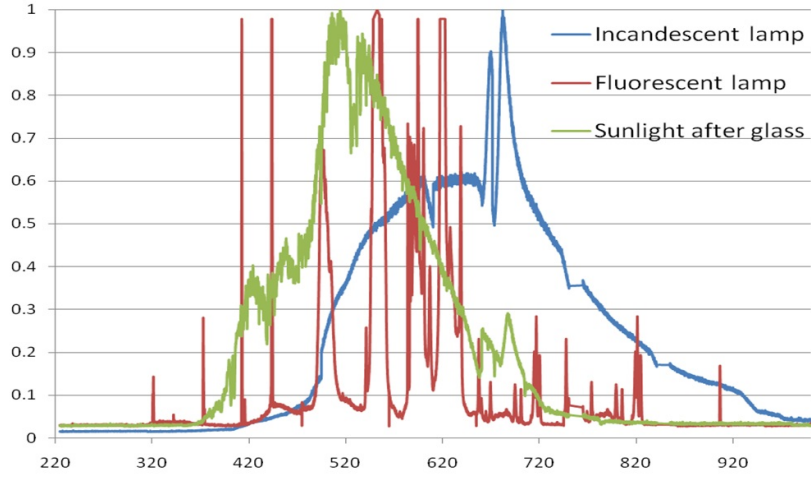
Figure 2.20: Normalized optical spectrum of ambient light sources.

and c is the speed of light. The combination $R_D(\lambda) = e\eta(\lambda)\lambda/hc$ in the above equation is the detector responsivity (A/W) at wavelength λ.

However, a fluorescent lamp can be modulated both at twice the utility frequency of either 50Hz or 60Hz using conventional ballasts and at much higher frequency of 20-40kHz using electronic ballasts. Thus its photodetector output current electrical spectrum may contain components at harmonics up to hundreds of kilohertz. Much research work has been done to measure its spectral distribution and study its effect on indoor optical wireless communication [55, 56, 57]. But it is difficult to propose a general model for this interference because of the variation of commercial fluorescent lamps and electronic ballasts with different switching frequencies, which might require measurement for precise characterization.

Dark Current Noise

Dark current in photodetectors corresponds to the random emission of electrons due to absorption of thermal energy at a fixed average rate when no field is being

38

detected. It is closely related to the device temperature and area. The dark current I_d is usually modeled as a DC current with noise PSD:

$$S_d(f) = I_d^2 \delta(f).$$ (2.11)

Quantum Shot Noise

The photodetection process in the photodetector is inherently a stochastic process, which means the output photocurrent is also stochastic with a certain probability distribution. Therefore we need to know the statistics of the photocurrent including the mean and variance. The mean photocurrent (including contributions from signal light, ambient light interference and dark current) contains the signal of interest that varies with the received optical power, whereas the variance acts as a distortion to the desired signal and represents the amount of noise power present in the photodetector's output. This shot noise arises from photodetection due to the quantum mechanical nature of light and is defined as quantum shot noise. The PSD of quantum shot noise induced by the unmodulated ambient light and dark current can be represented as:

$$S_{ds}(f) = 2e\Big[\frac{e}{hc}\int_{\lambda_{rL}}^{\lambda_{rH}} \eta(\lambda)\lambda S_b(\lambda)R_f(\lambda)d\lambda + I_d\Big],$$ (2.12)

where $S_b(\lambda)$ represents the ambient light noise power spectrum density.

Electronics Noise

Finally, we consider the electronics noise induced by the receiver circuit, the dominant part of which is introduced by the preamplifier front-end. Four principal types of front-end designs usually used in optical receivers include: resistor termination with a low-impedance voltage amplifier, high impedance amplifier, transimpedance amplifier, and noise matched or resonant amplifier [53]. Among them the transimpedance
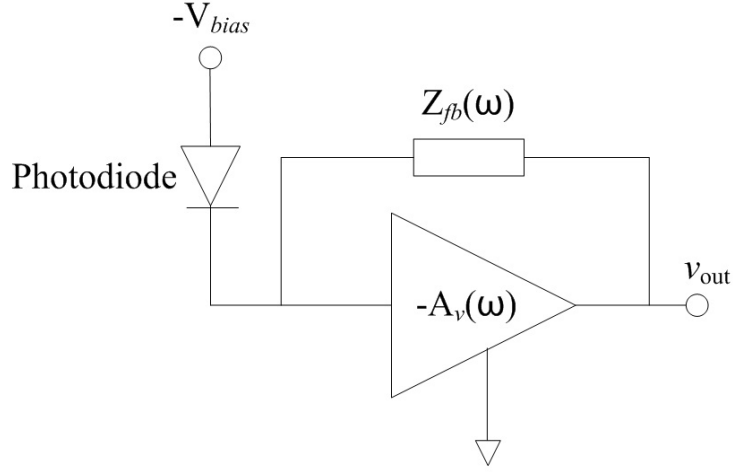
Figure 2.21: A typical transimpedance amplifier circuit configuration.

preamplifier is widely adopted in many optical wireless communication receiver front-end designs due to its capability to achieve relatively large bandwidth and comparatively low noise at the same time. A typical transimpedance amplifier circuit configuration is shown in Fig. 2.21 with feedback impedance $Z_{fb}(\omega)$ and open loop gain $A_v(\omega)$.

The equivalent input current noise PSD of this transimpedance amplifier is given as [53]:

$$S_a(f) = i_n^2 + \frac{4kT}{R_{fb}} + \frac{v_n^2}{R_t^2}[1 + (2\pi R_{fb}C_t f)^2], \tag{2.13}$$

where $R_t = R_{fb}A_0R_d/[(A_0+1)R_d + R_{fb}]$, $C_t = C_{fb} + C_d$, R_{fb} is the feedback resistance, A_0 is the core amplifier DC gain $A_v(0)$, C_{fb} is the feedback capacitance, R_d and C_d are the resistive and capacitive parts of the combined impedance (including the amplifier's input impedance, any load resistance, and the photodiode's internal impedance) respectively. Here the noise performance of the core amplifier is characterized by the spectral densities v_n^2 and i_n^2 of the internal voltage and current random noise sources. This whole electronics noise term can be treated as a zero-mean additive Gaussian random process with variance as the noise power.

If we adopt the field effect transistor (FET) to build the transimpedance amplifier, the input equivalent current noise PSD can be represented as:

$$S_{aFET}(f) = \left[\frac{4kT}{R_{fb}} + 2eI_L + \frac{4kT\Gamma}{g_m}(2\pi C_t)^2 f_c f + \frac{4kT\Gamma}{g_m}(2\pi C_t)^2 f^2 \right], \qquad (2.14)$$

where I_L is the gate leakage current, g_m is the FET transconductance, C_t is the total input capacitance, f_c is the $1/f$ noise corner frequency of the FET, Γ is the numerical constant (0.7 for Si JFETs, 1.03 for Si MOSFETs, and 1.75 for GaAs MESFETs). In the above equation, the first noise term is due to the feedback resistance thermal noise. The second and third noise terms are contributions from the leakage current and $1/f$ noise. The last term is due to the channel thermal noise and induced gate noise.

2.4   Uplink Options

In this section, some possible uplink options for a visible light communication system will be compared. Their performance will be compared in terms of capabilities of optical devices, light safety, background interference, and path loss.

Several approaches have already been investigated. Infrared (IR) has been considered to build an uplink with its transmitter co-located with the downlink VLC receiver [44] and a retro-reflecting transceiver also has been proposed [45]. Cooperation between VLC and radio frequency (RF) standards may also allow full connectivity for a terminal in which a VLC downlink can be combined with an RF uplink [46]. Besides the above proposed uplink options, the near ultraviolet (UV) and visible light (VL) spectra could be considered to provide uplink communication as well. The near UV spectra have a much relaxed eye safety requirement than those solar blind deep UV counterparts considered for non-line-of-sight (NLOS) communications [58]. However, obvious disadvantages exist in using RF and retro-reflecting transceivers that may prevent them

from real applications. For retro-reflecting transceivers, they cannot achieve a high modulation rate because the reflection is realized in a pure physical way which is hard to be modulated very fast. For a communication system that uses RF for uplink, large background interference from other indoor RF equipments is a major problem. Meanwhile, the cost of the whole mixed RF/optical communication system would correspondingly increase because two different sets of transceivers have to be integrated in the same communication unit (one in the RF domain and one in the optical domain). In some cases, RF is even prohibited such as hospital and aircraft cabin. Therefore our goal is to choose an uplink in the optical domain which can also achieve a relatively high data rate. Towards this end, the near UV, visible and infrared spectra become candidates. We will compare their performance to show the respective strength and weakness.

An uplink optical transmitter often makes use of an LED as the light source at relatively high transmitted power but low cost. The LEDs we choose to compare are all commercial off-the-shelf (COTS) commodities from ThorLabs with center wavelengths at 375nm (LED370E, near UV), 470nm (LED470E, blue) and 850nm (LED851L, IR) respectively. All of them have a modulation bandwidth of about 50MHz, which is large enough for our high data rate communication requirement. For an uplink receiver, we also choose commercial photodiodes combined with corresponding bandpass optical filters to reduce the background interference.

In the following part we will discuss the safety requirement for these optical bands. The safety issues of the baseband IR physical layer have been discussed [59]. Under the assumption that the system uses 4-PPM modulation and has a data rate of 2Mbit/s, the single pulse Maximum Permissible Exposure (MPE) for this system using LED as a light source is 28.2 mW/cm^2 based on the 1993 edition of the standard IEC-825-1-Safety of Laser Products [60]. For convenience of comparison, the same

assumption is adopted for the visible and near UV communication systems. Following the same procedure, the MPEs of the visible light and near UV can be calculated as follows.

There are three defined cases: single pulse irradiance, pulse train average irradiance, and repetitive pulse train irradiance. For repetitively pulsed radiation, the following method should be used to determine the MPE. For wavelengths between 400nm and 10^6nm, the MPE is determined by using the most restrictive requirements of a), b) and c) below. For wavelengths less than 400nm, the MPE is limited by the most restrictive requirements of a) and b). We will denote the MPEs for the visible light (470nm) and the near UV (375nm) as H_{vis} and H_{uv} respectively.

a) Single pulse irradiance. Suppose the maximum pulse duration is $t_d = 260ns$ and based on the IEC standard [60], when $1.0 \times 10^{-7} < t_d < 1.8 \times 10^{-5}s$, the MPE radiant exposure is given by: $H_{vis-sp} = 5 \times 10^{-3} J/m^2$, $H_{uv-sp} = C_1 J/m^2 = 5.6 \times 10^3 t_d^{0.25} J/m^2 = 5.6 \times 10^3 \times (260 \times 10^{-9})^{0.25} J/m^2 \approx 126.45 J/m^2$.

b) Pulse train average irradiance. For time window $T = 10s$, $H_{vis} = 18t^{0.75} J/m^2 \approx 101.22 J/m^2$, $H_{uv} = C_1 J/m^2 = 5.6 \times 10^3 t^{0.25} J/m^2 \approx 10^4 J/m^2$. Since there are $N = 107$ pulses in $T = 10s$, the average radiant exposure is $H_{vis-pt} = 101.22/10^7 J/m^2 \approx 10^{-5} J/m^2$, $H_{uv-pt} = 10^4/10^7 J/m^2 = 10^{-3} J/m^2$.

c) Repetitive pulse train irradiance. For $N = 10^7$ pulses, the repetitive pulse criterion specifies that $H_{vis-train} = H_{vis-sp} \times N^{-0.25} = 5 \times 10^{-3} \times 10^{-1.75} J/m2 \approx 8.89 \times 10^{-5} J/m^2$.

Therefore by taking the most restrictive requirement, the MPEs for the visible and near UV spectra are $H_{vis} = 10^{-5} J/m^2$ and $H_{uv} = 10^{-3} J/m^2$. The single pulse MPE could also be expressed in terms of irradiance as: $E_{vis} = H_{vis}/t_d = 3.9 mW/cm^2$ and $E_{uv} = H_{uv}/t_d = 384.6 mW/cm^2$.

Those are the MPEs evaluated for point sources. The MPE safety levels for extended sources at wavelengths from 400nm to 1400nm are those for point sources increased by the factor C_6. For visible spectrum and exposure time of 10s, C_6 is given by [60]: $C_6 = \alpha/\alpha_{min} = 50/11 = 4.5$, where α is the angular subtends of the LED source at the minimum accommodation distance (10cm) and α_{min} is the minimum angular subtends defined in the standard. Therefore $E_{vis-extended} = E_{vis} \times C_6 = 3.9 \times 4.5 = 17.6mW/cm^2$.

In summary, the MPEs for near UV, visible and infrared spectra are 384.6mW/cm^2, 17.6mW/cm^2 and 28.2mW/cm^2 respectively. We conclude that the near UV spectrum has the least restrictive requirement. If we assume the area of human body exposed to the transmitted light is 10cm^2, then the power exposure limit is 3.8W, 176mW and 282mW for the near UV, visible and infrared spectra respectively.

Background interference for the uplink in the visible light communication system is mainly composed of two parts, the scattered sunlight and the illumination light. We measured the power of three corresponding optical bands from the scattered sunlight in the order of several microwatts. But the electrical signal of the detector output due to incident scattered sunlight is concentrated around zero hertz. Such a DC current can be easily removed by an electrical filter, for example, we found a negligible output after we applied a 10KHz highpass filter. Therefore the scattered sunlight wouldn't introduce much interference for the uplink communication. For the illumination light, we examined some common light sources including white LED, mercury fluorescent lamp, and incandescent lamp. These sources have large amount of contribution to the visible spectrum while almost none in the near UV spectrum. Within the infrared band, things become different for these light sources. The white LED and mercury fluorescent lamp are measured to have very little component while the incandescent lamp has a relatively

large portion of light. The interference caused by illumination would be mainly determined by the future room lighting design including what types of light source to be used and where to be installed. Our measured spectra of various background interferences are shown in Fig. 2.20. These light sources are usually modulated at a certain electrical frequency, especially in the case of visible downlink communication using white LED, and thus can only be eliminated by an electrical filter when those frequency peaks are known and separated from the desirable signal.

Some experiments were carried out to measure the path loss for the three optical bands, the results of which are summarized in Tab. 2.3. The experimental setup is as follows. The transmitter was placed about 1.8m under the ceiling and pointed straight up. The receiver with an active receiving area of $0.81cm^2$ was located very close to the ceiling. Its field of view pointed straight down at the transmitter in the LOS case and oppositely in the NLOS case. For LOS path, the experimental results conform very well to the theoretical prediction. For NLOS path, the experimental results show that the ceiling has very strong absorption for the near UV and visible spectra while relatively weak absorption for the infrared band.

Table 2.3: Path loss results for LOS and NLOS uplink channels.

	Tx Optical Power (mW)	Half View Angle	LOS Received Power (μW)	LOS Path Loss (dB)	LOS Theorectical Path Loss (dB)	NLOS Received Power (μW)	NLOS Path Loss (dB)
Infrared (850nm)	3.2	6^0	2.0	32	31.4	0.45	38.5
Near UV (375nm)	1.2	5^0	1.1	30.4	29.4	0.015	49
Visible (470nm)	2.6	7.5^0	1	34.1	33.4	0.05	47.2

In conclusion, near UV has the least restrictive safety requirement and least background interference when compared with the other two options but it has large path loss for the NLOS link. It may be the best choice of uplink with LOS path. Infrared band has relatively restrictive safety requirement and large background interference from some light sources, but it may become a good choice of uplink for the NLOS communication link due to its least NLOS path loss. The visible band has the most restrictive safety requirement and probably the largest background interference. But the advantage in visibility is very helpful for pointing to the receiver. If the future LED lighting evolves into a main stream of 3-chip white LEDs, there are certain visible bands that interfere little with a downlink channel. In such a case, wavelength division duplexing is applicable.

2.5 Point-to-point System Demonstration and Link Performance

In this section, a preliminary indoor LOS visible light communication system prototype to demonstrate the feasibility of the indoor lighting combined VLC will be presented. The system can operate at a maximum horizontal separation of 3.5m and vertical distance of 1m with maximum data rate of 115kbps, mainly limited by the data rate of the RS232 interface. A systematic diagram is shown in Fig. 2.22 [61].

At the transmitter, we used nine 1-chip white LEDs (OSRAM LCW W5AM), each with 69lm output under 350mA driving current and full beam angle of 170^0. The relative radiant power spectrum density and the spatial intensity distribution curves of each LED can be found in their datasheets. These LEDs were driven by OOK signals
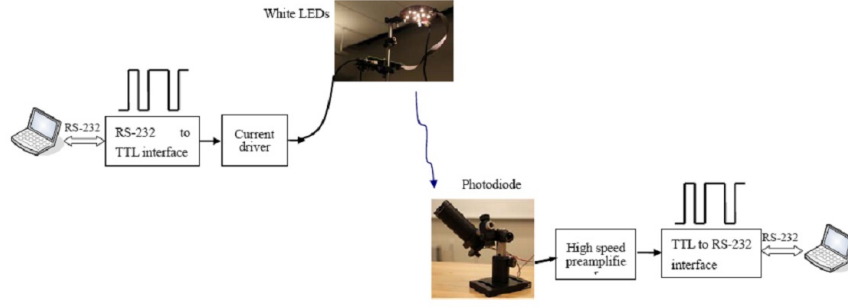
Figure 2.22: Systematic block diagram of the demonstration system.

from the laptop connected by an RS232 cable and a corresponding interface. Since the system can only operate at a data rate far less than the modulation bandwidth of the white LED, pre-equalization is unnecessary.

At the receiver, a commercial photodiode (PDA10A) with an internal transimpedance preamplifier was used. It has an active area of 0.8mm^2 and an electrical signal bandwidth of 150MHz. A concentrator is used in front of the photodiode, along with an optical bandpass filter (Thorlabs FB450-40), The filter has a center wavelength of 450nm, a full width at half maximum (FWHM) of 40nm, and transmittance of about 70%. These components were jointly used to expand the active receiving area and reduce the ambient light noise. The output electrical signal from the photodiode was also input into a laptop through a RS232 cable and corresponding interface.

The LEDs were first driven each with a constant current of 350mA. At each position the receiver was pointed toward the transmitter. We calculated the received optical power distribution on the receiver plane (Fig. 2.23) based on the channel model in Section 2.2.1 and datasheets provided by the vendor. We also calculated the achieved illuminance at the receiver plane, which shows a similar distribution as the received optical power, with maximum illuminance of 120lx at the center and 60lx at 1m horizontal separation. The achieved illuminance using this LED illumination is below the stan-
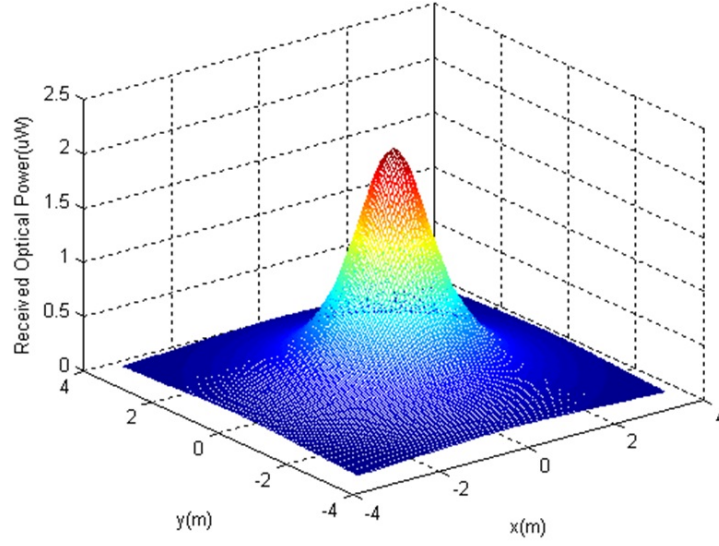
Figure 2.23: Received optical power distribution.

dardized average level of 300-500lx for an office environment. Utilizing more LEDs, for example 40 LEDs, is promising to provide the required illumination level within about 1m^2 area.

Next we analyzed the major noise sources present in this system. The measured ambient light noise power in the 450nm band is about 2μW, mainly induced by the scattered sunlight inside the office (with many large glass windows) and diffused light from fluorescent lamps modulated with powerline frequency 60Hz. We then input this ambient light generated photocurrent into the oscilloscope and found no obvious high frequency component, which mainly represents a kind of close-to-DC interference and also indicates the emitted light from the fluorescent lamps has insignificant power in the 450nm band. For our adopted OOK modulation scheme here, its effect can be easily eliminated by adjusting the optimal detection threshold which is implemented at the TTL to RS232 interface. A run length limiting (RLL) code (or line code) may be considered as an advanced option to minimizing data-induced DC components. An easy-
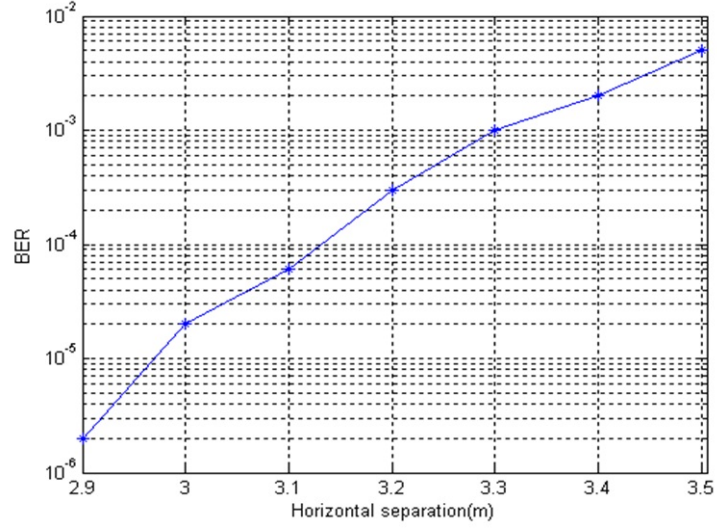
Figure 2.24: Measured BER performance.

to-implement line code is Manchester code. At the receiver, all RLL decoders can be AC coupled to reject the "near DC" ambient noise. The ambient light induced shot noise can be calculated based on our discussions in Section 2.3, which approximately equals $10^{-20}A^2$. The preamplifier noise can be characterized using the datasheets provided by the vendor, which indicates a value of roughly $1.5 \times 10^{-17}A^2$. The approximate SNR distribution can then be obtained according to Fig. 2.23 and the above calculated noise value.

Finally we measured the BER performance of this system by substituting the computer with a BER tester. The vertical distance was fixed and the BERs at varying horizontal separations were measured. At each position the pointing angle of the receiver was adjusted to gain the largest signal value and the detection threshold was adjusted manually to approach the optimum detection threshold. The measurement results for the horizontal separation from 2.9m to 3.5m are shown in Fig. 2.24. No notable BERs could be recorded by the tester for the horizontal separation within 2.9m.

49

Chapter 3

Data Rate Improving Techniques

Basic physical layer characteristics of an indoor VLC link have been discussed in the previous section. In allusion to those characteristics, more advanced communication system design techniques common in the traditional RF systems can be adopted to boost the system capacity and improve the system performance, which are the emphasis of this chapter. Several data rate improving techniques will be introduced, including the transmitter pre-equalization, the OFDM modulation, and the optical MIMO. Some key issues in applying these techniques to a VLC system will be investigated.

3.1 Transmitter Pre-equalization

At present, there are two major types of white LEDs, one type featuring a blue LED chip with a layer of yellow phosphor and the other embracing three LED chips in red, green and blue colors. Their typical spectral densities are shown in Fig. 3.1 [62].

A major challenge in achieving high-speed data transmission using these sources is their limited modulation bandwidth. For 1-chip white LED, this is partially attributed to the slow response of the yellow phosphor. Thus, one may utilize only the blue com-
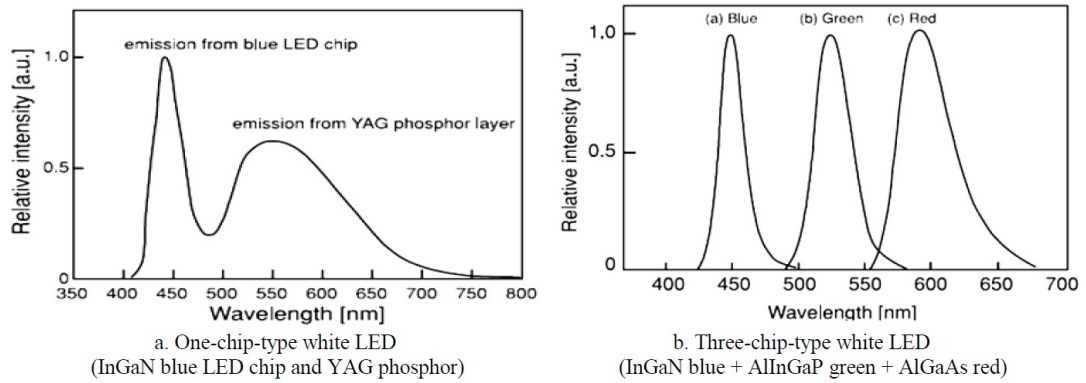
Figure 3.1: Spectral densities of 1-chip and 3-chip white LEDs.

ponent for a high bandwidth at the price of reduced received optical power. Techniques to improve the modulation bandwidth using blue filtering at the receiver have been reported [13]. The modulation bandwidth of these two types of LEDs with blue filtering is typically ∼15MHz for 1-chip LED and ∼25MHz for the 3-chip LED. Pre-equalization techniques for both multiple LEDs and single LED to further enhance the modulation bandwidth have been proposed using analog driver circuits [19, 20, 21]. Here we will present a new pre-equalization technique using a digital filter to improve the frequency response of the transmitter unit (filter plus LED) and hence increase the modulation bandwidth.

Our main idea is to treat the commercial white LED as a low pass filter and then a complementary filter can be designed correspondingly to make the joint frequency response of the LED with complementary filter flat within a certain frequency range [54]. The complementary filter can be realized digitally using FPGA or DSP which is easy to implement and can also be easily changed to adapt to different LEDs. This results in a great advantage in flexibility as compared to an analog circuit that is hard to alter for different LEDs.

In order to realize the above idea, it's first needed to determine the frequency
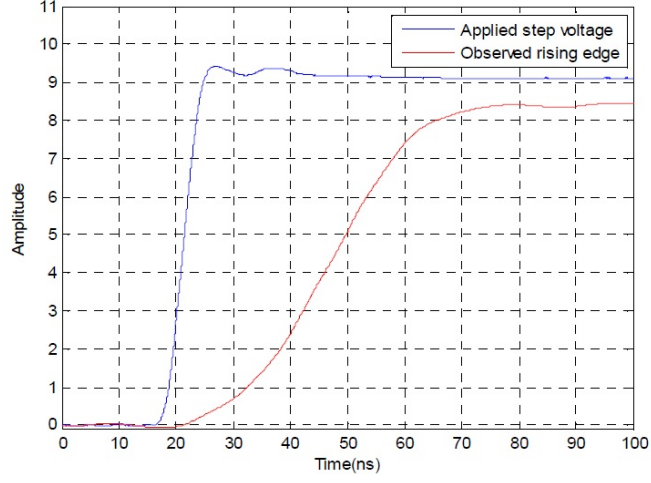
Figure 3.2: Input step voltage and observed optical intensity rising edge.

response of an LED. Here we propose an easy method to obtain the impulse response of the LED and hence the frequency response using Fourier Transform. The LED is assumed to be a linear time invariant (LTI) system. A narrow rectangular voltage pulse is applied as an input to the LED and the response (rising edge of the transmitted optical intensity) is recorded using a photodiode and an oscilloscope, as shown in Fig. 3.2.

From the figure we can tell that the applied step voltage has a rising edge of duration $\sim$7ns, while the duration of the observed optical intensity rising edge is $\sim$70ns, which is much larger than the input rising duration. If we treat the input step voltage as an ideal step function $u(t)$, then the output $y(t) = h(t) \otimes u(t)$ where $h(t)$ denotes the impulse response of the LED, and $\otimes$ represents the convolution. By simple calculations we can obtain that $h(t) = dy(t)/dt$, which is just the derivative of the output. The Fourier Transform of the impulse response $h(t)$ gives the frequency response of the LED. Two kinds of commercial off-the-shelf white LEDs have been chosen for validation, the 1-chip white LED (OSRAM LW W5SN-JYKZ-5K8L-Z) and

the 3-chip white LED (ThorLabs LEDRGBE). The results are shown in Fig. 3.3 and Fig. 3.4. In the above analysis, the response time of the photodiode was neglected. This is because the adopted photodiode (ThorLabs PDA10A) has a very large bandwidth of $\sim$150MHz. Its response time of $\sim$6.67ns is much smaller than the LED transmitted optical intensity rising duration.

With the obtained frequency responses of the LEDs, corresponding complementary digital filters can be designed to improve the joint frequency responses. Matlab is used to design two kinds of digital filters, the FIR filter and the IIR filter. Two parameters need to be determined. The first is the range of frequency band chosen to be flattened (targeted bandwidth) and the second is the order of the digital filter. The first parameter is closely related to the transmitted power and bandwidth requirement of the post digital-to-analog converter (DAC). The joint frequency response can be written as $Y(f) = H(f)W(f)$ where $H(f)$ is the LED frequency response and $W(f)$ is the normalized digital filter frequency response which is designed to be the product of the inverse of the $H(f)$ and a normalizing coefficient $H(f)_{min}$. Thus $Y(f)$ actually approximates $H(f)_{min}$, which is the minimum value of the frequency response of the white LED over the desirable frequency range. In order to maintain a certain level of transmitted optical power, the driving signal power has to be raised correspondingly. There exists a tradeoff between the transmitted power and the improved modulation bandwidth. The second parameter is mainly limited by the capabilities of the digital processors (DSP or FPGA) such as the computation power. For instance, the higher the order is, the larger clock frequency is needed. Clearly a complexity/performance tradeoff exists. Usually it requires the order of $\sim$150 for the FIR filter to achieve excellent performance while for the IIR filter it only requires the order of $\sim$50 and even less. In Fig. 3.5 the equalized frequency responses using FIR and IIR filtering techniques in comparison with the
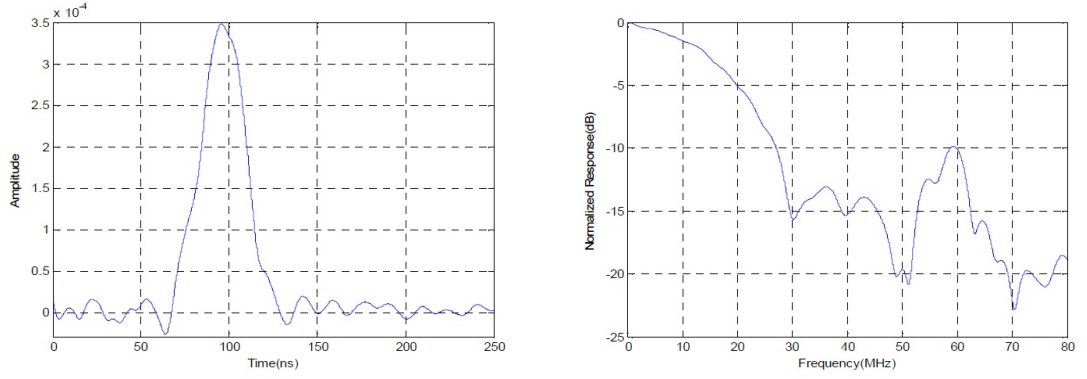
Figure 3.3: Impulse and frequency responses of the 1-chip white LED.
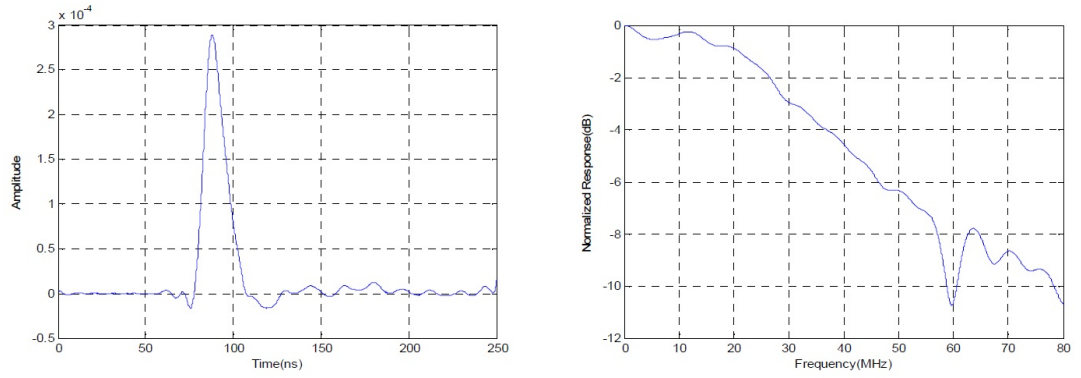
Figure 3.4: Impulse and frequency responses of the 3-chip white LED.

original LED frequency response are presented.

3.2 An Advanced Modulation Scheme: Orthogonal Frequency Division Multiplexing (OFDM)

The motivation of applying OFDM in an indoor VLC system can be attributed to two aspects. The first aspect is its capability to combat the intersymbol interference (ISI). As can be observed from Section 2.2.2, the channel impulse response could extend tens of nanoseconds when an NLOS diffuse channel is considered. Combined with the

a. 1-Chip LED frequency response   b. 3-Chip LED frequency response
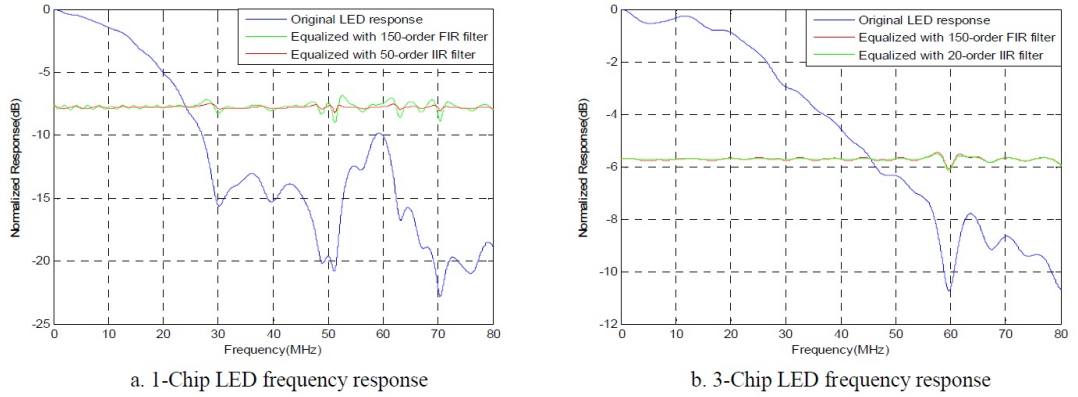
Figure 3.5: Frequency responses of white LED before and after pre-equalization.

impulse response of the lighting LED as shown in Section 3.1, the overall system impulse response could extend up to hundreds of nanoseconds. Besides the pre-equalization techniques we mentioned in Section 3.1 and the post-equalization techniques [17, 22, 23], another solution is to adopt the OFDM modulation. By adding a cyclic prefix with length no shorter than the system impulse response, the ISI effect at the receiver can be eliminated. The other motivation is that the indoor VLC system in general is a bandwidth-limited system instead of a power-limited system. Its bandwidth constraint mainly results from the limited modulation bandwidth of the LED and the NLOS channel. Meanwhile, because the VLC system is piggybacked on the indoor lighting system, the required illumination level sets a lower limit for the transmitted optical power, thus resulting in high SNR at the receiver end. OFDM is inherently a bandwidth efficient modulation scheme and therefore should be considered.

3.2.1 General OFDM structure

The basedband model of an optical OFDM transmission system is depicted in Fig. 3.6 [27]. An input binary bit stream $b[i]$ is grouped by passing through a serial-to-parallel (S/P) converter to generate parallel streams before being modulated. The
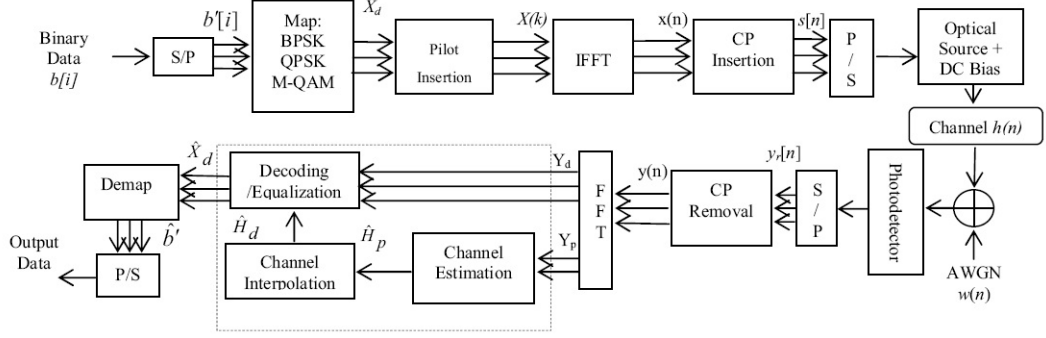
Figure 3.6: Baseband model of an optical OFDM system.

modulation schemes adopted could be BPSK, QPSK, and M-QAM. The modulated output symbols are defined as $X = X_0, X_1, ..., X_{2N-1}$. Pilot signals are uniformly inserted into all subcarriers for channel estimation in diffuse links. For LOS links there is no need for the pilot signals. The Inverse Fast Fourier Transform (IFFT) block is used to implement the OFDM, transforming the data sequence $X(k)$ of length $2N$ into a time-domain signal. The transmitted information symbols $X(k)$ are the frequency coefficients and the output of the IFFT block $x(n)$ is the time domain of the input samples: $x(n) = IFFT_{2N}\{X(k)\}$, where n and $k = 0, 1, 2, ..., 2N - 1$. In optical system with intensity modulation, only real-value and positive signals are used. Therefore in order for the OFDM to be applied in the VLC system, the input information symbols $X(k)$ should have Hermitian symmetry to produce real value at the IFFT block output. To mitigate the effects of multipath induced ISI, OFDM symbol is preceded by a cyclic prefix (CP) as shown in Fig. 3.7. The length of the CP is normally considered to be greater than or equal to the channel length (impulse response time) to eliminate the ISI.

In optical transmission with Intensity Modulation/Direct Detection (IM/DD), the positivity of the OFDM signal can be guaranteed by either adding a DC bias, as in
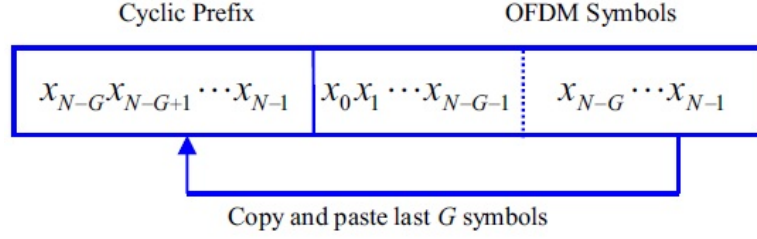
Figure 3.7: OFDM symbol structure with a cyclic prefix.

DC biased optical OFDM (DCO-OFDM) [63], or by clipping at zero and transmitting only the positive parts of the OFDM waveform as in asymmetrically clipped optical OFDM (ACO-OFDM) [64]. Finally, the OFDM signal is passed through a parallel-to-serial converter (P/S) to generate a discrete-time OFDM symbol $s(n)$ of duration $T_s = 2NT + GT$, where $\triangle f = B/2N$ is the frequency spacing between the subcarriers within the system bandwidth B. Then the continuous-time symbol applied to the optical source is produced by passing the discrete-time OFDM symbol to a digital-to-analog converter (DAC).

The received OFDM signal propagated through the channel $h(n)$ is given by:

$$y[n] = Rs[n] \otimes h[n] + n[n], \tag{3.1}$$

where $n[n]$ is the additive noise, R is the responsivity of the photodetector and $\otimes$ denotes the convolution. The channel impulse response $h[n]$ and the noise term $n[n]$ can be determined as introduced in Section 2.2 and 2.3. Due to the CP, the discrete linear convolution of $s[n]$ and $h[n]$ becomes a circular convolution hence simplifying the equalization process at the receiver. Thus at the receiver, the signal is passed through S/P and its CP from each received symbol is removed before being applied to the N-point FFT block: $Y(k) = FFT_{2N}\{y(n)\}$.

3.2.2 Probability distribution of the Peak to Average Power Ratio (PAPR) and Crest Factor (CF)

One of the major disadvantages of an OFDM based system is the high Peak to Average Power Ratio (PAPR) and Crest Factor (CF) of the time domain signal. In traditional RF based systems, this usually necessitates a transmitter with a high dynamic range and hence results in reduced power efficiency. In the proposed indoor VLC system, the high PAPR of the transmitted OFDM symbol could result in the flickering issue of the LED lighting. Besides, due to the limited linear input-output operating range, high PAPR could lead to the transmitter LED working in the nonlinear region, introducing distortion to the transmitted OFDM symbol. Next we will derive the probability distribution of the PAPR and CF [65], providing guidance for the OFDM system design.

In the OWC OFDM system, without loss of generality, the equivalent digital complex baseband signal of the OFDM symbol after the IFFT block can be written as

$$x(n) = \frac{1}{\sqrt{2N}} \sum_{k=0}^{2N-1} \left(X_k e^{j2\pi k \frac{n}{2N}} \right), \tag{3.2}$$

where $2N$ is the number of subcarriers. By imposing the conjugate symmetry constraint $X_k = X_{2N-k}^*, k = 1, 2, ..., N-1$, where the DC bias of the OFDM is assumed to be zero, $X_0 = X_N = 0$, the signal becomes real, expressed as

$$x(n) = \frac{2}{\sqrt{2N}} \sum_{k=0}^{N-1} |X_k| \cos \left(2\pi k \frac{n}{2N} + arg(X_k) \right). \tag{3.3}$$

When N is large enough, according to the central limit theorem, $x(n)$ is an asymptotically Gaussian variable with zero mean and variance $E\left[|x(n)|^2\right] = E\left[|X(k)|^2\right] = \sigma^2$. The normalized envelope of the OFDM signal is $Env(n) = |x(n)|/\sqrt{P_{ave}}$ and the normalized signal power is $P(n) = x(n)^2/P_{ave}$, where $P_{ave} = \sigma^2$ is the average power of the

OFDM signal. Their probability density functions (PDFs) can be derived as

$$f_{Env}(y) = \begin{cases} \sqrt{\frac{2}{\pi}} e^{-y^2/2}, & y > 0 \\ \\ 0, & y \leq 0 \end{cases} \tag{3.4}$$

$$f_P(p) = \begin{cases} \sqrt{\frac{2}{\pi}} p^{-1/2} e^{-p/2}, & p > 0 \\ \\ 0, & p \leq 0 \end{cases}. \tag{3.5}$$

Different from the case in traditional RF OFDM systems, where the envelope of the OFDM signal is asymptotically a Rayleigh process and the signal power obeys χ^2 distribution [66], it can be observed the envelope and the signal power of the optical wireless OFDM signal follow different probability distributions.

The PAPR of the OFDM symbol is defined as

$$PAPR = \frac{\max_{0 \leq n \leq 2N-1} |x(n)|^2}{P_{ave}}, \tag{3.6}$$

and the CF is defined as: $CF = \sqrt{PAPR}$. Assume the samples in one OFDM symbol are uncorrelated with each other, the cumulative distribution functions (CDFs) of the PAPR and CF can be derived as,

$$F_{PAPR}(z) = F_p(z)^{2N}, \tag{3.7}$$

$$F_{CF}(z) = F_{Env}(z)^{2N}, \tag{3.8}$$

where $F_p(z)$ and $F_{Env}(z)$ are the CDFs of the envelope and power of the OFDM signal respectively.

Figure 3.8 compares CDFs of CF and PAPR between optical wireless (OW) OFDM and RF OFDM. It's observed that for a given threshold value and number of subcarriers, the CDF of the PAPR for the OW OFDM symbol is much lower than that for the RF OFDM symbol. This means the OW OFDM system has a more severe

59
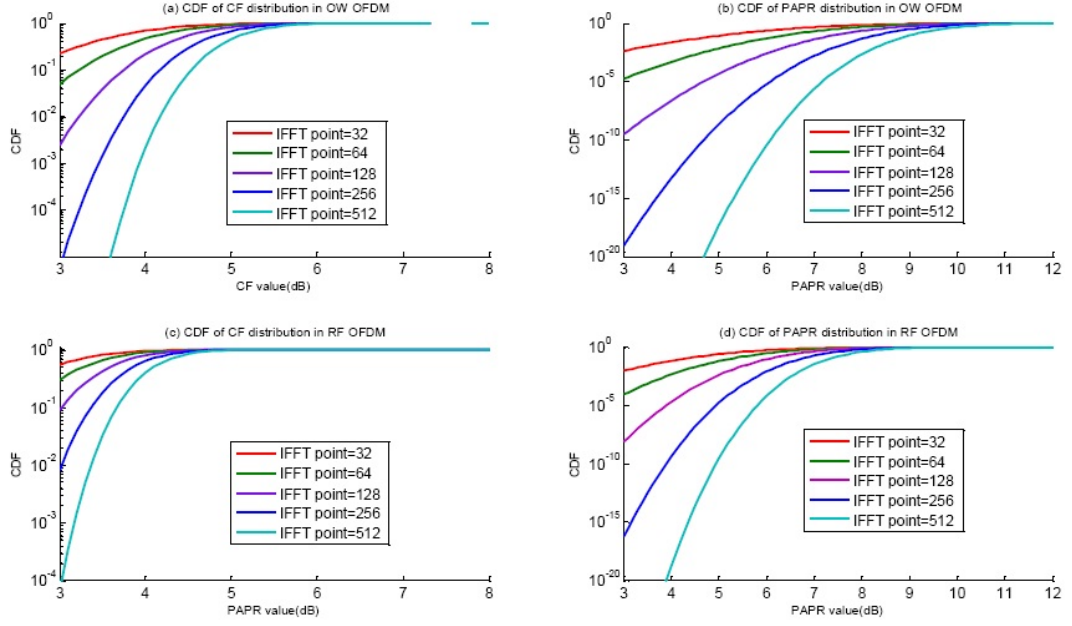
Figure 3.8: Cumulative distribution functions of PAPR and CF.

PAPR issue than the RF OFDM system. Also as the number of subcarriers increases, the PAPR problem also deteriorates. Similar conclusion can be drawn for the CF.

From the above analysis it can be observed that the PAPR is not related closely with the modulation constellation size of each subchannel. It is determined merely by the number of subchannels (equivalent to the number of IFFT points). The PAPR issue is more prominent with larger number of subchannels. The simulation results therefore can provide guidance in choosing the appropriate number of subchannels in an OFDM VLC system design.

3.3 Optical Multiple-input-multiple-output (MIMO) Communications

In the previous sections we have discussed several system design techniques for achieving high data rate of the indoor VLC system. Besides, another effective solution is to take advantage of the spatial resolution of different transmitting LEDs, which could be utilized to realize multiple-input-multiple-output (MIMO) communication.

While MIMO is widely used in radio communications [67], corresponding research for indoor optical wireless has only been recently carried out. In [68], a multispot-diffuse MIMO system was proposed and a low-rate pixilated MIMO system was introduced in [69]. The space-time coding for indoor diffuse optical wireless MIMO systems was discussed in [70]. Both the non-imaging and imaging optical MIMO VLC systems were proposed in [34]. BER results for a non-imaging optical MIMO system and the requirement of pixel size at different data rates for an imaging optical MIMO system were numerically studied. In this section, channel capacity is studied for both non-imaging and imaging MIMO VLC systems. The system model will be introduced, followed by the investigation of the channel capacities both analytically and numerically in typical scenarios respectively.

3.3.1 System description

The non-imaging and imaging MIMO VLC systems follow the same structure as in [34] (Fig. 3.9 and Fig. 3.10). Multiple LED arrays are mounted on the ceiling. Each of them serves as an independent transmitter and can be used to transmit parallel data streams. The difference between two VLC systems lies in the receiver front-end. Multiple separate photodetectors are adopted at the receiver for the non-imaging MIMO system,
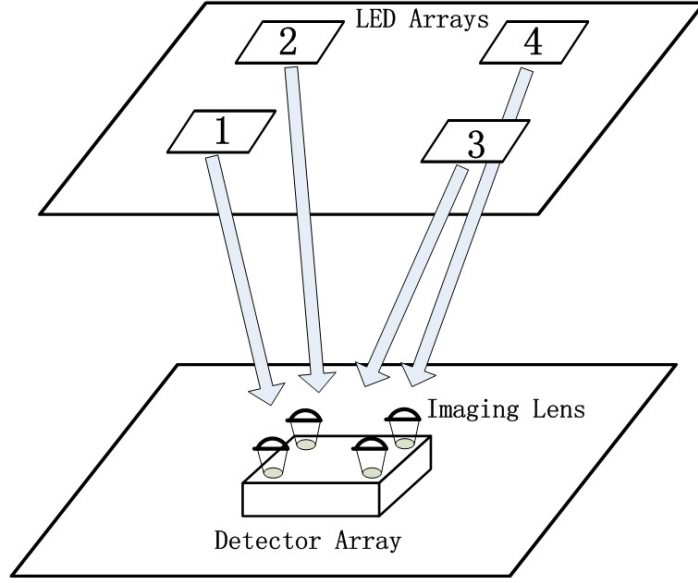
Figure 3.9: Non-imaging MIMO VLC system.

each having a front lens to collect more optical signal power. Their outputs could be processed jointly to recover the transmitted information. For the imaging MIMO VLC system, usually an imaging lens is mounted in front of an image array which contains multiple closely aligned pixel elements. Transmitting LED arrays are imaged onto the sensor plane, and each receiving element receives different portions of the energy.

Two typical propagation links exist, namely the line-of-sight (LOS) link and non-line-of-sight (NLOS) diffuse link. According to [22], the strongest diffuse component is at least 7dB (electrical) lower than the weakest LOS component. Therefore only the LOS link is considered for performance evaluation. The channel matrix can be fully described by the DC gains from the transmitter to the receiver.
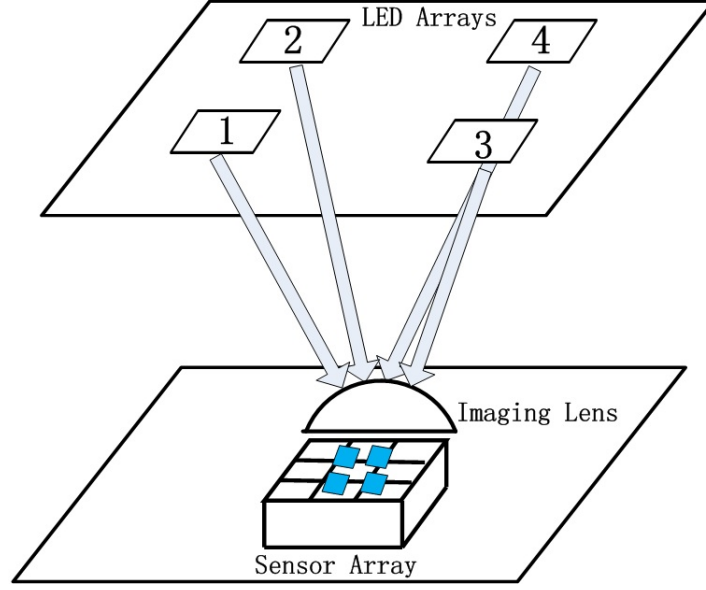
Figure 3.10: Imaging MIMO VLC system.

3.3.1.1 Non-imaging MIMO VLC system

If we treat each LED array as a single light source and model its beam transmission pattern as Lambertian, according to the discussion in Section 2.2.1 the DC gain between receiver antenna i and transmitter antenna j, h_{ij}, can be expressed as [61]

$$h_{ij} = \begin{cases} \frac{(m_j+1)A_i}{2\pi D_{ij}^2} \cos \alpha_{ij} \cos_j^m(\beta_{ij}), & 0 \leq \alpha_{ij} \leq \Psi_i \\ 0, & \alpha_{ij} > \Psi_i \end{cases}, \qquad (3.9)$$

where m_j is the order of the Lamertian radiation pattern for transmitter j, A_i is the active receiving area of receiver i, D_{ij} is the distance between transmitter j and receiver i, α_{ij} and β_{ij} are the incident angle and emitting angle from transmitter j to receiver i respectively, and Ψ_i is the field of view (FOV) of receiver i. The $N_r \times N_t$ channel matrix $\mathbf{H} = [h_{ij}]$ has $(i,j)th$ entry h_{ij}, where N_t and N_r are the numbers of transmitting and receiving elements respectively.

63

3.3.1.2 Imaging MIMO VLC system

For such a system, the DC gain from transmitter j to the receiver front-end imaging lens h_j can be similarly determined. Images are projected onto the sensor array, which fall on one or several elements. The DC gain from transmitting antenna j to each receiving sensor antenna i can be represented as

$$h'_{ij} = a_{ij}h_j, \quad a_{ij} = \frac{A_{ij}}{\sum_{p=1}^{N_r} A_{pj}}, \tag{3.10}$$

where A_{ij} and a_{ij} are the area of the image and the proportion of the energy of transmitting light source j that falls on receiving pixel i respectively. The scalar a_{ij} is fully dependent on the transmitting LED lamp shape and the imaging system. Denote $i_T(x,y)$ as the emitted spatial optical intensity distribution on the transmitter plane and $i_R(x,y)$ as the received spatial distribution of optical intensity over the image plane. Let M denote the magnification predicted by geometrical optics of the imaging system and define $i'_T(x,y)$ as the image of the transmitting plane on the image plane due solely to geometric optics. Their relations are expressed as [69]

$$i'_T(x,y) = \frac{1}{M}i_T(\frac{x}{M}, \frac{y}{M}), \tag{3.11}$$

$$i_R(x,y) = h_{imag}(x,y) \otimes i'_T(x,y), \tag{3.12}$$

where $h_{imag}(x,y)$ is the point-spread function characterizing the response of the imaging system to a spatial impulse of optical intensity and is usually characterized by a linear spatial filter. Fundamentally, $h_{imag}(x,y)$ is limited by diffraction due to the finite aperture size of practical components.

3.3.1.3 Noise

For an indoor VLC system, typical noise sources include thermal noise from electronics and detector shot noise. Shot noise is dominant at a high illumination level,

while thermal noise is dominant at lower background illumination. The shot noise is essentially a Poisson random process, while it approaches a Gaussian process according to the central limit theorem when the received background illumination is high. Its single-sided power spectral density (PSD) is expressed as

$$\sigma_{shot}^2 = 2q\gamma P, \tag{3.13}$$

where q is the electron charge, γ is the responsivity of the photodetector (A/W), and P is the total received optical power at the photodetector. Besides, the thermal noise is also usually modeled as Gaussian distributed. The sum noise term therefore can be approximated as an additive white Gaussian noise.

3.3.2 Channel capacity

For intensity-modulation/direct-detection (IM/DD) optical wireless communication systems, there exist two unique characteristics different from traditional RF communications: non-negativity and optical power constraint of the transmitted signal (equivalent to the amplitude constraint in traditional RF communication systems). Here the capacity of the VLC channel with an average optical power (input signal amplitude) constraint is studied following [69]. A DC bias corresponding to the average optical power P is applied to each LED lamp. Let the total electrical power constraint for each LED lamp, E, be a function of the average optical power constraint, as $E = cP^2$ for some constant $c > 0$ with unit A^2/W^2. The constant c is chosen so that the clipping distortion of the channel is minimized. For a given bias optical power P, c is set to ensure that the probability of negative amplitude is small. Any negative excursions by the signal are clipped and modeled as noise. Assume each transmitted symbol is independent and Gaussian-distributed with mean P and variance $\varepsilon^2 cP^2/N_t$, the clipping

probability can be approximated as

$$P_{clip} = 2Q\left(\frac{P}{\sqrt{\varepsilon^2 cP^2/N_t}}\right),\tag{3.14}$$

where ε is the LED efficiency with unit W/A. If P_{clip} is set to be an acceptable value of 10^{-8}, the value of $\varepsilon^2 c$ should be taken as $\varepsilon^2 c = 0.0304 \times N_t$. Considering the equivalent electrical power constraint, the channel matrix is revised accordingly as $\mathbf{H}' = \varepsilon \mathbf{H}\gamma$, where γ is the photodetector responsivity with unit A/W. Also as we mentioned in the previous section, the shot noise at each receiver antenna is dependent on the input intensity level. In order to estimate the capacity, we make the pessimistic assumption that the noise variance at each receiver antenna, σ^2, is the maximum over all inputs and they are independent.

Following the analysis for traditional RF MIMO systems, perform singular value decomposition on the channel [71],

$$\mathbf{H}' = \mathbf{U}\mathbf{\Lambda}\mathbf{V}^*,\tag{3.15}$$

where $\mathbf{U}\in\mathcal{R}^{N_r \times N_r}$ and $\mathbf{V}\in\mathcal{R}^{N_t \times N_t}$ are unitary matrices, and $\mathbf{\Lambda}\in\mathcal{R}^{N_r \times N_t}$ is a rectangular matrix whose diagonal elements are non-negative real numbers and whose off-diagonal elements are zero. The diagonal elements $\lambda_1 \geq \lambda_2 \geq \cdots \geq \lambda_{n_{min}}$ are the ordered singular values of the channel matrix $\mathbf{H}'$, where $n_{min} = \min(N_t, N_r)$. Each λ_i corresponds to an eigen-mode of the channel and each non-zero eigen-mode can support a data stream. The MIMO channel capacity can be written as:

$$C = \sum_{i=1}^{n_{min}} log_2(1 + \frac{E\lambda_i^2}{N_t W \sigma^2}) \quad \text{bits/s/Hz}\tag{3.16}$$

where σ_2 is noise PSD and W is the system bandwidth. Its upper bound can be found based on Jensen's inequality

$$\frac{1}{k}\sum_{i=1}^{k} log_2\left(1 + \frac{E\lambda_i^2}{\sigma^2}\right) \leq log_2\left(1 + \frac{E}{\sigma^2}\left(\frac{1}{k}\sum_{i=1}^{k}\lambda_i^2\right)\right)\tag{3.17}$$

where k is the number of non-zero singular values, and

$$\sum_{i=1}^{k} \lambda_i^2 = \text{Tr}\left[\mathbf{H}'\mathbf{H}'^*\right] = \sum_{i,j} |h_{i,j}|^2, \tag{3.18}$$

The smaller the condition number $\max(\lambda_i)/\min(\lambda_i)$ of the channel matrix, the larger the capacity.

3.3.3   Simulation results

We adopt the same room configuration as that in [34] and summarized in Table I to evaluate the non-imaging MIMO channel capacity. Assume the total average transmitted optical power is fixed and divided equally among the LED arrays which are uniformly placed on the ceiling.

Table 3.1: Parameters for non-imaging MIMO simulations.

Parameters	Values
Room size (length*width*height)	5m*5m*3m
Tx-Rx vertical distance	2.15m
Total average transmitted optical power in blue band	14.4W
LED transmission Lambertian order	1
Active receiving area of the photodetector with lens	1cm^2
Optical bandpass filter transmittance	0.75
Receiver photodetector FOV (half angle)	90^0
Photodetector responsivity (blue)	0.21A/W
Thermal noise density	$5\text{pA}/\sqrt{\text{Hz}}$
System bandwidth	10MHz

The received SNR varies with the receiver position inside the room, leading to
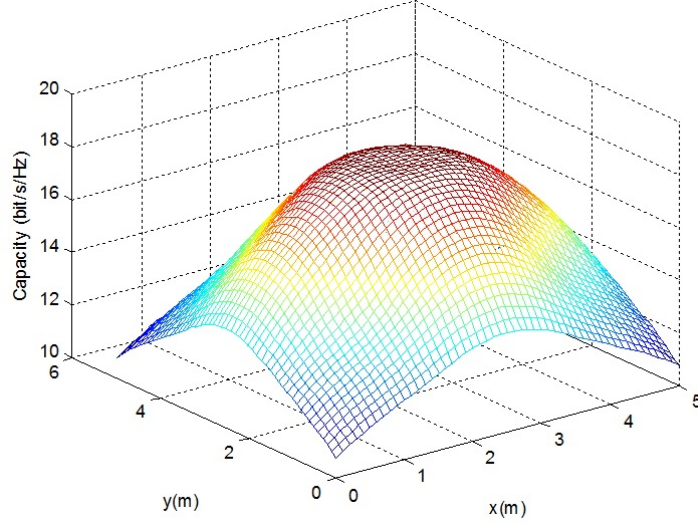
Figure 3.11: Non-imaging MIMO channel capacity distribution within the room.

the corresponding channel capacity variation. The simulation result with 2×2 transmitting LED arrays and a 2×2 receiving photodetector array (photodetector separation is 10cm) is shown in Fig. 3.11. It's observed that an average of 15bit/s/Hz could be achieved in a typical illuminated office environment. Fig. 3.12 shows the effect of photodetector separation, assuming the photodetector is placed at the room center. A monotonic increase is observed attributed to improved channel condition for increased separation.

Next we examine the effects of the number of transmitters Nt and receivers Nr. Fig. 3.13(a) shows the capacity with a 4×4 receiving photodetector array at different receiver positions. It's observed that in the center area of the room, the channel capacity decreases with increased N_t due to the decreased SNR. While near the corner area, the channel capacity first increases and then decreases slowly. The situation is quite different for varying N_r. With 4×4 LED transmitting arrays, almost linear capacity increase is observed from Fig. 3.13(b). These parameters largely affect the degree of freedom
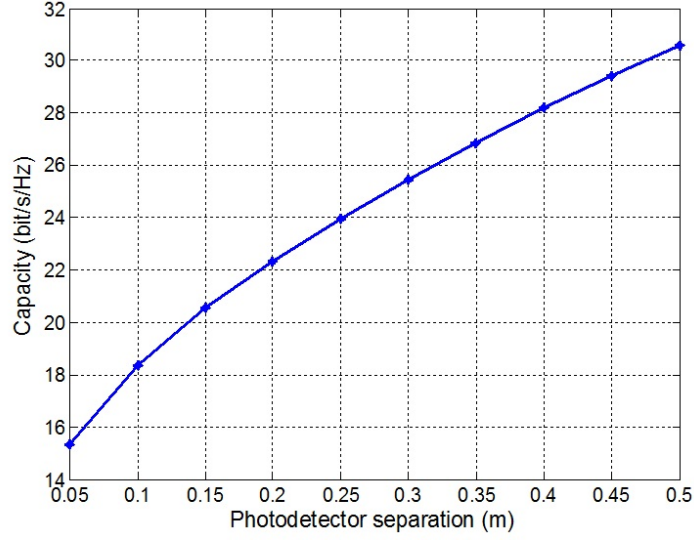
Figure 3.12: Non-imaging MIMO channel capacity variation with the receiving photodetector antenna separation.

provided by the MIMO channel and thus the channel capacity.

Similarly, we study the imaging MIMO channel capacity. Parameters used for evaluation are the same as Tab. 3.1 plus that the LED array size is assumed to be $0.4m \times 0.4m$ and the magnification factor M is 1075. For ease of analysis, assume $h_{imag}(x,y) = \delta(x,y)$, which means the images of the LED arrays are determined merely by the geometric optics. Fig. 3.14 shows channel capacity variation at different receiver positions corresponding to $N_t = 4$, $N_r = 16$. Different from the non-imaging MIMO channel capacity, notches appear at certain locations where the channel capacity decreases drastically. This is determined by the imaging nature of the receiver front-end. At positions where notches appear, the images of the transmitting LED arrays are divided equally between two pixels and the degrees of freedom provided by the imaging MIMO channel decrease dramatically.

Next, effects of N_t and N_r are also studied. First, set $N_r = 16$ and vary N_t from 4 to 36. The capacity at different receiver positions is shown in Fig. 3.15(a). The
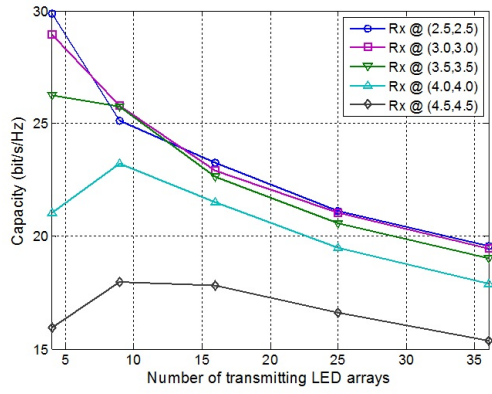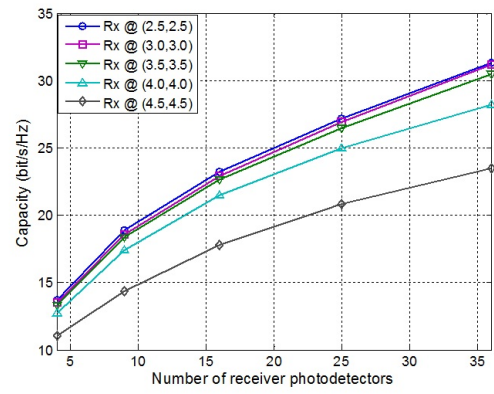
a. Effect of the number of transmitting antennas.   b. Effect of the number of receiving antennas.

Figure 3.13: Effect of the number of transmitting and receiving antennas on the non-imaging MIMO channel capacity.
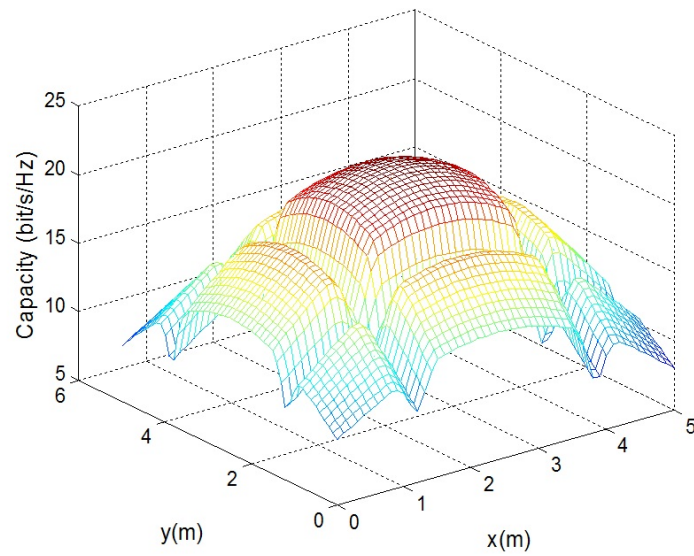
Figure 3.14: Imaging MIMO channel capacity distribution within the room.
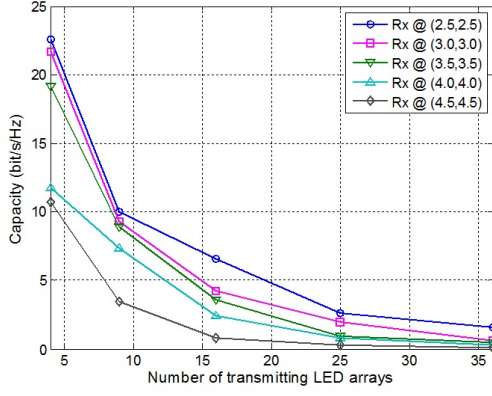
a. Effect of the number of transmitting antennas.
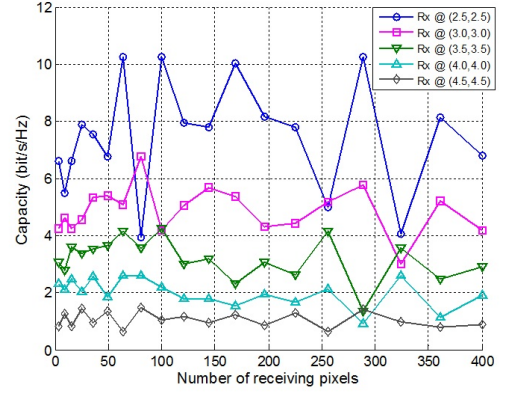
b. Effect of the number of receiving antennas.

Figure 3.15: Effect of the number of transmitting and receiving antennas on the imaging MIMO channel capacity.

channel capacity decreases rapidly as N_t increases. In our simulation, the pixel size is much larger than the LED array image. As N_t increases, more images fall on the same pixel and the channel condition becomes worse. If $N_t = 16$ and N_r varies from 4 to 400, capacity at each of different receiver locations fluctuates around certain mean level as seen in Fig. 3.15(b). Fluctuations decrease as the receiver moves away from the room center.

Chapter 4

Optical Femtocell: An Indoor Multiuser Access Scheme

In the previous chapters, an indoor VLC link has been characterized and transceiver design techniques have been discussed to boost the link data rate and improve the system performance. In practical indoor application scenarios, multiple users usually reside within the same room simultaneously. A multiuser access scheme is therefore needed to accommodate different users. Meanwhile, due to the interference issues in the deployment of current femtocell systems, such VLC multiuser access solution is promising as a new physical layer implementation technology.

4.1 Introduction

With popularity of smart phones and diverse multimedia internet access services, there have been ever increasing subscribers worldwide. Despite the rapid advancement of the cellular networks, their coverage and quality of service (QoS) still can not be guaranteed everywhere, especially in the area where subscribers are densely populated.

As an effective solution, femtocell has been proposed and gradually deployed as micro-basestations at home and in office buildings [72]. However, one critical challenge in deploying a femtocell system is the interference between the femtocell and the macrocell networks [72, 73, 74], that has significantly limited the system capacity.

In this chapter, a new physical layer is proposed for the implementation of a femtocell system utilizing lighting LED based visible light communication (VLC) [9]. Indoor VLC has several unique advantages that make it appropriate for the femtocell network. Firstly, it's piggybacked on LED lighting, rapidly penetrating the indoor lighting market and providing ubiquitous coverage [2]. Such an optical femtocell network can therefore be easily deployed wherever lighting LEDs are adopted for the general illumination. Secondly, VLC uses the lighting LEDs as the transmitters almost for free. Most cost is invested on installation of lighting infrastructure. Lastly but most importantly, VLC utilizes light as the transmission carrier. It does not introduce interference to the existing cellular networks. Due to confined beaming, LED light from different femtocells minimally interferes each other, in not only cells blocked by walls but also adjacent cells. Therefore, VLC with densely distributed LEDs provides large communication coverage while each confined area is served at maximum throughput.

Since the proposed optical femtocell system is overlaid on a lighting system, the lighting control functions shouldn't be compromised by the communication function. One typical lighting control function is dimming control [75]. To ensure it compatability, the IEEE standard defines a new modulation scheme, the variable-PPM (VPPM) modulation [8]. Multiple channel reuse strategies have been proposed for indoor optical wireless communication systems, including time division multiple access (TDMA), frequency division multiple access (FDMA), code division multiple access (CDMA) [76, 77], and wavelength division multiple access (WDMA) [78]. To consider femtocell applica-
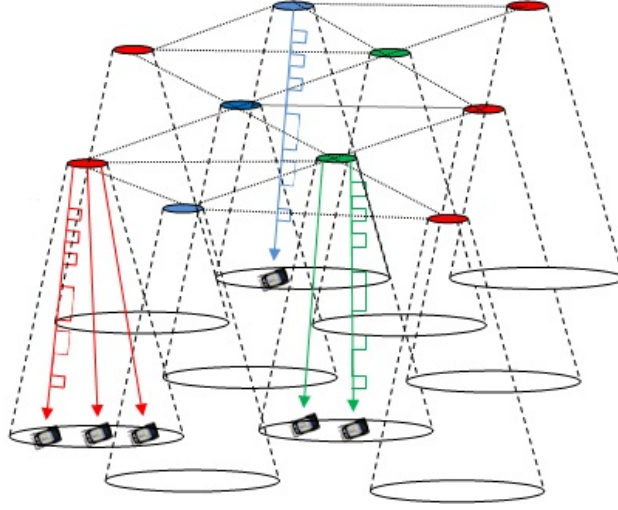
Figure 4.1: General structure of an indoor VLC optical femtocell system.

tions in the current context and better mitigate interference from different femtocells, a combined wavelength division and code division multiple access scheme is proposed.

The remainder of this chapter is organized as follows. In Section 4.2, the general structure of the proposed indoor optical femtocell system is presented. Then the system performance is theoretically analyzed in Section 4.3. In Section 4.4, the Monte-Carlo simulation is adopted to numerically evaluate the system performance under typical settings and reveal the effects of various parameters.

4.2   General System Structure

The general system architecture of an indoor VLC optical femtocell system is shown in Fig. 4.1. Multiple LED lamps are mounted on the ceiling, each transmitting the desired information to mobile users underneath the LED lamp. Each LED lamp can be treated as a micro-basestation and the major covering area of an LED lamp is defined as an "optical femtocell". The entire indoor room environment therefore

contains multiple cells.

Within each cell, it may occur that multiple mobile terminals reside at the same time. The orthogonal code, Walsh-Hadamard (WH) code, is adopted for user differentiation within a cell and minimize intracell interference. Each user is assigned a unique WH code of the same length. The transmission beam pattern of the lighting LED is usually wide (e.g. a beam angle of 120^0 in the Lambertian radiation pattern), causing intercell interference at the receiver side. To mitigate such interference, a two-fold strategy jointly employing color (wavelength) and code is proposed. The first fold is to use different wavelength channels for adjacent cells. Multi-color white LEDs may be an option for illumination such as RGB white LEDs on the LED market. Each LED integrates multiple LED chips, with each chip providing one color. Among all colors, one color can be selected to carry useful information for communication while all other colors are reserved for illumination. To ensure white color for illumination, the average intensity for the information-carrying color is adjusted to equal each of other colors for illumination. As an example, each RGB LED can provide three optical carrier wavelengths, namely red (620nm), green (525nm), and blue (470nm) as shown in Fig. 4.2. As in cell planning for a cellular system, LEDs of different information-carrying colors are arranged on the vertices of equilateral triangles, as shown in Fig. 4.3. Due to the orthogonality of different wavelength channels, the intercell interference from the 6 nearest neighboring LEDs is eliminated. If we focus on one particular wavelength channel, the LED arrangement is similar to the hexagonal cell arrangement adopted in cellular networks with cluster size $N = 1$ [79]. The second fold is to assign phase-shifted maximum-length PN sequences (m-sequences) to neighboring LEDs sharing the same wavelength channel. Based on the above design principles, the code sequence for
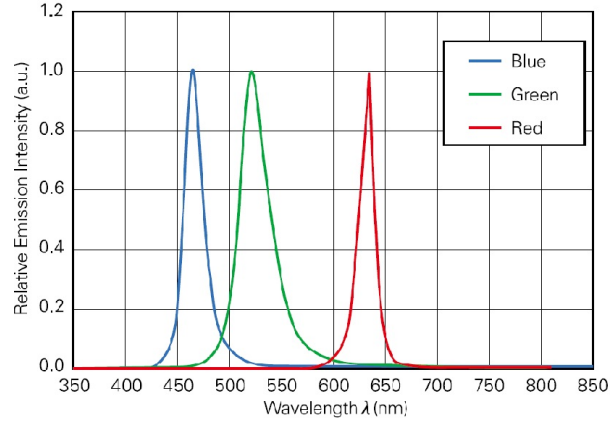
Figure 4.2: Optical power spectrum of a typical three-chip RGB LED.
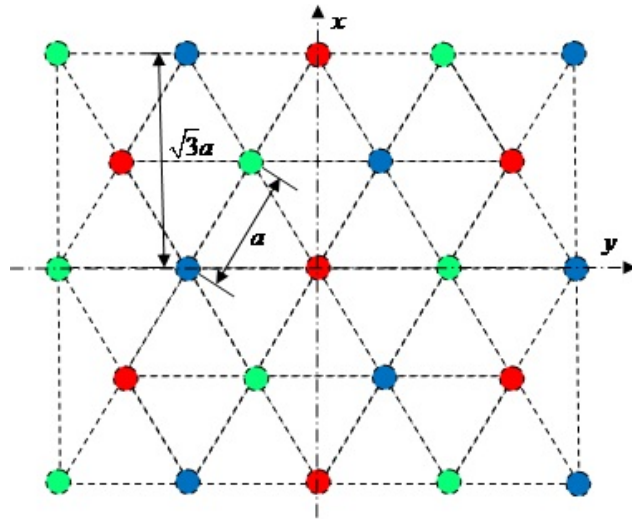
Figure 4.3: LED arrangement on the ceiling for wavelength division multiple access.

each LED is a concatenated orthogonal/PN sequence. The orthogonal WH code is to distinguish different users within the same cell, while the PN sequence is to distinguish different femtocells sharing the same carrier wavelength.

The cell size is defined as the coverage area within which the link quality of service (QoS) between the mobile user and the transmitting LED meets the requirement, for example, the transmission BER being lower than 10^{-5}. As a result, the cell coverage overlaps based on the definition. Once a link is established between the mobile user and a transmitting LED, the link will be maintained as long as the link QoS requirement is satisfied. If the link QoS drops below the pre-specified level during the user movement, a soft "handover" is achieved to shift the link from one cell to another. If the handover location is within the overlapping area of multiple cells, a comparison will be made to choose the link with the largest signal strength.

As mentioned earlier, the indoor VLC is piggybacked on the illumination system. Thus the communication should not impair the normal illumination functions, for example the dimming control. The IEEE802.15.7 standard defines a variable-PPM (VPPM) modulation scheme which is compliant with the typical dimming control technique, pulse width modulation (PWM) [8]. In our scheme, the VPPM modulated signal is applied to one color of the three color LED chips. To maintain the spectrum of the emitted white light from the three-chip LEDs, the average output optical power of three colors must be kept the same. Therefore PWM modulation is applied to the other two unmodulated LED chips to ensure the same power level as the VPPM carrier. The PWM symbol repetition rate is designed to be much lower than the VPPM chip rate, so that the interference from the PWM dimming sequences and the transmitted VPPM signal can be differentiated in the frequency domain. Corresponding filters could be designed for such fixed interference cancelation [80].

The piggybacked VLC provides a convenient way for information broadcasting or downlink transmission from LEDs to a mobile terminal. For the uplink of an indoor VLC optical femtocell system, multiple options have been proposed [45, 46, 54], but no general consensus has been reached for the uplink choice. In the rest of the chapter we only consider the performance of the downlink from the transmitting LEDs to the mobile terminal.

4.3 System Performance Analysis

4.3.1 Transmitted signal model

As discussed in the previous section, the concatenated orthogonal/PN code is used as the spreading sequence. Assume the period of the long PN sequence d_l assigned to cell l is P and that of the Walsh-Hadamard code assigned to the kth user in cell l $w_l^{(k)}$ is N, the concatenated code sequence for the kth user in cell l can be expressed as $c_{l,j}^{(k)} = d_{l,j+k_l'} w_{l,j}^{(k)}, j = -\infty, ..., +\infty$, where $d_{l,j}, w_{l,j}^{(k)}, c_{l,j}^{(k)} \in \{-1, 1\}$, k_l' is the phase shift of the m-sequence adopted for cell l, and j is the index of the bit sequence. The code spreading procedure is as follows. The unipolar binary information bit sequence $s_{l,j}^{(k)} \in \{0, 1\}$ from the lth LED to the kth user is first converted to a bipolar bit sequence $s_{l,j}^{(k)'} \in \{-1, 1\}$ through $s_{l,j}^{(k)'} = 2s_{l,j}^{(k)} - 1$. Then this bit sequence is code spread by the concatenated code sequence $c_{l,j'}^{(k)}$, $a_{l,j'}^{(k)} = s_{l,\lfloor j'/N \rfloor}^{(k)'} \cdot c_{l,j'}^{(k)}, j' = -\infty, ..., +\infty$, where j' is chip index. At last, this code spread bit sequence is modulated according to the VPPM modulation scheme.

Suppose the maximum supported user number within a cell is K and the chip

time for a single code bit is T_c. The signal transmitted by the lth LED is

$$s_l(t) = \sum_{k=1}^{K} \lambda_{l,k} s_l^{(k)}(t), \qquad (4.1)$$

$$s_l^{(k)}(t) = \sum_{j=-\infty}^{j=+\infty} P_l \psi_l(t - jT_c - e_{l,j}^{(k)} \delta_l), \qquad (4.2)$$

where $\lambda_{l,k}$ is a random variable that accounts for the activity factor of the transmission, for example, $\lambda_{l,k} = 1$ with probability η and $\lambda_{l,k} = 0$ with probability $1 - \eta$, P_l is the transmitted optical power from the modulating chip for each user within a cell, $e_{l,j}^{(k)} = (1 + a_{l,j}^{(k)})/2$, and δ_l is the time shift induced by the VPPM modulation. Here the transmitted optical power for each user is chosen based on the transmit balancing where the available power at the transmitting LED is allocated equally among the users. If no user is present within the cell, low repetition rate PWM dimming sequences will be transmitted, and the correspondingly induced interference can be minimized using the interference cancelation technique mentioned in the previous section. The pulse waveform is chosen to be a rectangular pulse,

$$\psi_l(t) = rect(\frac{t}{w_l}), \quad rect(t) = \begin{cases} 1, & 0 < t < 1 \\ 0, & otherwise \end{cases} \qquad (4.3)$$

where w_l is the pulse width representing the time interval when the light is turned on. The time shift of the VPPM modulation is therefore written as $\delta_l = T_c - w_l$. The dimming level could correspondingly be represented as $D_l = 1 - w_l/T_c$. In order to guarantee the communication performance using VPPM modulation, the dimming level could not be made arbitrarily small or large compared to those realized by PWM dimming control. Therefore a limit is set for the dimming level resolution of the VPPM symbols, 10% as defined in the IEEE802.15.7 standard, which implies that w_l could only take on values as $0.1nT_c$, $n = 1, 2, 3...9$. However, a more sophisticated algorithm is also

79

proposed in the standard to support a dimming resolution of 0.1% using the dimming level resolution limited VPPM symbols.

4.3.2 Channel model

The indoor VLC channel consists of two types of links, namely the line-of-sight (LOS) link and the non-line-of-sight (NLOS) diffuse link [10]. Compared with the LOS link, the received optical power from the NLOS link is usually much smaller. Therefore only the LOS link is considered and contributions from NLOS links are neglected [61]. For Lambertian radiation pattern of the transmitting LED, the path loss can be written as

$$\alpha = \frac{(m+1)A_r}{2\pi D^2} \cos \varphi \cos^m \beta, \tag{4.4}$$

where m is the order of Lambertian emission, A_r is the active receiving area, D is the transmitter-receiver distance, φ is the incident angle at the receiver front-end, and β is the emission angle from the transmitter. The channel impulse response is a time delayed delta function,

$$h(t) = \delta(t - \tau). \tag{4.5}$$

Data symbols synchronized at the transmitter will undergo the same time delay and remain synchronized at the receiver front-end.

4.3.3 Received signal model

Assume appropriate optical bandpass filters are adopted at the receiver front-end, and intercell interference from other neighboring cells adopting different wavelength carriers are ignored. We only consider intracell interference from other users within the same cell and intercell interference from other neighboring cells adopting the same wavelength carriers within the room. Without loss of generality, assume transmitter

TX1 transmits desired information to a synchronized receiver RX1. The received signal is contributed by the desired user, $(K-1)$ interfering users within the same cell, and all users from other $(L-1)$ neighboring cells sharing the same wavelength channel. It is described by

$$r(t) = r_u(t) + r_{intracell}(t) + r_{intercell}(t) + n(t), \tag{4.6}$$

where $n(t)$ is noise. Within a bit interval $[0, T_b]$ of duration $T_b = NT_c$, these contributions have the following forms

$$r_u(t) = \sum_{j=0}^{N-1} \alpha_1 \varepsilon_1 P_1 \psi_1(t - jT_c - e_{1,j}^{(1)} \delta_1), \tag{4.7}$$

$$r_{intracell}(t) = \sum_{k=2}^{K} \sum_{j=0}^{N-1} \lambda_{1,k} \alpha_1 \varepsilon_1 P_1 \psi_1(t - jT_c - e_{1,j}^{(k)} \delta_1), \tag{4.8}$$

$$r_{intercell}(t) = \sum_{l=2}^{L} \sum_{k=1}^{K} \sum_{j=-\infty}^{+\infty} \lambda_{l,k} \alpha_l \varepsilon_l P_l \psi_l(t - jT_c - e_{l,j}^{(k)} \delta_l - \tau_l), \tag{4.9}$$

where α_l and τ_l are the path loss and time delay from the lth LED to the receiver respectively, ε_l is the receiving photodiode responsivity (A/W).

The receiver makes a decision based on the received signal in the time interval $[0, T_b]$ and a locally generated correlation mask defined as

$$m(t) = \sum_{j=0}^{N-1} c_{1,j}^{(1)} v(t - jT_c), \quad v(t) = \psi_1(t - \delta_1) - \psi_1(t). \tag{4.10}$$

The correlator output becomes

$$Z = \int_0^{T_b} r(t)m(t)dt. \tag{4.11}$$

Here we assume the dimming level of the reference transmitting LED TX1 is known at the receiver, and therefore the correlation mask is made up of the same pulse transmitted from the reference TX LED. Combining eqs. (4.6)-(4.10), (4.11) can be rewritten as

$$Z = Z_u + Z_{intracell} + Z_{intercell} + Z_n, \tag{4.12}$$

where Z_u, $Z_{intracell}$, $Z_{intercell}$, and Z_n represent the useful signal, the intracell interference, the intercell interference, and noise at the receiver output. Each of these contributions will be expressed next.

The useful signal component at the receiver output contributed by all N pulses within the desired one bit interval can be expressed as

$$Z_u = \int_0^{T_b} r_u(t)m(t)dt = N\alpha_1\varepsilon_1 P_1 q_0^{(1)} s_{1,0}^{(1)'} \left(1 - R_0^{(1)}(\delta_1)\right), \tag{4.13}$$

where $q_0^{(1)}$ is the basic pulse energy with $q_0^{(1)} = \int_0^{T_c} \psi_1^2(t)dt$, $s_{1,0}^{(1)'}$ is the transmitted bit with a value of 1 or -1, and $R_0^{(1)}(t)$ is the autocorrelation function of the energy normalized pulse waveform $\frac{1}{\sqrt{q_0^{(1)}}}\psi_1(t)$. Its detailed derivation can be found in Appendix .1.

The intracell interference $Z_{intracell}$ is proved to be zero under our system configuration, as shown in Appendix .1. The intercell interference is given by

$$\begin{aligned} Z_{intercell} &= \int_0^{T_b} r_{intercell}(t)m(t)dt \\ &= \sum_{j=0}^{N-1} c_{1,j}^{(1)}(Y_j' - Y_j) \\ &= \sum_{l=2}^{L} \alpha_l\varepsilon_l P_l \sum_{k=1}^{K} \int_0^{T_b} \sum_{j=-\infty}^{j=+\infty} \lambda_{l,k}\psi_l(t - jT_c - e_{l,j}^{(k)}\delta_l - \tau_l)\cdot \sum_{i=0}^{N-1} c_{1,i}^{(1)}v(t - iT_c)dt, \end{aligned}$$

$$\tag{4.14}$$

where

$$\begin{aligned} Y_j &= \int_{jT_c}^{(j+1)T_c} \psi_1(t - jT_c)r_{intercell}(t)dt, \\ Y_j' &= \int_{jT_c}^{(j+1)T_c} \psi_1(t - jT_c - \delta_1)r_{intercell}(t)dt. \end{aligned} \tag{4.15}$$

needs to be characterized. As stated earlier, TX LED1 is chosen to be the LED of interest and it's assumed $\tau_1 = 0$. The timing offsets of other interfering LEDs are τ_l, $l = 2, 3, ..., L$, which are assumed to be independent of each other and uniform over the

interval $0 < \tau_l < T_b$. Define $x_l = \lfloor \frac{\tau_l}{T_c} \rfloor$ and $y_l = \tau_l - x_l T_c$, and we can observe that $x_l = 0, 1, ..., N-1$ with probability $\frac{1}{N}$ and y_l is uniform over $(0, T_c)$.

As shown in eq. (4.3), the rectangular pulse is adopted at the transmitter and if it's assumed that the LED turn-on and turn-off time $\tau_{on}, \tau_{off} \ll T_c$, the expression for Y_j' and Y_j is derived as:

$$
\begin{aligned}
Y_j &= \sum_{l=2}^{L} \sum_{k=1}^{K} \frac{1 - a_{l,j-x_l}^{(k)}}{2} \lambda_{l,k} \alpha_l \varepsilon_l P_l \times o_1 + \sum_{l=2}^{L} \sum_{k=1}^{K} \frac{1 + a_{l,j-x_l}^{(k)}}{2} \lambda_{l,k} \alpha_l \varepsilon_l P_l \times o_2 \\
&+ \sum_{l=2}^{L} \sum_{k=1}^{K} \frac{1 - a_{l,j-x_l-1}^{(k)}}{2} \lambda_{l,k} \alpha_l \varepsilon_l P_l \times o_3 + \sum_{l=2}^{L} \sum_{k=1}^{K} \frac{1 + a_{l,j-x_l-1}^{(k)}}{2} \lambda_{l,k} \alpha_l \varepsilon_l P_l \times o_4 \\
Y_j' &= \sum_{l=2}^{L} \sum_{k=1}^{K} \frac{1 - a_{l,j-x_l}^{(k)}}{2} \lambda_{l,k} \alpha_l \varepsilon_l P_l \times o_1' + \sum_{l=2}^{L} \sum_{k=1}^{K} \frac{1 + a_{l,j-x_l}^{(k)}}{2} \lambda_{l,k} \alpha_l \varepsilon_l P_l \times o_2' \\
&+ \sum_{l=2}^{L} \sum_{k=1}^{K} \frac{1 - a_{l,j-x_l-1}^{(k)}}{2} \lambda_{l,k} \alpha_l \varepsilon_l P_l \times o_3' + \sum_{l=2}^{L} \sum_{k=1}^{K} \frac{1 + a_{l,j-x_l-1}^{(k)}}{2} \lambda_{l,k} \alpha_l \varepsilon_l P_l \times o_4'
\end{aligned}
\tag{4.16}
$$

where

$$o_1 = \begin{cases} w_l, & 0 < y_l \leq \max(w_1 - w_l, 0) \\ \\ w_1 - y_l, & \max(w_1 - w_l, 0) < y_l \leq w_1 \\ \\ 0, & w_1 < y_l < T_c \end{cases},$$

$$o_2 = \begin{cases} w_1 + w_l - T_c - y_l, & 0 < y_l \leq w_1 + w_l - T_c \\ \\ 0, & w_1 + w_l - T_c < y_l < T_c \end{cases},$$

$$o_3 = \begin{cases} 0, & 0 < y_l \leq T_c - w_l \\ \\ w_l + y_l - T_c, & T_c - w_l < y_l \leq T_c + \min(w_1 - w_l, 0) \\ \\ w_1, & T_c + \min(w_1 - w_l, 0) < y_l < T_c \end{cases},$$

$$o_4 = \begin{cases} y_l, & 0 < y_l \leq \min(w_1, w_l) \\ \\ \min(w_1, w_l), & \min(w_1, w_l) < y_l \leq \max(w_1, w_l) \\ \\ w_1 + w_l - y_l, & \max(w_1, w_l) < y_l < w_1 + w_l \\ \\ 0, & w_1 + w_l < y_l < T_c \end{cases};$$

(4.17)

and

$$o'_1 = \begin{cases} 0, & 0 < y_l \leq T_c - w_1 - w_l \\ y_l + w_1 + w_l - T_c, & T_c - w_1 - w_l < y_l \leq T_c - \max(w_1, w_l) \\ \min(w_1, w_l), & T_c - \max(w_1, w_l) < y_l \leq T_c - \min(w_1, w_l) \\ 0, & T_c - \min(w_1, w_l) < y_l < T_c \end{cases},$$

$$o'_2 = \begin{cases} w_1, & 0 < y_l \leq \max(w_l - w_1, 0) \\ w_l - y_l, & \max(w_l - w_1, 0) < y_l \leq w_l \\ 0, & w_l < y_l < T_c \end{cases},$$

$$o'_3 = \begin{cases} 0, & 0 < y_l \leq 2T_c - w_1 - w_l \\ y_l + w_1 + w_l - 2T_c, & 2T_c - w_1 - w_l < y_l < T_c \end{cases},$$

$$o'_4 = \begin{cases} 0, & 0 < y_l \leq T_c - w_1 \\ y_l + w_1 - T_c, & T_c - w_1 < y_l \leq T_c + \min(w_l - w_1, 0) \\ w_1, & T_c + \min(w_l - w_l, 0) < y_l < T_c \end{cases}.$$

(4.18)

The physical meaning of Y_j can be observed from Fig. 4.4. The top rectangular shows the pulse of $\psi_1(t - jT_c)$ and the bottom one shows two interfering pulses from other cells. Each interfering pulse is toward either the beginning or the end of the chip interval, which is differentiated using the solid and dotted lines. The interference introduced by the interfering pulse $\psi_l(t - jT_c - x_lT_c)$ is represented by the first two items of the summation including o_1 and o_2, and that by the interfering pulse $\psi_l(t - jT_c - x_lT_c - 1)$ is represented by the last two items including o_3 and o_4. The expression of Y'_j can be interpreted similarly.
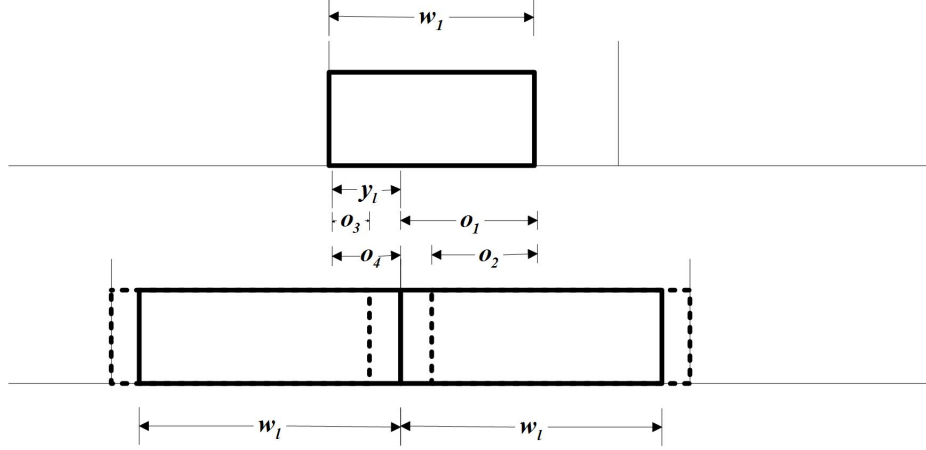
Figure 4.4: Illustration of the intercell interference.

Received signals are corrupted by the additive noise, which is a combination of the shot noise induced by the ambient light within the room and the thermal noise from the receiver front-end. The shot noise in a direct-detection system is often modeled by a signal-dependent, Poisson-rate photon counting model. However, in an indoor VLC system, incoherent propagation and the high intensity of the background light make the shot noise independent of the signal. This enables us to model it with extremely high accuracy as an additive white Gaussian noise (AWGN) with single-side power spectral density (PSD) N_{shot} (A^2/Hz), referred to the input of the preamplifier [53]. The PSD of the thermal noise is denoted as N_{th}, which is also modeled as an AWGN. The PSD of the total noise is represented as $N_0 = N_{shot} + N_{th}$. The receiver correlation output induced by the noise Z_n is written as:

$$Z_n = \sum_{j=0}^{N-1} \int_{jT_c}^{(j+1)T_c} c_{1,j}^{(1)} n(t) v(t - jT_c) dt = \sum_{j=0}^{N-1} c_{1,j}^{(1)} (n_{j,1} - n_{j,0}), \qquad (4.19)$$

where $n_{j,1} = \int_{jT_c}^{(j+1)T_c} n(t)\psi_1(t - jT_c - \delta_1)dt$ and $n_{j,0} = \int_{jT_c}^{(j+1)T_c} n(t)\psi_1(t - jT_c)dt$, with variances $\sigma_{n_{j,1}}^2 = \sigma_{n_{j,0}}^2 = N_0 q_0^{(1)}$. Define $x_j = n_{j,1} - n_{j,0}$. It can be proved that each x_j

is also a Gaussian random variable with the variance $\sigma_{x_j}^2$ derived as:

$$
\begin{aligned}
\sigma_{x_j}^2 &= 2N_0 q_0^{(1)} + 2\mathrm{Cov}(n_{j,1}, -n_{j,0}) \\
&= 2N_0 q_0^{(1)} - 2 \int_0^{T_c} \int_0^{T_c} \langle n(\tau_1) n(\tau_0) \rangle \psi_1(\tau_1 - \delta_1) \psi_1(\tau_0) d\tau_1 d\tau_0 \\
&= 2N_0 q_0^{(1)} - 2N_0 \int_0^{T_c} \psi_1(\tau_1 - \delta_1) \psi_1(\tau_1) d\tau_1 \\
&= 2N_0 q_0^{(1)} \big(1 - R_0^{(1)}(\delta_1)\big),
\end{aligned}
\tag{4.20}
$$

where $\langle \cdot \rangle$ represents the expectation, and $\langle n(\tau_1) n(\tau_0) \rangle = \delta(\tau_1 - \tau_0)$ in our case. Since each x_j is independent and the code bit $c_{j,1}$ takes values of 1 or -1, the variance of Z_n is

$$
\sigma_{Z_n}^2 = 2N N_0 q_0^{(1)} \big(1 - R_0^{(1)}(\delta_1)\big).
\tag{4.21}
$$

Up to now, we have analyzed each component in the correlation receiver output shown in eq. (4.12). The obtained output is compared against the threshold, zero as in our case, and a decision is made based on the comparison result. As can be observed from eq. (4.16), the intercell interference is conditioned on multiple random variable parameters, including the timing offsets τ_l of different cells, transmitting LEDs dimming level (related to w_l), the number of users within the cells (decided by $\lambda_{l,k}$), and the transmitting bits from different LEDs (affecting $a_{l,j-x_l}^{(k)}$ and $a_{l,j-x_l-1}^{(k)}$). Given certain realizations of those parameters, the intercell interference is fixed together with the useful signal component. The average bit error rate (BER) at the receiver therefore can be expressed as:

$$
BER = E\left[Q\left(\sqrt{\frac{(Z_u + Z_{intercell})^2}{\sigma_{Z_n}^2}} \right) \right],
\tag{4.22}
$$

where the expectation is taken over all those random variable parameters.

4.4 System Performance Evaluation

In this section numerical results will be presented for the performance of the proposed indoor optical femtocell system in a large office room with multiple LED lamps mounted on the ceiling. Each LED lamp is consisted of arrays of white LEDs, which are assumed to be RGB white LEDs with spectrum as shown in Fig. 4.2, and the output lumen of a single LED lamp is 1620 lm. The LED lamps are distributed in the way as shown in Fig. 4.3 with the nearest LED lamp distance $a = 2$ m. Here the LED lamp radiation pattern is assumed to be Lambertian for ease of analysis. The photodiode receiver is pointed straight upward towards the ceiling with a vertical separation of 2 m. With this configuration, the illumination level is calculated to be within the typical illumination level of 300~500 lx required for the office environment at the height of the receiver, as shown in Fig. 4.5. Optical bandpass filters are adopted at the receiver front-end to separate different wavelength channels. Since each wavelength channel exhibits similar behavior with no significant difference, only the blue wavelength channel (470 nm) is considered here. A blue optical filter with a bandwidth of 40 nm and a transmittance of 0.75 is adopted. The responsivity ε of the PD is assumed to be 0.21 A/W for the blue optical band.

Here we assume the maximum number of users K that a cell supports is 3. A 8×8 WH code matrix is generated by the computer and each user within a cell is assigned a unique line of the matrix as the code. Phase-shifted m-sequences of length $2^{11} - 1$ are assigned to different cells to mitigate the intercell interference. It's assumed here the phase shift of the m-sequence equals the length of the WH code. Different optical clock rates are proposed in the IEEE standard [8], extending from 200 kHz to 120 MHz to support a broad class of optical transmitters (LEDs). Therefore here various
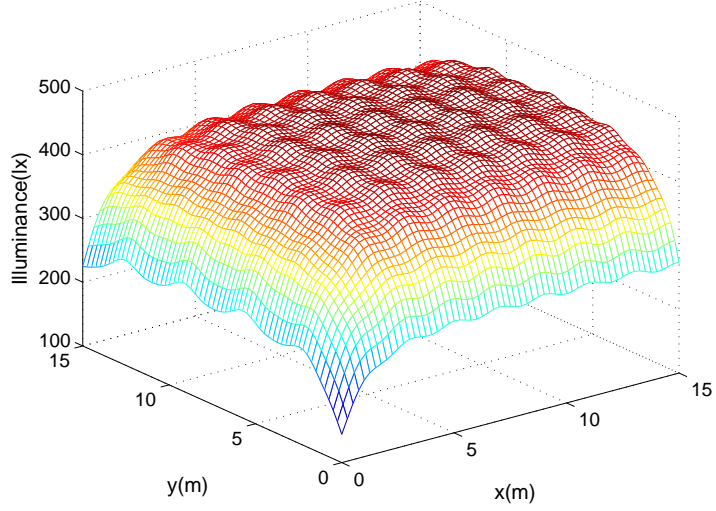
Figure 4.5: Illuminance distribution within the room.

chip rates, namely 50, 75, and 100 Mcps, are selected for performance evaluation, which are equivalent to user data rates of 6.25 Mbps, 9.375 Mbps, and 12.5 Mbps respectively. We assume the LED combined with some pre-equalization techniques can support the maximum data rate under consideration [19, 21] and the LED turn-on and turn-off time $\tau_{on}, \tau_{off} \ll T_c$. The power spectral density (PSD) of the thermal noise from the receiver front-end preamplifier is taken as $N_{th} = 4 \times 10^{-24}$ A^2/Hz, and that of the shot noise is determined by the total received optical power at the receiver as $N_{shot} = 2q\varepsilon P_r$, where P_r is the total received optical power at the receiver. Typical parameter values used for simulation are summarized in Tab. 4.1.

4.4.1 Determination of the cell area

As stated in Section 4.2, the cell area is defined as the area where the link BER is maintained below 10^{-5}. Suppose the vertical height of the receiver is fixed, as the receiver moves away from the target LED, the received signal strength decreases and the

89

Table 4.1: Parameters for system performance evaluation.

Nearest LED distance	2 m
LED lamp luminosity	1620 lm
Tx-Rx vertical distance	2 m
Filter center wavelength, bandwidth, transmittance	470 nm, 40 nm, 0.75
Photodiode active receiving area	1 cm^2
Photodiode responsivity	0.21 A/W
Walsh-Hadamard code length	8
m-sequence length	$2^{11} - 1$
Maximum number of users within a cell	3
PSD of receiver front-end thermal noise	2×10^{-12} A/$\sqrt{\text{Hz}}$

intercell interference increases. For a Lambertian radiation pattern of the transmitting LED, the path loss variation with the horizontal separation increase is shown in Fig. 4.6. It can be observed from Fig. 4.3 that as the receiver moves away from the target LED along the x-axis and y-axis, the received intercell interference varies differently because of the arrangement of the LED. Monte-Carlo simulations have been carried out to reveal the difference. The dimming level of the target LED is chosen to be 0.5 and those of the other LEDs are chosen from $0.1n, n = 1, 2, ..., 9$ with equal probability. We also assume there is only one user within the target cell and therefore the available transmit power is fully dedicated to the target user. The average BER variations with the horizontal separation increase along the x-axis and y-axis are shown in Fig. 4.7. The maximum Tx-Rx horizontal separations for the link to maintain a BER lower than 10^{-5} along the x-axis and y-axis are 1.8 m and 2 m respectively.

It can be observed that the link performance remains the same with different
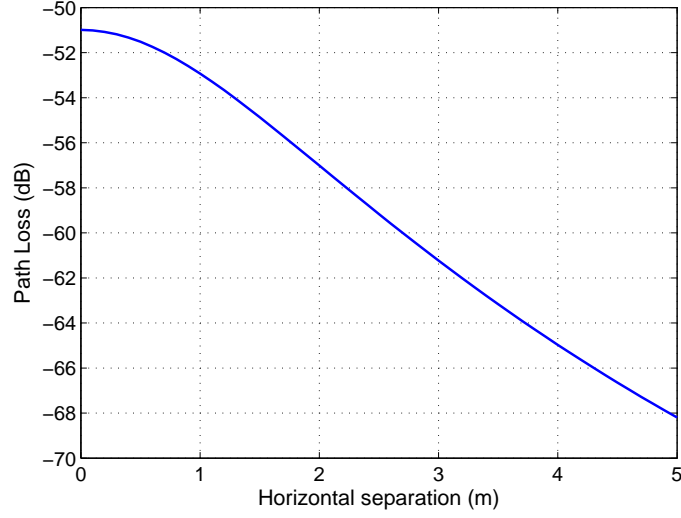
Figure 4.6: Path loss variation with horizontal separation increase between Tx and Rx.

system chip rates. This can be explained as follows. Under our system configuration, the intercell interference is dominant over the noise term in determining the system performance. As can be observed from eqs. (4.13) and (4.16)-(4.18), both the signal component and the intercell interference term at the correlation output are linearly proportional to the chip time T_c. The signal component varies proportionally with the intercell interference as the chip rate varies and thus its effect is counteracted.

4.4.2 Effect of the adjacent LED lamp distance

It is learned from the previous part that under the typical office lighting scenario the covering cell area of each LED lamp overlaps largely. To mitigate the overlap, one way is to increase the adjacent LED lamp distance a. However, this may result in the degradation of the illumination quality. To evaluate the illumination performance, two parameters are adopted, the average and the standard deviation of the illuminance at the horizontal plane of the receiver height. Dense sampling points of the illumi-
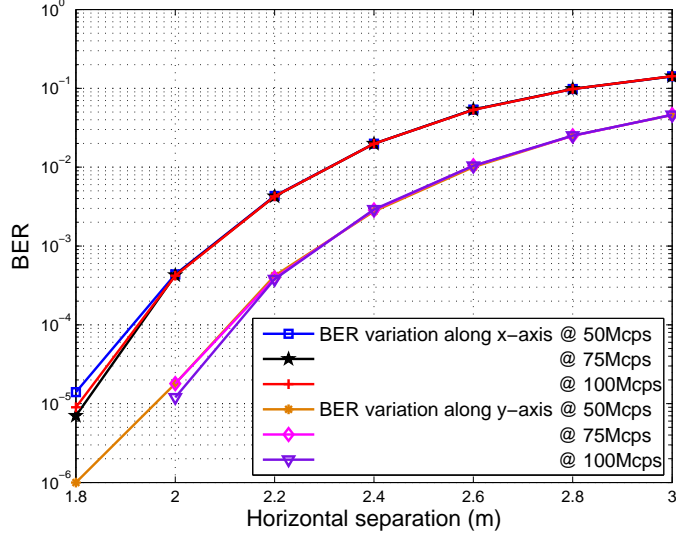
Figure 4.7: Average BER variation with horizontal separation increase.

nance are taken within the major illuminated area, based on which the average and the standard deviation are obtained. The average illuminance reflects the brightness of the illuminated plane, while the standard deviation describes its uniformity. On the basis of fixed average illuminance, the effect of adjacent LED lamp distance on the standard deviation is investigated. With the increase of the adjacent LED lamp distance, the output lumen of each LED has to increase accordingly to guarantee the fixed average illuminance. Based on our current setting, the average illuminance is 442 lx and the standard deviation is 7.6 lx. Maintaining the same average illuminance level, the standard deviation variation with adjacent LED lamp distance increase is shown in Fig. 4.8. It is observed the standard deviation increases dramatically with the adjacent LED lamp distance increase, indicating a severe degradation of the illuminance uniformity.

Another way to mitigate the cell overlapping is to select only a subset of all the LED lamps for data transmission. As shown in Fig. 4.3, instead of choosing the 6 nearest LED lamps with distance a for different wavelength channel assignment, one can
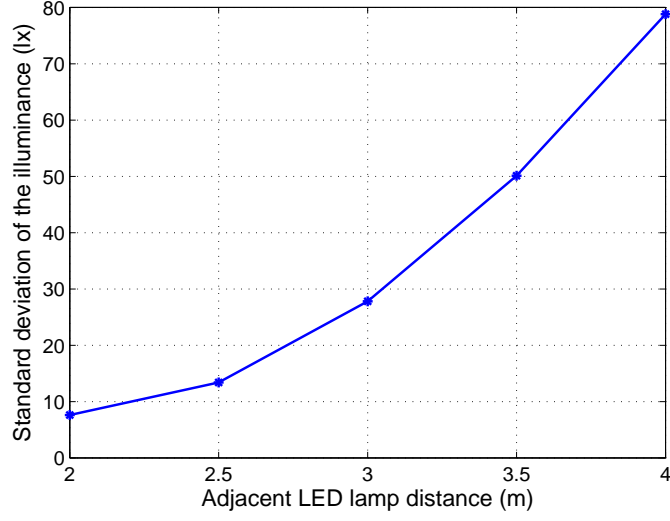
Figure 4.8: Standard deviation of the illuminance variation with adjacent LED lamp distance increase.

choose those 6 LED lamps with distance $2a$. Compared with the cochannel interference, the interference introduced by the basic lighting could be made insignificantly small. Thus the cells can be designed to have minimum overlapping without degrading the communication performance.

4.4.3   Effect of the number of users within a cell

When more than one user reside within a cell at the same time, the available transmit power needs to be allocated among different users. The transmit balancing scheme is adopted where the available power is allocated equally among the users. Thus as the number of users within a cell increases, the allocated transmit power for each user decreases, leading to the performance degradation for each user. To reveal the performance degradation of a single link with the number of user increase within the target cell, BER variations of the target user with horizontal separation change given different number of users present in the cell are simulated (Fig. 4.9). The chip rate is
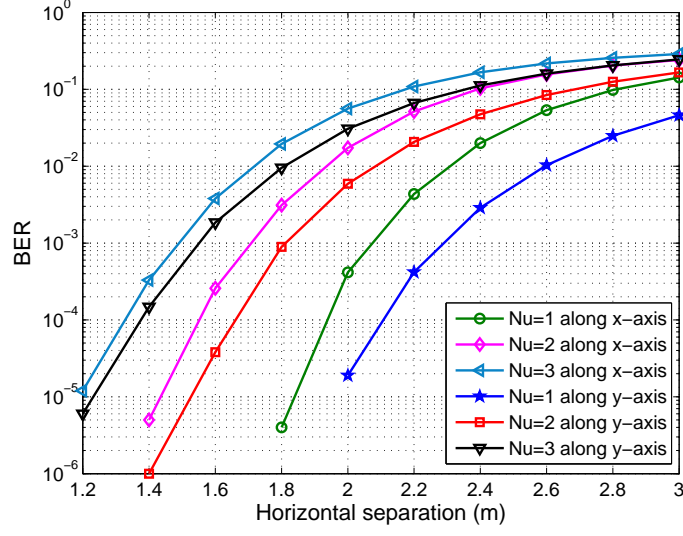
Figure 4.9: Performance degradation due to the number of users increase within a cell.

set to be 100 Mcps and the other parameters are set to be the same as those listed in

Tab. 4.1.

4.4.4 Effect of the dimming level change

In the previous two parts, we have assumed the dimming level of the target LED is 0.5, implying a VPPM symbol pulse width of $0.5T_c$ according to our definition in Section 4.3. Based on eqs. (4.13) and (4.21), the signal to noise ratio SNR could be represented as:

$$SNR = \frac{Z_u^2}{\sigma_{Z_n}^2} = \frac{N(\alpha_1 \varepsilon_1 P_1)^2 q_0^{(1)} \left(1 - R_0^{(1)}(\delta_1)\right)}{2N_0} \tag{4.23}$$

For a rectangular transmitted pulse, if we define $q_0^{(1)} \left(1 - R_0^{(1)}(\delta_1)\right)$ as the effective pulse width w_{eff}, the SNR is linearly proportional to w_{eff}. It can be derived that

$$w_{eff} = \begin{cases} w_l, & 0 < w_l \leq 0.5T_c \\ \\ T_c - w_l, & 0.5T_c < w_l < T_c \end{cases}$$, which is symmetric against $w_l = 0.5T_c$. Besides,
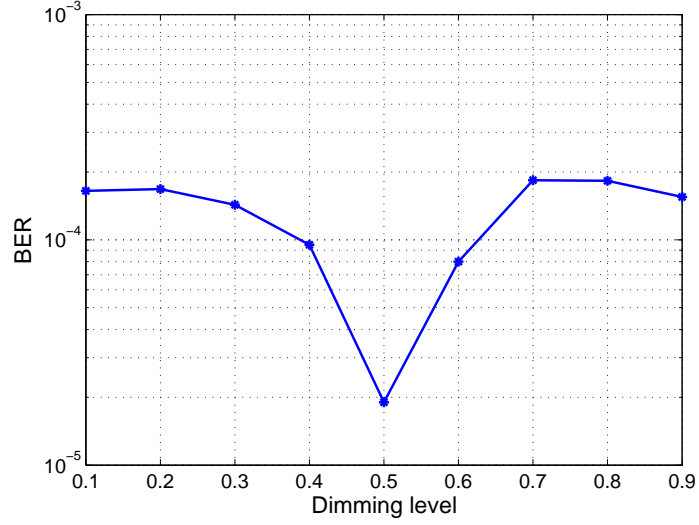
Figure 4.10: Impact of dimming level on the system performance.

according to eq. (4.16), the pulse width variation also affects the intercell interference. This makes the signal to interference plus noise ratio (SINR) at the receiver highly dependent on the pulse width. Thus the dimming level of the target LED, equivalent to the pulse width of the VPPM symbol, has a great impact on the system performance.

The effect of the dimming level change is simulated with the results shown in Fig. 4.10. During this simulation, the receiver position is fixed at $(0, 2)$ and the dimming level of the target LED varies from 0.1 to 0.9, equivalent to the pulse width change from $0.9T_c$ to $0.1T_c$, while the dimming levels of the other LEDs are determined randomly. It can be observed from this figure that the BER variation with the dimming level change has a quasi-symmetrical pattern against the axis $D_1 = 0.5$. This is mainly determined by the SNR variation pattern as discussed in the previous paragraph and the imperfection of the symmetry is mainly introduced by the simulation error.

Chapter 5

LED Traffic Light based Outdoor VLC Link Characterization

In this chapter, the application of VLC in an outdoor open space scenario based on the LED traffic light is investigated. Compared with the indoor VLC systems that have been discussed in the previous chapters, the outdoor VLC systems have several distinctions in their physical layer characteristics. The first is that large ambient light interference exists, including the background solar radiation and the artificial light interference. Their major characteristics and effects on the system performance need to be identified. The second is that the transmission relies only on the unobstructed LOS link due to absence of fixed reflecting surfaces.

Following its first proposal in 2001 [35], much research effort has been devoted to applying VLC for outdoor information transmission required in the ITS. Outdoor VLC mainly utilizes traffic related infrastructure to broadcast traffic or location information to automobiles, such as traffic lights, street lights, and automobile headlights or taillights [35, 36, 37, 40, 41]. They can also help to realize ranging [81] and information

exchange between automobiles [82].

For outdoor VLC systems, two different kinds of receiving devices can be adopted, namely the photodiode and the CMOS image sensor. Some advantages of an image sensor receiving system, compared to a photodiode receiving system, are parallel reception and robustness against interfering light sources. VLC based on a receiving CMOS image sensor has been discussed in [40, 41]; however, the relatively low sampling rate of scanned image sensor outputs and high price limit their VLC applications. On the other hand, a non-scanned array of photodiodes can support higher data rates at lower cost, and is regarded as an economic device for VLC.

The general structure of an outdoor photodiode-receiving VLC system is shown in Fig. 5.1. Up to now, most research work for such systems has mainly focused on system design and performance simulation according to a simplified ideal link model [35, 36, 37] or practical system demonstration using a specifically designed receiver tracking front-end [43]. No systematic empirical link characterization based on the COTS LED traffic lights has been carried out, including the transmitter characterization, channel modeling and validation, and background interference characterization. In this chapter, we will conduct a thorough link characterization for outdoor VLC systems with a COTS LED traffic light at the transmitter side and a photodiode as the receiver front end [83]. The obtained results obtained will provide valuable guidance for practical system design.

This chapter is organized as follows. In Section 5.1, the ambient light interference is characterized and corresponding measurement results are presented, including both the background solar radiation and commonly encountered artificial light interference. Detailed characterization of the performance of some typical COTS LED traffic lights as VLC transmitters is shown in Section 5.2. Both the frequency response and

the typical input-output relation of these traffic lights are demonstrated. Then a link budget model for the LOS VLC channel between a LED traffic light and an automobile is proposed and validated by measurements in Section 5.3. Qualitative empirical link test in a fog environment is also introduced in this section. According to those results, performance of an outdoor VLC system adopting different modulation schemes is predicted in Section 5.4.

5.1 Ambient Interference Characterization

This section focuses on the communication link ambient interference, injected with the signal, into the photodiode as shown in Fig. 5.1. This ambient interference mainly stems from two different kinds of sources: the background solar radiation and the artificial light sources. Their major characteristics and impact on the communication system will be studied.
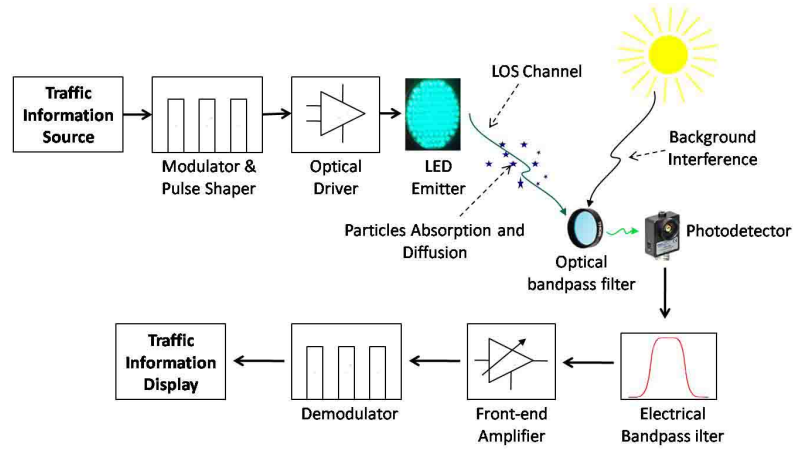
Figure 5.1: Diagram of an outdoor VLC system.

5.1.1 Background solar radiation characterization

For outdoor VLC systems, one important challenge comes from the intense background solar radiation. Photodetectors directly exposed to sunlight may easily get saturated, leading to the inability of detecting the intensity modulated optical signals. Even in the absence of the saturation problem, the shot noise in the photodetector induced by the received solar radiation can potentially be a dominating noise source that limits the performance of the whole communication system. Therefore characterization of the background solar radiation is of great importance in designing corresponding noise suppression techniques and boosting the system performance.

The background solar radiation is composed of two parts, the direct normal and diffuse horizontal spectral solar radiation. Various models have been proposed [84] predicting the background solar radiation based on a set of parameters, such as location, date, time, receiver plane configuration, and weather conditions. Under cloudless sky conditions, the direct irradiance on a surface normal to the direction of the sun at ground level for wavelength λ is given by

$$I_{d\lambda} = H_{o\lambda} D T_{r\lambda} T_{a\lambda} T_{w\lambda} T_{o\lambda} T_{u\lambda}, \tag{5.1}$$

where the parameter $H_{o\lambda}$ is the extraterrestrial irradiance at the mean earth-sun distance for wavelength λ; D is the correction factor for the earth-sun distance; $T_{r\lambda}$, $T_{a\lambda}$, $T_{w\lambda}$, $T_{o\lambda}$, and $T_{u\lambda}$ are the transmittance functions of the atmosphere at wavelength λ for molecular (Rayleigh) scattering, aerosol attenuation, water vapor absorption, ozone absorption, and uniformly mixed gas absorption respectively. The direct irradiance on a horizontal surface is obtained by multiplying the above equation by $cosZ$, where Z is the solar zenith angle. On the other hand, the diffuse irradiance is difficult to determine accurately with a simple parameterization method. It is affected largely by the surroundings, which

vary a lot with the environment change and the orientation of the receiving device. Thus no simple formula is available. For practical optical receivers, the received background solar radiation is also affected by the receiver field of view (FOV). If the sun is within the receiver FOV, usually the direct normal irradiance will dominate over the diffuse horizontal irradiance, and the received optical power won't vary a lot with the FOV. However, if the sun is outside the receiver FOV, then only diffuse horizontal irradiance should be taken into account and the received optical power is proportional to the receiver FOV since the diffuse irradiance impinges the receiver from all directions.

The measurement campaign has been conducted to empirically determine the background solar radiation level. Since we are only interested in three color bands (500nm, 590nm, 620nm) corresponding to those of the traffic lights, three different optical bandpass filters, with bandwidth of 40nm, 10nm, and 20nm respectively, were adopted for optical power measurement in these separating bands. The obtained measurement results will be normalized with the bandwidth of each separating band, which eliminates the effect of the bandwidth difference. A photodiode (918D-UV-OD3) connected to a power meter (Newport 1918C) was used to receive the background solar radiation and read out the power value. The receiver front-end combining the optical filter and the photodiode has an active receiving area of $1cm^2$ and a half angle FOV of about 15^0, mainly limited by the FOV of the optical bandpass filter. We measured the direct normal irradiance and horizontal diffuse irradiance separately. First we set the photodiode to point straight upward to collect the diffused solar irradiance from the atmosphere. Since the zenith angle of the sun was larger than the receiver half angle FOV in our setting, no direct irradiance from the sun was received. The power meter was controlled to read and record this optical power every second and this lasted almost the whole daytime to obtain the optical power variation. We will indicate this optical

power under vertical pointing as the vertical power in the remaining of this chapter. Every other hour, we also readjusted the orientation of the photodiode as the sun moved, making it point directly at the sun to collect the direct and part of the diffuse irradiance within the receiver FOV. This power was then recorded and indicated as the maximum power. As we mentioned earlier, the direct irradiance in this case is much larger than the diffused counterpart and the measured power is mainly contributed by the direct irradiance.

The power measurement in three optical bands took place in Riverside, California, USA on three days. The weather conditions were slightly different on those three days. It was a little cloudy on one day while sunny on the other two days. Our measured vertical power variation within a day is shown in Fig. 5.2, and the measured maximum power results are revealed in Fig. 5.3. Suppose the optical power spectrum density within each optical band is constant. All the results were normalized with the bandwidth and the transmittance of the optical bandpass filters.
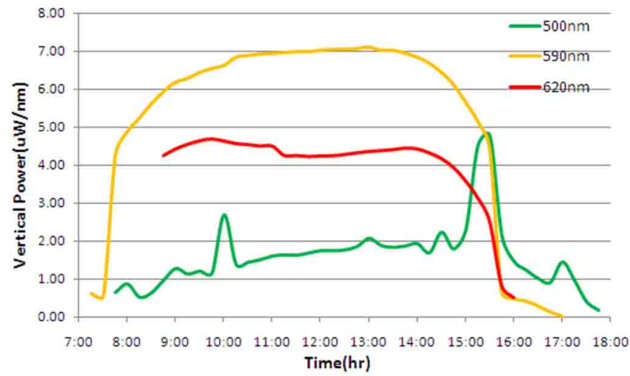
Figure 5.2: Vertical power variation within one day.

We notice that large variations occur for the vertical power measurement results of 500nm band. This is mainly due to the irregular movements of clouds that blocked

101
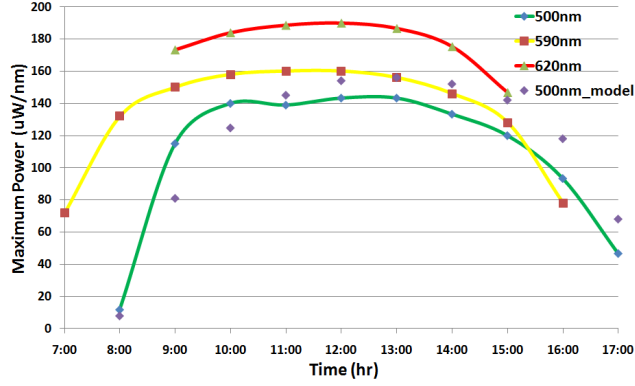
Figure 5.3: Measured maximum power variation within one day and comparison with the SPCTRAL2 model for the 500nm band.

the sun and enhanced the diffusion at the same time. Large spikes appear when the sun is blocked by the cloud. The variation is largely dependent on the climate conditions and therefore is hard to estimate. Thus the horizontal diffuse part is closely related to the weather conditions, which might be difficult to characterize using a simple model. Additionally, the diffuse irradiance is also affected largely by the surroundings. When the photodiode was adjusted to point at different objects, such as the shadow of a tree or a building exposed to sunshine, variations of the received optical power was shown to be tens of microwatt to hundreds of microwatt. Since differences exist at FOVs of three bandpass filters and the weather conditions on three days, the trend of the optical power spectrum density (W/nm) in three different bands may not exactly follow that of the solar radiation optical spectrum.

The background solar irradiance model SPCTRAL2 proposed in [84] was applied to compare against the measurement results at 500nm band (Fig. 5.3). Given some weather related parameters, such as aerosol optical depth, ground albedo, thickness of ozone, and total precipitable water vapor, combined with some other location related parameters, both direct normal irradiance and horizontal diffuse irradiance could be predicted. Acceptable agreement is mostly observed between the experimental and

102

predicted results.

Since the background solar radiation is much larger than the anticipated signal optical power (usually in the range of several microwatt), one way to isolate the signal from the intense background solar noise is by distinguishing them in the electrical frequency domain. The measured electrical power spectrum of the solar radiation on a sunny day showed clearly that the photodetected solar radiation represents mostly a DC component (less than 200Hz), which could easily be eliminated using an electrical bandpass filter. However, as we mentioned earlier, the shot noise in the photodetector induced by the intense solar radiation approximates an additive white Gaussian noise (AWGN) and couldn't be easily mitigated.

5.1.2 Artificial light source interference characterization

Another kind of interference that could impair the correct reception of the optical signal is the light from some artificial light sources. The artificial light source interference is inevitable in urban area where numerous street lights and advertising boards using different light sources (e.g. fluorescent lamp, neon lamp, LED) are in the vicinity of the traffic lights. Different from the background solar radiation, the output light from these artificial light sources is usually modulated, with an electrical power spectrum extending to a certain high frequency, potentially interfering with the signal of interest. Since there's no general model for such interference, the best way to eliminate its effect on the signal demodulation is to separate the signal and interference in the modulation frequency band. Artificial lighting interference for indoor optical wireless communications, mainly from fluorescent lamps with or without electronic ballasts, has been measured and characterized [55, 56]. However, artificial light interference for outdoor optical wireless communication systems comes from more diverse sources, the

electrical power spectra of which will be measured systematically here.

The measurement system front-end was composed of a photodiode (DET36A) with a convex lens in front and a transimpedance preamplifier (SR570), the output of which was AC coupled to a spectrum analyzer (HP 3589A) with a measurement range from 10Hz to 150MHz. The bandwidth of the measurement system was limited by that of the preamplifier, which has a flat frequency response from DC to 1MHz. We have walked through downtown Riverside and Los Angeles, and carried out measurements on different typical light sources along the street. Based on the observation, the interfering artificial light sources fall into three major categories. The first category refers to light sources for lighting purposes (e.g., street light, decoration light, background light for advertising boards) which include fluorescent lamp, incandescent lamp, xenon lamp, and LED lamp. The second category stands for light sources for static advertising purposes (e.g., neon sign board) which include neon light. And the third represents light sources for dynamic advertising and signaling (e.g., LED screen). These three categories of light sources exhibit quite different electrical power spectra. Those light sources for lighting purposes are usually driven directly by the main 60Hz AC voltage and therefore their spectra mainly contain peaks at multiple harmonics of 60Hz, extending only to several kHz and representing essentially low-frequency interference. The lights in the second category are usually driven by electronic ballast which could extend the spectrum to tens of kHz. The lights in the last category for dynamic advertising are usually driven by sophisticated controlling circuits for information display. Therefore they could produce electrical power spectra with much higher frequency components extending to hundreds of kHz, constituting a major interference for low data rate communication.

Three typical scenarios corresponding to those three categories and the measured spectra are shown in Fig. 5.4. The main peaks of 60Hz and 120Hz can be

clearly observed with their harmonics extending to less than 3kHz. The electronic ballast driven neon sign board exhibited an electrical power spectrum extending to almost 40kHz, while an extended interfering spectrum to 300kHz from a big video displaying LED screen was detected. Notice that the observable power spectrum is limited by the received light optical power and the sensitivity of our customized signal detection frontend. The received light optical power was at the range of tens of microwatt, varying a lot with the relative location and orientation between the light source and the receiver. The major noise source at the receiver front-end was from the adopted preamplifier (SR570c with a typical noise density of $10^{-24}A^2/Hz$). A lower-noise preamplifier might help to further extend the observable interfering frequency range. Filtering and electrical signal modulation techniques can be used to mitigate such artificial interference [85, 86]. Its detailed discussion is beyond the scope and is therefore omitted.

5.2   LED Traffic Light Characterization

In order to perform link budget analysis, the power delivery capability of a transmitter LED traffic light lamp has to be characterized. Since a COTS LED traffic light lamp is designed for signaling purpose only, its performance as a communication transmitter is usually absent in the vendor datasheet. In this section, some key parameters critical for communication, including the input-output relation and the frequency response, will be characterized based on the measurement results of several typical LED traffic light lamps.

Three different green COTS LED traffic light lamps (TRF108 and TRF112 from LEDtronics with diameters of $200mm$ and $300mm$ respectively, NB200RC3A from LightsToGo Inc. with a diameter of $200mm$) have been selected for measurement. They
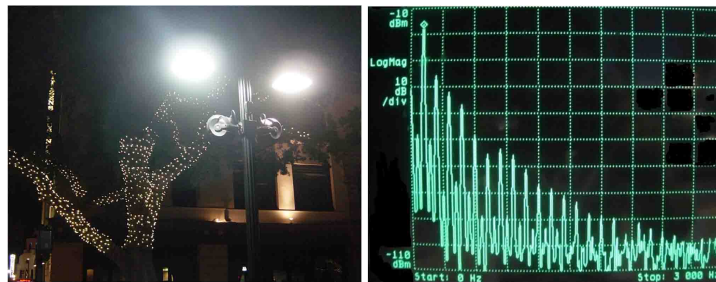
a. Typical street light scenario and its electrical power spectrum.

b. Typical neon sign board and its electrical power spectrum.
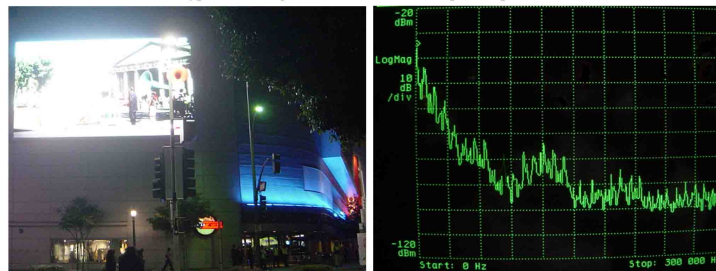
c. Typical big video displaying LED screen and its electrical spectrum.

Figure 5.4: Typical artificial light sources and their power spectra.

have typical concatenation structures connecting multiple LEDs to form a LED array in the lamp, as shown in Fig. 5.5. In NB200RC3A lamp, 61 single LEDs and 61 resistors are divided into three serial groups, each with 20, 21, and 20 LEDs correspondingly. The concatenation structures of TRF108 and TRF112 are the same except the number of LEDs, where three LEDs are first serially connected as a subgroup and then the subgroups are connected in parallel. In both lamps, two resistors are used to replace two supposed LEDs. So there are 121 LEDs plus 2 resistors in the TRF112 lamp, and 52 LEDs plus 2 resistors in the TRF108 lamp. To reveal the effects of concatenation structures on the modulation performance, we removed the AC/DC transformers and most of the internal long connecting wires, leaving only the circuit board connecting all the LEDs. Although only three LED traffic light lamps are selected for measurement, they are typical in current COTS LED traffic light market, and therefore results obtained here can be used to reveal the characteristics of general LED traffic light lamps.
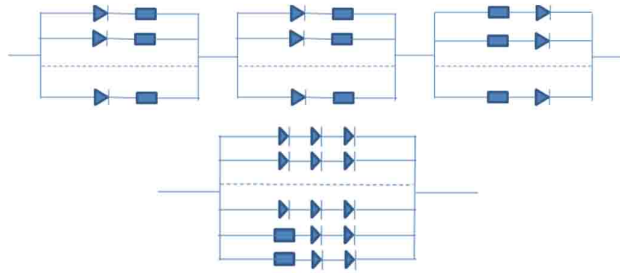
Figure 5.5: Concatenation structures of different LED lamps.

5.2.1 Input-output relation characterization

The ideal output light intensity of an LED is considered to be proportional to the injection current modeled as

$$P = \frac{I}{e} \cdot h\nu \cdot \eta_{int} \cdot \eta_{extraction}, \tag{5.2}$$

where monochromatic light frequency ν is assumed, η_{int} is the LED internal quantum efficiency, and $\eta_{extraction}$ is the light extraction efficiency. This equation is validated by our measurement results (Fig. 5.6). Given the linear relation between the injection current and the output light intensity, the relation between the input driving voltage and the output light intensity can be determined if the I-V relation of the LED traffic light lamp is available. The measured I-V curves of three COTS LED traffic light lamps are shown in Fig. 5.7. Linear and polynomial curve fitting for the LED I-V transfer function can be performed [32], and the fitting results for TRF112 are also shown in the figure. It can be observed that a third-order polynomial fits well with the measured curve for a large range of voltage, stated by

$$I = b_0 + b_1(V_{in} - V_{DC}) + b_2(V_{in} - V_{DC})^2 + b_3(V_{in} - V_{DC})^3. \tag{5.3}$$

A quasi-linear region exists for the large voltage range and can be used for data modulation (approximately 10V$\sim$12V as shown in Fig. 5.7). The nonlinear effects of the LED modulation usually lead to performance degradation if waveform modulation with a carrier is adopted, such as FSK or OFDM. If a simple baseband modulation scheme is used, such as OOK, PPM, or PAM, only discrete levels need to be differentiated and nonlinearity is of less concern.
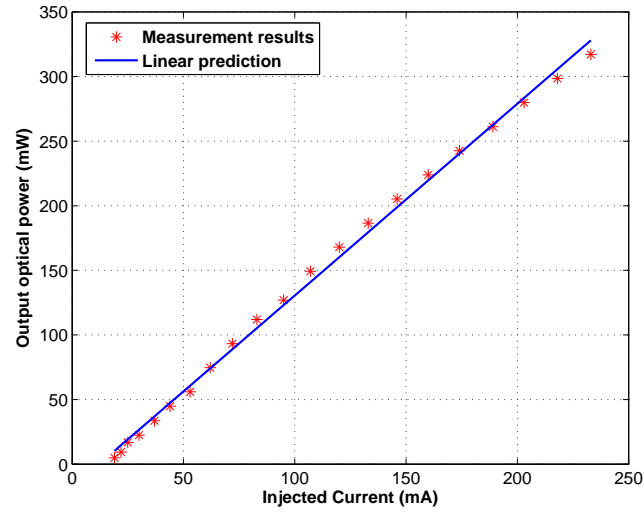
Figure 5.6: Input current and output optical power relation of TRF108.
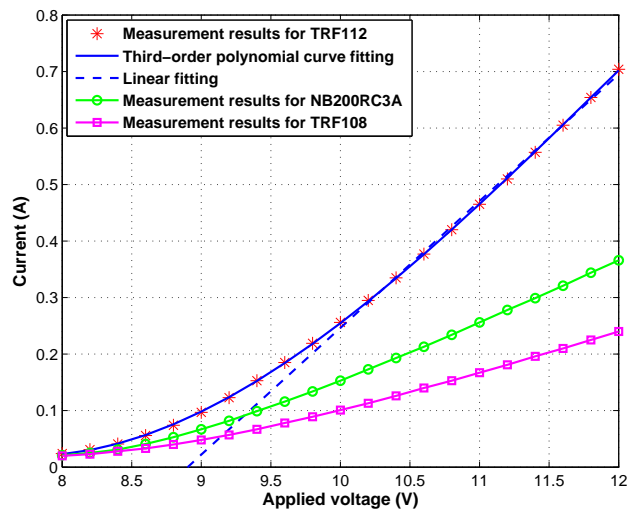
Figure 5.7: Input voltage and output current relation of typical LED traffic light lamps.

5.2.2 Frequency response characterization

Due to the intrinsic photon generating nature in a LED through recombination of the electrons and holes [48] and the parasitic capacitance and inductance of a LED traffic light lamp, emitted light typically undergoes a transition period in time upon being driven by an input current, or equivalently shows certain finite electrical bandwidth. This property may impose limitation to input signaling rate. In order to characterize the frequency response of typical COTS LED traffic light lamps, the measurement campaign was first carried out to obtain the empirical results for both single LEDs and LED lamps. The frequency-sweeping method was adopted with the experimental setup shown in Fig. 5.8. A function generator (Agilent 33250A) was adopted to provide the sweeping frequency signal (ideal sine wave). The DC bias was provided by a power supply (Agilent E3648A) and was set to make the LED operate in the quasi-linear input-output region (10V∼12V) as shown in Fig. 5.7. At the receiver front end, a photodiode (PDA10A) was adopted to receive the signal light, converting it into electrical current which was amplified thereafter by the internal amplifier. The electrical signal was then directed to the electrical spectrum analyzer and the power peak at the sweeping frequency was recorded. The photodiode we adopted has a small-signal bandwidth of 150MHz, much larger than the LED modulation bandwidth. Therefore its effect on the measured frequency response of the LED lamp is negligible.
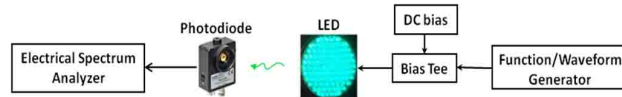
Figure 5.8: Experimental setup for the frequency response measurement.

Using this measurement system setup, the frequency response results of differ-

ent kinds of single LEDs and LED lamps were obtained in Fig. 5.9. Since the passband of the bias tee starts from 100kHz, the lower end frequency in our measurement was also set as 100kHz. Power values at all other higher frequencies were compared with that at 100kHz and the relative magnitude values were obtained. We can observe from the figure that two single LEDs from two different LED lamps have quite different modulation bandwidths (defined as the 3-dB bandwidth), one about 3MHz (TRF108) and the other about 6MHz (NB200RC3A). This could be induced by the differences in the LED core area and internal diffusion capacitance. Also only small variations between the frequency response of the single LED and that of its corresponding LED lamp are observed, which indicate that concatenation of LEDs does not affect its frequency response significantly.
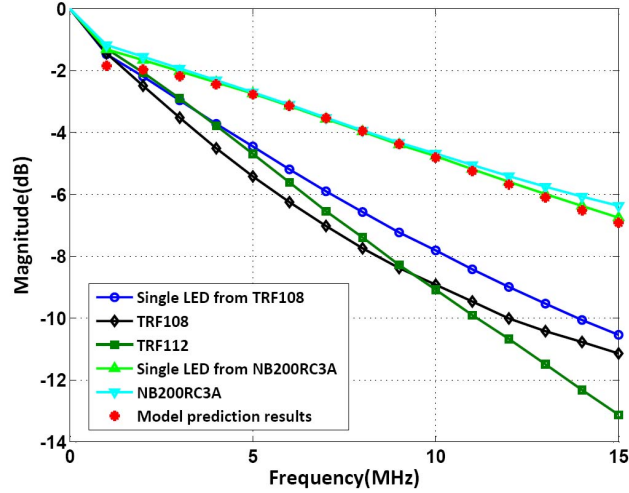
Figure 5.9: Frequency responses of different LEDs and LED lamps and comparison with the model prediction.

A simple model can be adopted to predict the frequency response of these LEDs. If the voltage is modulated at an angular frequency ω, the intensity of the light output varies with ω as [87]

$$P(\omega) = \frac{P(0)}{\sqrt{1 + (\omega\tau_{eff})^2}},$$

(5.4)

which is identical to the magnitude of the transfer function for the capacitor in an RC serial circuit whose time constant is the effective carrier lifetime $\tau_{eff} = RC$, and C can be regarded as the diffusion capacitance of the LED. The measured frequency response of the single LED from NB200RC3A was chosen to validate the model and shows satisfactory agreement according to this figure. Pre-equalization techniques to trade electrical power for a larger LED bandwidth have been proposed [19, 20].

5.3 Link Analysis and Validation

Following the characterization of the power transmitting capability of the transmitter LED traffic light, the link loss is analyzed and validated in this section. A path loss model and models for typical noise sources in the transceiver front end are first introduced. Then carrier to noise density ratio (C/N_0) measurement results will be shown to validate analysis.

5.3.1 Theoretical link models

For most lighting lamps where the transmission beam pattern is symmetric around the normal of the transmitter LED lamp, a simple line-of-sight (LOS) path loss model can be adopted [61]

$$L_L = \frac{g_s(\beta)A_r\cos(\alpha)}{D^2\int_0^{\theta_{max}}2\pi g_s(\theta)\sin(\theta)d\theta}. \tag{5.5}$$

However, in most COTS LED traffic light lamps, associated beam shaping lens usually alter the symmetric transmission beam pattern to make the signaling more efficient and less dazzling. If we define the normal of the transmitter plane as the z-axis, the horizontal direction perpendicular to the z-axis as the x-axis, and the vertical direction perpendicular to the z-axis as the y-axis, we can adopt those two angle parameters in

a typical spherical coordinate system, the inclination angle θ and the azimuth angle φ. Then the transmission beam pattern can be described as $g_s(\theta, \varphi)$ adopting two parameters instead of a single parameter function $g_s(\theta)$. The path loss model should be revised as

$$L_L = \frac{g_s(\beta, \gamma) A_r \cos(\alpha)}{D^2 \int_0^{2\pi} \int_0^{\pi} g_s(\theta, \varphi) \sin(\theta) d\theta d\varphi}, \tag{5.6}$$

where β and γ are the inclination angle and the azimuth angle of the receiver position respectively, A_r is the receiver active area, α is the angle between the transmitter-receiver line and the receiver normal, and D is the receiver distance to the transmitter.

Under clear weather conditions, the received optical power at the receiver can be written as $P_r = P_t L_L$, where P_t is the total transmitted optical power at the transmitter LED lamp. In other severe weather conditions, such as fog, rain, and snow, extra attenuation of the optical power is introduced, $P_r = P_t L_L L_A$, where L_A is the attenuation by particle absorption and diffraction. Besides extra attenuation of optical power in severe weathers, fading of the transmission channel may be introduced by the motion of some particles. Such phenomena have been investigated and reported in rainy, fogging or snowy weather [88, 89, 90].

In order to obtain the signal to noise ratio (SNR) at the receiver front-end, typical noise sources in the outdoor VLC system should be characterized. Among all possible noise sources in a free space optical wireless communication system, including ambient light interference, quantum shot noise, optical excess noise, photodetector dark current noise, photodetector excess noise, and electronics noise, the most significant noise sources comprise the artificial light source interference, background solar radiation induced shot noise and the electronics noise.

The artificial light source interference has been characterized empirically through

experimental measurement. The quantum shot noise arises from the stochastic detection nature of the photodetector. It is proportional to the average total detected photocurrent with single-sided PSD as

$$\sigma_{shot}^2 = 2qI, \tag{5.7}$$

where q is the electron charge and I is the total photocurrent. The electronics noise mainly represents noise of the preamplifier at the receiver front-end, represented by $\sigma_{amp}^2(f)$. For most COTS preamplifiers, the noise PSD is usually included in the vendor's datasheet. For a customized communication system where the preamplifier noise is fixed, the dominating noise source depends on the application scenario, in which the artificial light source interference and background solar radiation level vary, leading to the variation of the shot noise level. A comparison of the shot noise and preamplifier noise is shown in Fig. 5.10 for three photodiodes at different background solar radiation levels. In this figure, the preamplifier noise was taken from the datasheet of a commercial preamplifier as $2pA/\sqrt{Hz}$ and three photodiodes have different active receiving areas of $0.8mm^2$, $13mm^2$, and $1cm^2$.
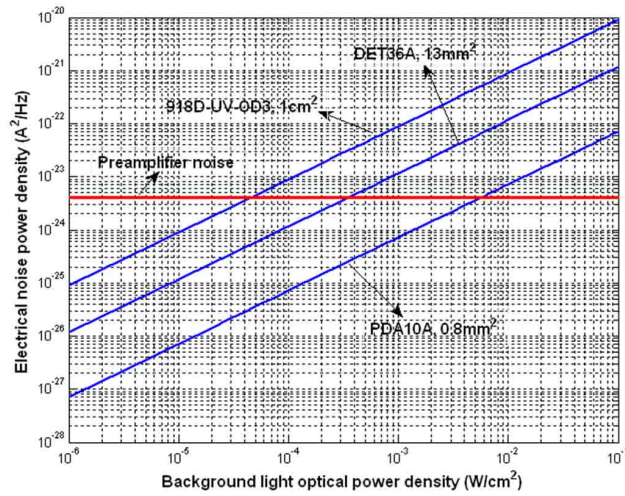
Figure 5.10: Comparison of shot noise and preamplifier noise.

The above analysis is validated indirectly by measured carrier to noise density ratio (C/N_0). If a driving voltage signal $V = V_0 + V_a sin(2\pi f_0 t + \phi)$ is applied to the LED traffic light lamp, where V_0 and V_a are set to make the traffic light lamp operate in the quasi-linear input-output region, the total output optical power follows the same relation, $P_t = P_0 + P_a sin(2\pi f_0 t + \phi)$. After propagation through a LOS channel with attenuation L and reception by a photodiode with responsivity R_λ (A/W), the C/N_0 can be represented as

$$\frac{C}{N_0} = \frac{\frac{1}{2}(R_\lambda L P_a)^2}{\sigma_{shot}^2 + \sigma_{amp}^2},$$

(5.8)

where σ_{shot}^2 and σ_{amp}^2 are the PSD of the shot noise and amplifier noise respectively. For our link validation measurement, the test site is chosen so that no artificial light source is present and thus its effect is omitted here.

5.3.2 Empirical link measurement

The outdoor empirical link measurement campaign was carried out on a sunny day. The experimental system was set up to include the sun within the receiver FOV, which represents the worst case for outdoor VLC where the background solar radiation interference reaches a peak. A simple DC-suppressing signal detection front-end was integrated to realize maximum signal amplification. At night, the same testing was carried out for comparison utilizing two different signal detection front-ends, the DC-suppressing front-end and another transimpedance preamplifier front-end with higher gain and lower noise but without DC-suppressing capability.

5.3.2.1 Experimental setup

The experimental setup with DC-suppressing signal detection is shown in Fig. 5.11. At the transmitter, a $500 kHz$ sinusoidal signal from a function/waveform generator

(Agilent 33250A) combined with a DC bias (Agilent E3648A) was used to drive the green LED lamp (TRF108) to work in the quasi-linear region. As can be observed from Fig. 5.9, the power loss due to the frequency response of the LED lamp is quite insignificant. The output optical signal then underwent the LOS channel with attenuation and reached the receiver. At the receiver, an optical bandpass filter (Thorlabs FB500-40) was adopted to reject the out-of-band optical power, reducing the total received solar radiation power. Then a convex lens was used to help collect more optical signal power, providing a gain for optical reception. The collected optical signal with background solar radiation entered the photodiode (Thorlabs DET36A) and was converted to an electrical current signal, which was output to a resistor and transformed to a voltage signal. This voltage signal was then filtered by a bandpass filter (TTE KB4-500K-50K-50-69B) to eliminate the DC component induced mainly by the background solar radiation. This filtered signal was amplified (Sonoma Instrument 310) and output to the spectrum analyzer (HP 3589A) for C/N_0 measurement. For the experimental setup at night without strong DC component interference by solar radiation, another receiving front-end, composed of the photodiode (DET36A) and a transimpedance preamplifier (SR570) to directly amplify the current signal from the photodiode, was also adopted for comparison.

During the experimental system setup, the traffic light lamp was mounted on a basketball hoop with a height of $3.1m$ and the photodetector was attached to a moveable platform with a height of $1.1m$, approximately the same as that of the front hood of an automobile. During the measurement the photodetector was set to be along the normal of the traffic light lamp and its active receiving area was adjusted to point directly at the traffic light lamp, which guaranteed maximum signal power reception. The horizontal distance between the transmitter and receiver varied from $5m$ to $80m$ and
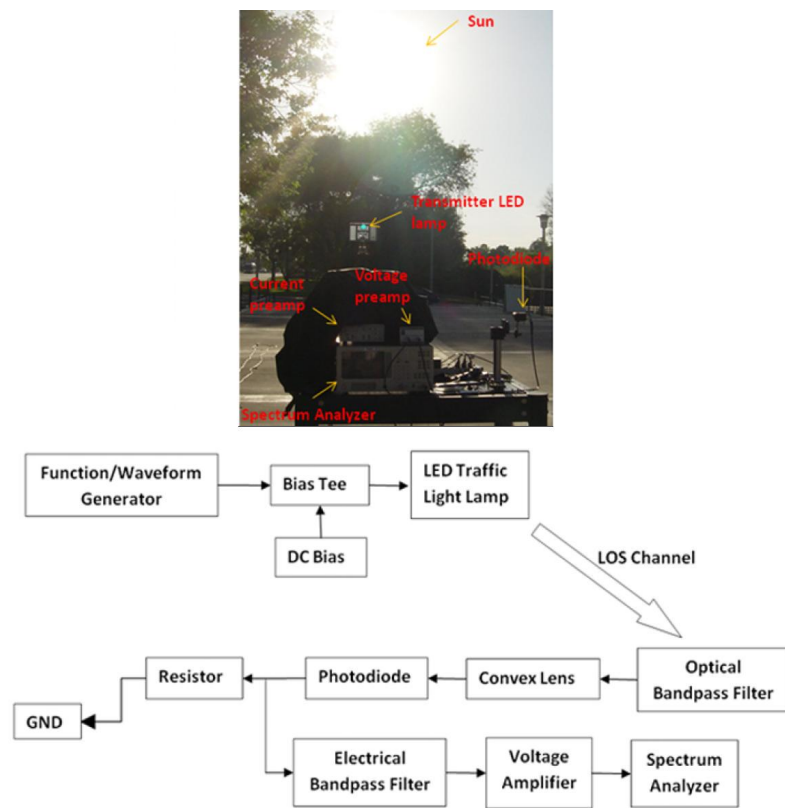
Figure 5.11: Experimental setup for outdoor C/N_0 measurement.

Table 5.1: Parameters in the measurement system

Applied bias voltage	$10.5V$
Signal voltage amplitude	$1.5V$
Modulation frequency	$500kHz$
Transmitted optical power at bias	$186mW$
Transmitted AC signal optical power	$136.2mW$
Horizontal distance	$5 \sim 80m$
Transmitter lamp height	$3.1m$
Receiver photodetector height	$1.1m$
Photodiode effective receiving area	$13mm^2$
Background solar radiation density	$1.2mW/cm^2$
Photodetector responsivity	$0.28A/W$
Convex lens diameter	$2.54cm$
Receiver FOV	15^0

the corresponding C/N_0 was recorded. All the related parameters of the experimental system are listed in Table 5.1.

5.3.2.2 Measurement results

The C/N_0 measurement results with two different signal detection front-ends at different horizontal separation distances are presented in Fig. 5.12. Because the one with DC-suppressing capability has lower amplification gain and larger noise, mainly originated from the resistor and the voltage amplifier, the C/N_0 with this signal detection front-end has an almost $20dB\text{-}Hz$ poorer performance. Also the C/N_0 results adopting

this DC-suppressing front-end are the same for measurement at both the daytime and the nighttime, which indicates the noise from the amplifier outweighed the solar radiation induced shot noise. Thus the effect of direct solar radiation input on the photodiode couldn't be observed in this case.
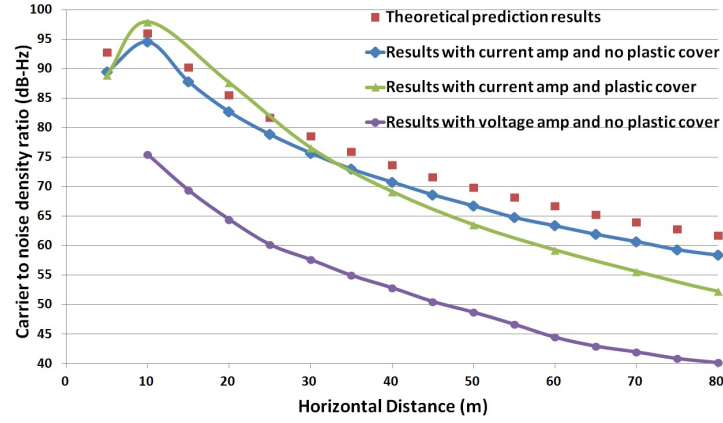
Figure 5.12: C/N_0 measurement results for different cases and comparison with the theoretical predication results.

As we mentioned earlier, the plastic lens cover is usually adopted for the LED traffic light lamp to alter the transmission beam pattern and make the signaling more efficient. Two typical plastic lens covers exist for the LED traffic light lamp, namely the Cobweb lens and the Fresnel lens. The Cobweb lens makes LED traffic lights quite bright, but not dazzling, through secondary distribution of luminous intensity; that is, the rays of light are evenly distributed such that the failure of one of the LEDs will not affect the overall performance. On the other hand, a small Fresnel lens makes LED traffic lights extremely bright resulting in high luminous intensity and visual penetrability. The LED traffic light we adopted for measurement has a Fresnel lens cover in front. The C/N_0 measurement results with the higher gain transimpedance preamplifier receiving front-end for the LED traffic light both with and without the plastic Fresnel lens cover are also compared in this figure. We can observe that despite additional losses introduced by the

plastic cover, the C/N_0 results with the cover are still larger than its counterpart within a certain distance (about 30m). This is mainly due to the beam shaping capability of the plastic lens cover which converts the axis-symmetrical radiation pattern to a downward enhancement pattern.

5.3.3 Measurement-based model validation

In this part, the theoretical link analysis is validated by our measurement results. Since the parameters of the transimpedance preamplifier are available from the datasheet and the transmission pattern of the LED traffic light lamp without the plastic lens cover is more convenient to characterize (as shown in Fig. 5.13, indicating essentially an axis-symmetric pattern), the measurement results under those two conditions were adopted as reference.
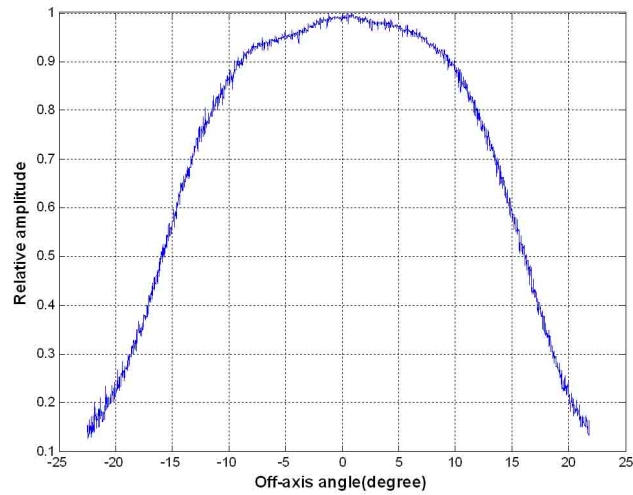

Figure 5.13: LED traffic light transmission beam pattern without plastic lens cover.

Due to the absence of DC-suppression capability to the input current signal for the transimpedance preamplifier, the validation reference measurement had to be carried out at night, when the background optical power in the corresponding green band was

only several microwatt. Therefore the dominant noise source was the preamplifier noise, which is $2pA/\sqrt{Hz}$ according to the vendor's datasheet. The C/N_0 results are then calculated based on the theoretical analysis and the listed parameters, which are also shown in Fig. 5.12. Good conformity is observed between the measurement results and the theoretical prediction. However, small deviations still exist which could be introduced by the inaccuracy of some parameter values we measured, such as the total transmitted optical power, the beam transmission pattern, and the convex lens gain.

5.3.4 Empirical fog environment testing

In this part, we compare the sensitivity of the photodiode with that of the human eye in a severe fog environment. This was designed mainly to demonstrate the advantage of the outdoor traffic light to vehicle VLC system in detecting the optical signal over the human vision in severe weather conditions like fog.

5.3.4.1 Experimental setup

The measurement campaign was carried out in an enclosed chamber. The main frame of the chamber was constructed with 1inch PVC pipeline and then transparent plastic paper was used to cover the main frame. The fog was generated using a fog machine. During the experiment the transmitter LED traffic light lamp was located at one end of the chamber. The traffic light lamp was driven by the combined 100kHz sinusoid signal from the signal generator and the DC bias from the DC supply source. At the receiver side, a photodiode was set to point directly at the transmitter LED lamp to observe the transmitted signal. The generated photocurrent was output to a transimpedance preamplifier and then it was connected to a spectrum analyzer to observe the received signal. A photo shoot showing the experimental setup is shown in

Fig. 5.14.
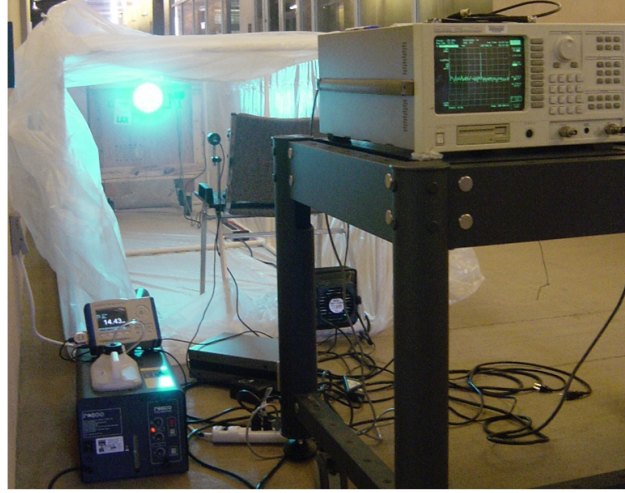
Figure 5.14: Photo shoot of the real experimental system.

5.3.4.2 Measurement results

Since the fog density inside the chamber couldn't be controlled, no quantitative results were obtained and only some qualitative phenomena were observed. At first the chamber was filled with dense fog so that our human eye couldn't see the traffic light and the photodiode couldn't detect the modulated signal either. Then the fog machine was stopped and the fog began to decay in the chamber slowly. In the meantime, we observed both the signal variation on the spectrum analyzer and the transmitter LED lamp from the receiver side. With the decay of the fog density in the chamber, the signal amplitude at 100kHz on the spectrum analyzer began to increase while our human eye couldn't see anything about the traffic light from the receiver side. As the signal amplitude reached about 20dB above the noise floor, our human eye could see a little bit of green from the receiver side, as shown in Fig. 5.15. After that, as the human eye could see that traffic light clearer and clearer, the signal amplitude also became larger and larger. These

phenomena validated the idea that the photodiode has better modulated traffic signal detection capability than our human eye in a dense fog environment.
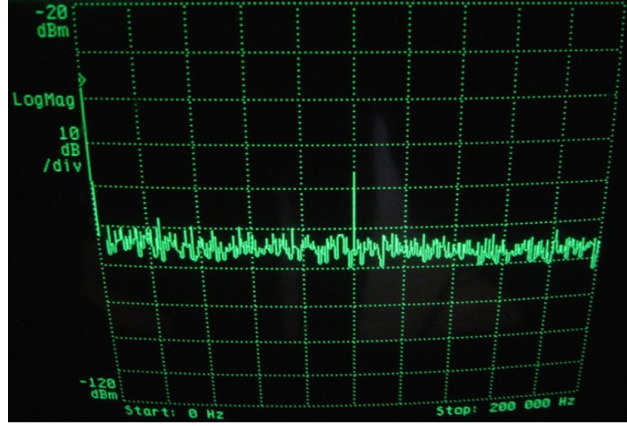
Figure 5.15: Signal amplitude on the spectrum analyzer when the human eye could see green from the traffic light.

5.4 System Performance Evaluation

In this section, the practical communication system performance will be evaluated. Since typical artificial light source interference lies in the low-frequency band (less than $1MHz$), modulation schemes that have least frequency components in the low-frequency band are preferred. Therefore here we consider the performance of pulse position modulation (PPM), which could be designed to have little or none frequency components in the low-frequency band [91]. We disregard the artificial light source interference here because of its environment-dependent nature.

The parameter values used for simulation are taken from the C/N_0 measurement system with some modifications. First, the height of the traffic light lamp is set to be the standard height of $5m$. Second, the output optical signal power is set to be the full power when the lamp is driven by the nominal driving voltage as stated in the datasheet, which was measured to be $322.2mW$. This is different from the signal power

123

adopted for link validation where only part of the full power was used due to the limita-
tion of the modulation method. To evaluate the universality of the adopted signal power
value, a corresponding standard specifying the brightness of $200mm$ traffic lights was
reviewed [92]. In this standard, the minimum luminous intensity along the lamp refer-
ence axis is set to be $200cd$. It's also required that the minimum luminous intensities
within 5^0 and 10^0 below the reference axis should be larger than 50% and 12.5% of that
along the reference axis respectively. To make use of the brightness requirement in the
standard, conversions from photometric unit to absolute power unit need to be carried
out [61]. Based on the measured spectra of three color LEDs, the conversion rate for
green, red, and yellow LED is $2.89mW/lm$, $5.08mW/lm$, and $4.52mW/lm$ respectively.
For our system setup, the spatial distribution requirement is satisfied according to Fig.
5.13. Due to the lack of a specified radiation pattern in the standard, no minimum total
transmitted optical power requirement can be derived that could be used to compare
against our adopted transmitted power value. Instead, the minimum luminous inten-
sity along the reference axis could be evaluated by the received optical power at a far
distance, where the paraxial assumption is valid. A comparison was made at the hori-
zontal distance of $80m$, the minimum received optical power required by the standard is
$2.92 \times 10^{-5}mW$ while the calculated received optical power based on our system setup
is also $2.92 \times 10^{-5}mW$, satisfying the minimum axial luminous intensity requirement.
From the above analysis, the adopted traffic light is typical under the requirement of
the standard and therefore the system performance evaluation based on this is also
representative.

For M-PPM modulation, each group of $log_2 M$ bits is encoded into an M-PPM
waveform $p_i(t)$, $i = 1, ..., M$, which has duration T. Each $p_i(t)$ includes one "chip"
of unit amplitude and duration T/M, in addition to $M - 1$ chips of zero amplitude.

A sequence of $p_i(t)$ forms the chip waveform $b(t)$, which is scaled by the peak optical power P_{peak} and transmitted over the channel $h(t)$. The receiver employs a unit-energy filter $g(t)$, which is matched to $p_1(t)$, and then samples the filtered signal at rate M/T, resulting in the signal samples

$$x_k = P_{peak}b(t) * h(t) * g(t)|_{t=kT/M} \tag{5.9}$$

The receiver chooses the largest among each group of M samples to obtain the detected symbol, which yields $log_2 M$ bits.

The electrical power spectrum of M-PPM was shown to be[91]

$$S(\omega) = |P(\omega)|^2[S_c(\omega) + S_d(\omega)], \tag{5.10}$$

where

$$S_c(\omega) = \frac{1}{T}[(1 - \frac{1}{M}) + \frac{2}{M}\sum_{k=1}^{M-1}(\frac{k}{M} - 1)cos(\frac{k\omega T}{M})], \tag{5.11}$$

$$S_d(\omega) = \frac{2\pi}{T^2}\sum_{k=-\infty}^{\infty}\delta(\omega - \frac{2\pi kM}{T}). \tag{5.12}$$

Fig. 5.16 shows the power spectrum of 2-, 4-, 8-, 16-PPM and that of OOK modulation. Compared with OOK modulation, PPM has much less frequency components in the low-frequency band.

The symbol error rate (SER) of M-PPM can be expressed as [91]

$$SER = Q(\frac{x_1 - x_2}{\sqrt{2N_0}}) + Q(\frac{x_1 - x_3}{\sqrt{2N_0}}) + ... + Q(\frac{x_1 - x_M}{\sqrt{2N_0}}), \tag{5.13}$$

where $N_0 = \sigma_{shot}^2 + \sigma_{amp}^2$. The bit error rate can be approximated as

$$BER \simeq \frac{M/2}{M-1}[Q(\frac{x_1 - x_2}{\sqrt{2N_0}}) + ... + Q(\frac{x_1 - x_M}{\sqrt{2N_0}})]. \tag{5.14}$$
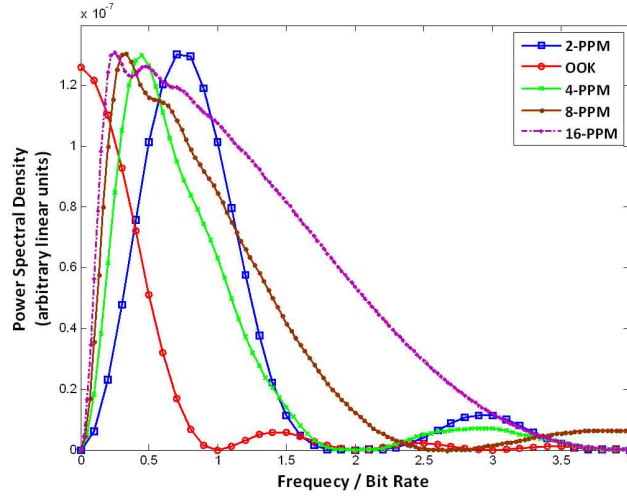
Figure 5.16: Power spectrum density of PPM and OOK.

5.4.1 Performance with horizontal separation variation

Adopting the calculated path loss results used for model validation at different horizontal separations in Section 5.3 and assuming the peak optical power P_{peak} to be fixed for different M-PPM ($M = 2, 4, 8, 16$), the received signal samples x_k can be obtained. The bit error rates of different M-PPM at a fixed symbol rate and 2-PPM at different bit rates are compared in Fig. 5.17. Here two noise sources discussed in Section 5.3, namely the preamplifier noise ($2pA/\sqrt{Hz}$) and the background solar radiation induced shot noise, are considered for system performance evaluation. The background solar radiation level is chosen to be the average horizontal diffuse density level of $2\mu W/nm$ shown in Fig. 5.2. Results show that at a bit rate of $100kbps$ and BER of 10^{-3}, the horizontal separation of $80m$ can be achieved between the transmitter and receiver, which is sufficient to deliver emergency alerts and real-time traffic information. Comparing the performance of 2-PPM and higher order PPM at the same data rates, 2-PPM has better performance at the expense of higher power consumption, which is not a key issue for outdoor VLC system. Besides, 2-PPM has much less low-frequency com-

ponents than higher order PPM as seen from Fig. 5.16, boosting the system capability against low-frequency artificial light source interference.

System performance with 2-PPM at a data rate of $100kbps$ under different background solar radiation levels is compared in Fig. 5.18. Here zero solar radiation represents the scenario at night, $140\mu W/nm$ represents the worst case where the direct normal irradiance from the sun is received, and the other two stand for cases with different dominant horizontal diffuse irradiance. The worst case shows a communication range of only $30m$ at the BER of 10^{-3} while the best case extends the range to $115m$.
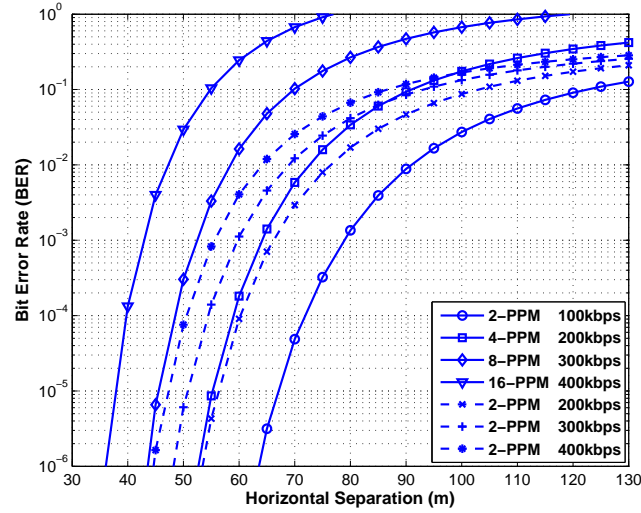
Figure 5.17: BER performance of different M-PPM and 2-PPM at different bit rates.

5.4.2 Range-rate tradeoffs

For the range-rate tradeoff analysis here, the 2-PPM modulation scheme is adopted. According to eq. (5.13), the communication system BER can be written as

$$BER = Q\left(\frac{x_1 - x_2}{\sqrt{2N_0}}\right), \tag{5.15}$$
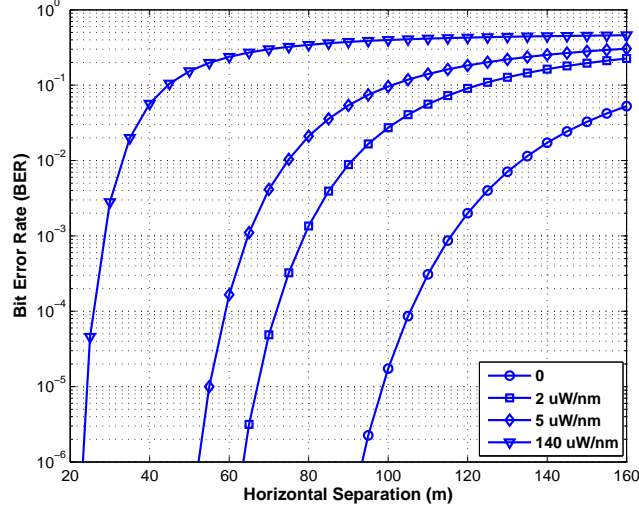
Figure 5.18: BER performance of 2-PPM at 100kbps under different background solar radiation levels.

where $x_1 = RL_L P_t T_r \sqrt{T_b}$ and $x_2 = 0$, R is the responsivity of the photodiode, L_L is the path loss of the channel, T_r is the transmittance of the optical bandpass filter, $T_b = 1/R_b$ is the bit time. If we rewrite eq. (5.5) as

$$L_L = c/D^2, \qquad c = \frac{g_s(\beta) A_r \cos \alpha}{\int_0^{\theta_{max}} 2\pi g_s(\theta) \sin \theta d\theta}, \qquad (5.16)$$

the relation between the data rate R_b and the range D can be represented as

$$D = \sqrt{\frac{RcP_t T_r}{Q^{-1}(BER)\sqrt{2N_0 R_b}}} \qquad (5.17)$$

The path loss increases with baseline range D, resulting in the SNR decrease at longer ranges. Thus the achievable data rates at different ranges are of practical interest.

The adopted preamplifier has a typical equivalent input current noise density of $\sigma_{amp}^2 = 2pA/\sqrt{Hz}$. Since the received background solar radiation usually varies with several impacting factors as partially shown in Fig. 5.2 and Fig. 5.3, we take the average horizontal diffuse density level $2.3\mu W/nm$. If we consider a green optical bandpass filter with bandwidth of 40nm and transmittance of 0.64, and the convex lens gain of 3.25, the total received solar radiation power is then 195W. The range-rate tradeoff performance

is shown in Fig. 5.19. With a BER requirement of 10^{-3}, data rate about 1Mbps could be achieved at 50m and 1kbps at 280m.
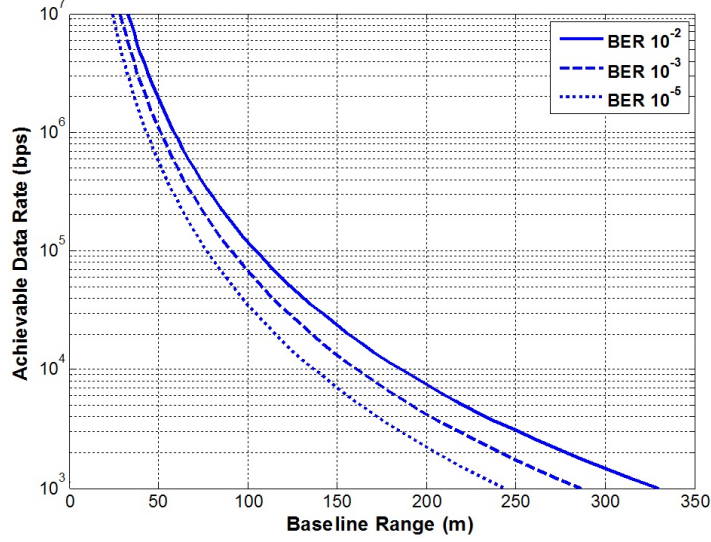
Figure 5.19: Range-rate tradeoff for application scenarios during daytime.

Fig. 5.20 demonstrates the effects of background solar radiation at 0, 2.3μW/nm, 5.4μW/nm, 140μW/nm respectively with system BER of 10^{-3}, where zero solar radiation represents the scenario at night, 140μW/nm represents the worst case where the direct normal irradiance from the sun is received, and the other two values stand for cases with dominant horizontal diffuse irradiance. The worst case gives 1kbps at 100m, and the best case extends the range to 430m.
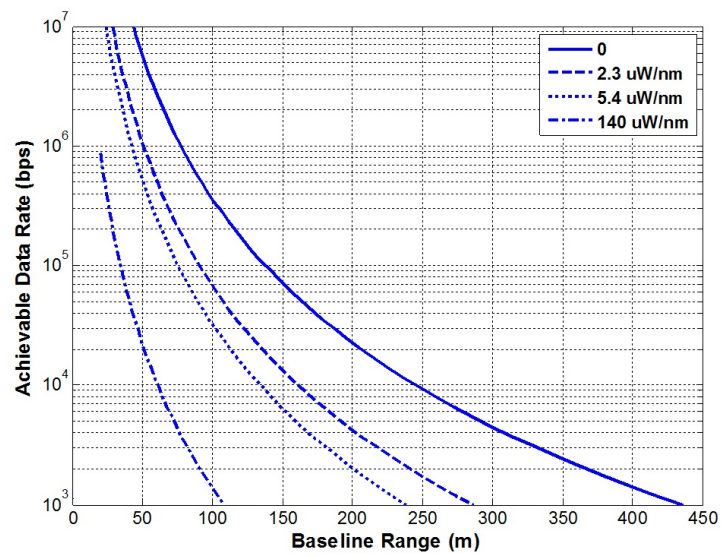
Figure 5.20: Range-rate tradeoffs with different background solar radiation levels.

Chapter 6

Conclusions

This dissertation investigated the basic physical layer characteristics of both the indoor lighting combined and outdoor LED traffic light based VLC systems, as well as corresponding transceiver design techniques to enhance the system data rate and improve the system performance.

As the basis for transceiver design, the physical layer characteristics of the indoor lighting combined VLC were first investigated systematically. The conversion from photometric parameters to radiometric parameters was introduced, providing a path between the evaluation of the illumination performance and the communication performance. The indoor VLC channels, comprised of the LOS and the NLOS channels, were investigated. A theoretical formula for the LOS path loss was derived using the commonly provided photometric parameters and then a link validation was performed based on a COTS white lighting LED. The NLOS channel impulse response was then characterized experimentally. The measured impulse response results of a typical office room and some other application scenarios were provided, together with the comparison with the computer simulation results. Next some typical noise sources present in the

VLC systems were discussed and the corresponding PSD expressions were shown. The performance of several potential uplink options for a full duplex communication system was evaluated from different aspects. Finally, a built point-to-point prototype system was reported to validate the feasibility of the VLC.

Several transceiver design techniques to boost the point-to-point communication data rate were investigated. A new pre-equalization technique using digital filters was proposed and their performance was evaluated numerically. The bandwidth efficient modulation scheme, OFDM, was then introduced. One typical issue when applying OFDM in VLC systems is the high PAPR introduced flickering problem. The probability distribution of such PAPR in VLC systems was derived, providing guidance on PAPR reduction. At last, the application of MIMO in indoor VLC systems was introduced, including both the non-imaging and imaging MIMO systems. Their corresponding capacities were evaluated and effects of different parameters affecting the channel capacities were discussed, such as the receiver antenna separation and the number of transceiver antennas.

Besides the single-user point-to-point communication link, a point to multi-point multiuser access scheme was proposed, combining the wavelength-division and code-division multiple access (WD-CDMA). Such multiuser VLC can be applied in the femtocell systems, named optical femtocell, to avoid interference issues between the femto- and macro- cell networks. To accommodate the dimming control functions required by lighting, the IEEE standard proposed VPPM modulation scheme was adopted. The system performance was first analyzed theoretically and then simulated using the computer Monte-Carlo simulation. Performance in a typically illuminated office room and effects of different parameters were revealed.

In addition to the indoor application scenarios, the outdoor VLC utilizing the

LED traffic lights and a photodiode receiver was also investigated. The systematic link characterization was carried out empirically, using COTS LED traffic lights. First, one big challenge in applying VLC outdoor, the ambient interference, including the background solar radiation and artificial light source interference, was investigated by field measurements. The transmitter performance was then evaluated using some typical COTS LED traffic lights. The LOS link validation was then carried out by measuring the carrier to noise density ratio. The empirical fog environment testing was also conducted to compare the sensitivities of the photodiode and the human eye in picking up a modulated signal. Finally, the link performance was evaluated numerically using our measurement results, including the BER variation with the horizontal separation and the range-rate tradeoffs.

Bibliography

[1] A.M. Street, P.N. Stavrinou, D.C. O'Brien, and Edwards D.J. Indoor optical wireless systems - a review. *Optical and Quantum Electronics*, 29(3):349–378, 1997.

[2] M. Kavehrad. Broadband room service by light. *Scientific American*, pages 82–87, 2007.

[3] J.M. Kahn and Barry J.R. Wireless infrared communications. *Proc. of the IEEE*, 85(2):265–298, 1997.

[4] J.G. Proakis and M. Salehi. *Digital Communications, Fifth Edition*. McGraw-Hill Hiher Education, New York, US, 2007.

[5] J.K. Kim and E.F. Schubert. Transcending the replacement paradigm of solid-state lighting. *Optics Express*, 16(26):21835–21842, 2008.

[6] G. Pang, K. Ho, T. Kwan, and E. Yang. Visible light communication for audio systems. *IEEE Transactions on Consumer Electronics*, 45(4):1112–1118, 1999.

[7] Visible light communication consortium. www.vlcc.net.

[8] IEEE WG802.15.7. IEEE standard for local and metropolitan area networks – part 15.7: Short-range wireless optical communication using visible light. 2011.

[9] T. Komine and M. Nakagawa. Fundamental analysis for visible-light communication system using led lights. *IEEE Trans. on Consum. Electron.*, 50(1):100–107, 2004.

[10] J. Grubor, S. Randel, K-D. Langer, and W. J. Walewski. Broadband information broadcasting using LED-based interior lighting. 26(24):3883–3892, 2003.

[11] G.B. Prince and T.D.C. Little. On the performance gains of cooperative transmission concepts in intensity modulated direct detection visible light communication networks. In *Proceedings of ICWMC*, pages 297–302, 2010.

[12] C.G. Lee, C.S. Park, J. Kim, and D. Kim. Experimental verification of optical wireless communication link using high-brightness illumination light-emitting diodes. *Optical Engineering*, 46(12):125005–1 – 125005–7, 2007.

[13] J. Grubor, S.C.J. Lee, K.D. Langer, T. Koonen, and J.W. Walewski. Wireless high-speed data transmission with phosphorescent white-light leds. In *Proceedings of the 33rd European Conference and Exhibition of Optical Communications*, pages 1–2, 2007.

[14] T.D.C. Little, P. Dib, K. Shah, N. Barraford, and B. Gallagher. Using led lighting for ubiquitous indoor wireless networking. In *Proceedings of WIMOB*, pages 373–378, 2008.

[15] Y. Yang, X. Chen, L. Zhu, B. Liu, and H. Chen. Design of indoor wireless communication system using leds. In *Proceedings of ACP*, pages 1–8, 2009.

[16] M. Rahaim, T. Borogovac, and J.B. Carruthers. Candles-communication and lighting emulation software. In *Proceedings of WiNTECH*, pages 9–14, 2010.

[17] T. Komine, J.H. Lee, S. Haruyama, and M. Nakagawa. Adaptive equalization system for visible light wireless communication utilizing multiple white led lighting equipment. *IEEE Transactions on Wireless Communications*, 8(6):2892–2900, 2009.

[18] K. Lee, H. Park, and J.R. Barry. Indoor channel characteristics for visible light communications. *IEEE Communications Letters*, 15(2):217–219, 2011.

[19] H. L. Minh, D. O'Brien, G. Faulkner, L. Zeng, K. Lee, D. Jung, and Y. Oh. 80 mbit/s visible light communications using pre-equalized white led. In *Proceedings of ECOC*, pages 1–2, 2008.

[20] H. L. Minh, D. O'Brien, G. Faulkner, L. Zeng, K. Lee, D. Jung, and Y. Oh. High-speed visible light communications using multiple-resonant equalization. *IEEE Photon. Tech. Lett.*, 20(14):1243–1245, 2008.

[21] H. Tanaka, Y. Umeda, and O. Takyu. High-speed led driver for visible light communications with drawing-out of remaining carrier. In *Proceedings of RWS*, pages 295–298, 2011.

[22] L. Zeng, D. O'Brien, H.L. Minh, K. Lee, D. Jung, and Y. Oh. Improvement of data rate by using equalization in an indoor visible light communication system. In *Proceedings of ICCSC*, pages 678–682, 2008.

[23] H. L. Minh, D. O'Brien, G. Faulkner, L. Zeng, K. Lee, D. Jung, Y. Oh, and E. T. Won. 100-mb/s nrz visible light communications using a postequalized white led. *IEEE Photonics Technology Letters*, 21(15):1063–1065, 2009.

[24] M.Z. Afgani, H. Haas, H. Elgala, and D. Knipp. Visible light communication using ofdm. In *Proceedings of TRIDENTCOM*, pages 129–134, 2006.

[25] H. Elgala, R. Mesleh, H. Haas, and B. Pricope. Ofdm visible light wireless communication based on white leds. In *Proceedings of VTC*, pages 2185–2189, 2007.

[26] S.C.J. Lee, J.W. Walewski, S. Randel, F. Breyer, H.P.A. van den Boom, and A.M.J. Koonen. Discrete multitone for novel application areas of optical communicaitons. In *Digest of the IEEE/LEOS Summer Topical Meetings*, pages 163–164, 2008.

[27] S.K. Hashemi, Z. Ghassemlooy, L. Chao, and D. Benhaddou. Orthogonal frequency division multiplexing for indoor optical wireless communications using visible light leds. In *Proceedings of CSNDSP*, pages 174–178, 2008.

[28] J. Vucic, C. Kottke, S. Nerreter, A. Buttner, K.D. Langer, and J.W. Walewski. White light wireless transmission at 200+ mb/s net data rate by use of discrete-multitone modulation. *IEEE Photonics Technology Letters*, 21(20):1511–1513, 2009.

[29] H. Elgala, R. Mesleh, and H. Haas. Indoor broadcasting via white leds and ofdm. *IEEE Transactions on Consumer Electronics*, 55(3):1127–1134, 2009.

[30] B. Inan, S.C.J. Lee, S. Randel, I. Neokosmidis, A.M.J. Koonen, and J.W. Walewski. Impact of led nonlinearity on discrete multitone modulation. *Journal of Optical Communications and Networking*, 1(5):439–451, 2009.

[31] I. Neokosmidis, T. Kamalakis, J.W. Walewski, B. Inan, and T. Sphicopoulos. Impact of nonlinear led transfer function on discrete multitone modulation: analytical approach. *Journal of Lightwave Technology*, 27(22):4970–4978, 2009.

[32] H. Elgala and R. Mesleh. Non-linearity effects and predistortion in optical ofdm wireless transmission using leds. *Int. J. Ultra Wideband Communicaitons and Systems*, 1(2):143–150, 2009.

[33] H. Elgala, R. Mesleh, and H. Haas. An led model for intensity-modulated optical communication systems. *IEEE Photonics Technology Letters*, 22(11):835–837, 2010.

[34] L. Zeng, D. O'Brien, H. L. Minh, G. E. Faulkner, K. Lee, D. Jung, Y. Oh, and E. T. Won. High data rate multiple input multiple output (mimo) optical wireless communications using white led lighting. *IEEE J. on Sel. Areas in Commun.*, 27(9):1654–1662, 2009.

[35] M. Akanegawa, Y. Tanaka, and M. Nakagawa. Baisc study on traffic information system using led traffic lights. *IEEE Trans. on Intelligent Transportation Systems*, 2(4):197–203, 2001.

[36] N Kumar, L N Alves, and R L Aguiar. Design and analysis of the basic parameters for traffic information transmission using vlc. In *Proc. of Wireless VITAE*, pages 798–802, 2009.

[37] I. E. Lee, M. L. Sim, and F. W. L. Kung. Performance enhancement of outdoor visible-light communication system using selective combining receiver. *IET Optoelectron*, 3(1):30–39, 2009.

[38] N. Kumar, D. Terra, N. Lourenco, L.N. Alves, and R.L. Aguiar. Visible light communication for intelligent transportation in road safety applications. In *Proceedings of IWCMC*, pages 1513–1518, 2011.

[39] M. Wada, T. Yendo, T. Fujii, and M. Tanimoto. Road-to-vehicle communication using led traffic light. In *Proceedings of the Intelligent Vehicle Symposium*, pages 601–606, 2005.

[40] H. Binti Che Wook, T. Komine, S. Haruyama, and Nakagawa M. Visible light communication with led-based traffic lights using 2-dimensional image sensor. In *Proc. of CCNC*, pages 243–247, 2006.

[41] S. Iwasaki, C. Premachandra, T. Endo, T. Fujii, M. Tanimoto, and Y. Kimura. Visible light road-to-vehicle communication using high-speed camera. In *Proc. of Intell. Veh. Symp.*, pages 13–18, 2008.

[42] T. Hara, S. Iwasaki, T. Yendo, T. Fujii, and M. Tanimoto. A new receiving system of visible light communication for ITS. In *Proceedings of the IEEE Intelligent Vehicles Symposium*, pages 474–479, 2007.

[43] S. Okada, T. Yendo, T. Yamazato, T. Fujii, M. Tanimoto, and Y. Kimura. On-vehicle receiver for distant visible light road-to-vehicle communication. In *Proceedings of the IEEE Intelligent Vehicle Symposium*, pages 1033–1038, 2009.

[44] W.P. Krug. Onboard wireless aerospace applications - challenges and opportunities. In *IEEE Photonics Society Summer Topical Meeting on Optical Wireless Systems and Applications*, 2012.

[45] T. Komine, S. Haruyama, and M. Nakagawa. Bidirectional visible-light communication using corver cube modulator. In *Proceedings of Wireless and Optial Communication*, 2003.

[46] D. O'Brien. Cooperation and cognition in optical wireless communications. In *Cognitive Wireless Networks: Concepts, Methodologies and Visions - Inspiring the Age of Enlightenment of Wireless Communications*. Springer, 2007.

[47] A. Zukauskas, M.S. Shur, and R. Gaska. *Introduction to Solid-State Lighting*. Wiley, New York, 2002.

[48] E F Schubert. *Light-Emitting Diodes*. Cambridge University Press, Cambridge UK, 2006.

[49] J.M. Kahn, W.J. Krause, and J.B. Carruthers. Experimental characterization of non-directed indoor infrared channels. *IEEE Trans. on Communications*, 43(2/3/4):1613–1623, 1995.

[50] F.J. Lopez-Hernandez, R. Perez-Jimenez, and A. Santamaria. Ray-tracing algorithms for fast calculation of the channel impuse response on diffuse ir wirelss indoor channels. *Opt. Eng.*, 39:2775–2780, 2000.

[51] J.B. Carruthers and P. Kannan. Iterative site-based modeling for wireless infrared channels. *IEEE Transactions on Antennas and Propagation*, 50:759–765, 2002.

[52] Z. Dong, K. Cui, G. Chen, and Z. Xu. Non-line-of-sight link performance study for indoor visible light communication systems. In *Proceedings of SPIE*, volume 7814, pages 781404–1 – 781404–10, 2010.

[53] S.B. Alexander. *Optical Communication Receiver Design*. SPIE Opt. Eng. Press/IEE, London UK, 1997.

[54] K. Cui, G. Chen, Q. He, and Z. Xu. Indoor optical wireless communication by ultraviolet and visible light. In *Proc. of SPIE*, volume 7464, pages 74640D–1 – 74640D–9, 2009.

[55] A.J.C. Moreira, Valadas R.T., and A.M. de Oliveira Duarte. Optical interference produced by artificial light. *Wireless Networks*, 3:131–140, 1997.

[56] R. Narasimhan, M.D. Audeh, and J.M. Kahn. Effect of electronic-ballast fluorescent lighting on wireless infrared links. *IEE Proceedings of Optoelectronics*, 143(6):347–354, 1996.

[57] M. Hauske, D. Shi, M. Ihle, and F.K. Jondral. Artificial lighting interference on free space photoelectric systems. In *International Symposium on Electromagnetic Compatibility*, 2009.

[58] Z. Xu and B.M. Sadler. Ultraviolet communications: potential and state-of-the-art. *IEEE Communications Magazine*, 46(5):67–73, 2008.

[59] C.R.A.T. Lomba, R.T. Valadas, and A.M. de Oliveira Duarte. Safety issues of the baseband IR PHY. In *IEEE802.11, doc:IEEE P802.11-94/174*, 1994.

[60] IEC825-1. *Safety of Laser Products - Part 1: Equipment Classification, Requirements, and User's Guide.* 1993.

[61] K. Cui, G. Chen, Z. Xu, and R. D. Roberts. Line-of-sight visible light communication system design and demonstration. In *Proceedings of CSNDSP*, pages 621–625, 2010.

[62] M. Kavehrad, Z. Hajjarian, and A. Enteshari. Energy-efficient broadband data communications using white leds on aircraft powerlines. In *Proceedings of ICNS*, pages 1–8, 2008.

[63] O. Gonzalez, R. Perez-Jimenez, S. Rodriguez, J. Rabadan, and A. Ayala. Adaptive ofdm system for communications over the indoor wireless optical channel. *IEE Proceedings-Optoelectronics*, 153:139–144, 2006.

[64] J. Armstrong and A.J. Lowery. Power efficient optical ofdm. *Electronics Letters*, 42:370–372, 2006.

[65] C. Ma, H. Zhang, M. Yao, Z. Xu, and K. Cui. Distributions of papr and crest factor of ofdm signals for vlc. In *Proceedings of Summer Topical Meeting on Optical Wireless Systems and Applications*, 2012.

[66] H. Ochiai and H. Imai. On the distribution of the peak-to-average power ratio in ofdm signals. *IEEE Transactions on Communicaitons*, 49(2):282–284, 2001.

[67] D. Gesbert, M. Shafi, D. Shiu, P.J. Smith, and A. Naguib. From theory to practice: an overview of mimo space-time coded wireless systems. *IEEE Journal of Selected Areas in Communications*, 21:281–302, 2003.

[68] S. Jivkova, B.A. Hristov, and M. Kavehrad. Power-efficient multispot-diffuse multiple-input-multiple-output approach to broad-band optical wireless communications. *IEEE Transactions on Vehicular Technology*, 53(3):882–889, 2004.

[69] S. Hranilovic and F.R. Kschischang. A pixilated mimo wireless optical communication system. *IEEE Journal of Selected Topics in Quantum Electronics*, 12:859–874, 2006.

[70] M. Garfield, C. Liang, T.P. Kurzweg, and K.R. Dandekar. Mimo space-time coding for diffuse optical communication. *Microwave and Optical Technology Letters*, 48:1108–1110, 2006.

[71] D. Tse and P. Viswanath. *Fundamentals of Wireless Communications*. Cambridge Univ. Press, Cambridge UK, 2005.

[72] T. Tran, Y. Shin, and O. Shin. Overview of enabling technologies for 3GPP LTE-advanced. *EURASIP Journal on Wireless Communications and Networking*, 2012(54), 2012.

[73] M. Yavuz, F. Meshkati, S. Nanda, A. Pokhariyal, N. Johnson, B. Raghothaman, and A. Richardson. Interference management and performance analysis of UMTS/HSPA+ femtocells. *IEEE Communications Magazine*, 47(9):102–109, 2009.

[74] D. Lopez-Perez, A. Valcarce, G. de la Roche, and J. Zhang. OFDMA femtocells: A roadmap on interference avoidance. *IEEE Communications Magazine*, 47(9):41–48, 2009.

[75] D. O'Brien, H. L. Minh, L. Zeng, G. Faulkner, K. Lee, D. Jung, Y. Oh, and E. T. Won. Indoor visible light communications: challenges and prospects. In *Proceedings of SPIE*, volume 7091, pages 709106–1 – 709106–9, 2008.

[76] G. W. Marsh and J. M. Kahn. Channel reuse strategies for indoor infrared wireless communications. *IEEE Trans. on Communications*, 45(10):1280–1290, 1997.

[77] J. M. G. Linnartz, L. Feri, H. Yang, S. B. Colak, and T. C. W. Schenk. Code division-based sensing of illumination contributions in solid-state lighting systems. *IEEE Trans. on Signal Processing*, 57(10):3984–3998, 2009.

[78] T. Kahn, M. Tahir, and A. Usman. Visible light communications using wavelength division multiplexing for smart spaces. In *Proceedings of CCNC*, 2012.

[79] Raymond C.V. Macario. *Cellular radio*. McGraw-Hill, Houndmills, 1997.

[80] V. G. Yanez, J. R. Torres, J. B. Alonso, J. A. R. Borges, C. Q. Sanchez, C. T. Gonzalez, R. P. Jimenez, and F. D. Rajo. Illumination interference reduction system for VLC communications. In *Proceedings of 11th World Sci. Eng. Acad. Soc.*, pages 252–257, 2010.

[81] R. Roberts, P. Gopalakrishnan, and S. Rathi. Visible light positioning: Automotive use case. In *Proceedings of VNC*, pages 309–314, 2010.

[82] C.G. Lee, S. Park, and M. Kang. Proposal of car-to-car message delivery over optical wireless communication link. *The Review of Laser Engineering*, 36:1320–1322, 2008.

[83] K. Cui, G. Chen, Z. Xu, and R.D. Roberts. Experimental characterization of traffic light to vehicle vlc link performance. In *Proceedings of GLOBECOM Workshops*, pages 808–812, 2011.

[84] R.E. Bird and C. Riordan. Simple solar spectral model for direct and diffuse irradiance on horizontal and tilted planes at the earth's surface for cloudless atmosphere. *Journal of Climate and Applied Meteorology*, 25:87–97, 1986.

[85] C. Chang, Y. Su, U. Kurokawa, and B. Choi. Interference rejection using filter-based sensor array in vlc systems. *IEEE Sensor Journal*, 12(5):1025–1032, 2012.

[86] R. Perez-Jimenez, J.A. Rabadan, and F.J. Lopez-Hernandez. Filtered modulation schemes for short distance infrared wireless communications. *IEEE Transactions on Consumer Electronics*, 46(2):275–282, 2000.

[87] T. Lee and A. Dentai. Power and modulation bandwidth of GaAs-AlGaAs high-radiance LED's for optical communication systems. *Journal of Quantum Electronics*, QE-14(3):150–159, 1978.

[88] N. Araki and H. Yashima. A channel model of optical wireless communication during rainfall. In *Proceedings of the 2nd Intern. Symp. on Wireless Commun. Sys.*, pages 205–209, 2005.

[89] M.A. Naboulsi, H. Sizun, and F. Fornel. Fog attenuation prediction for optical and infrared waves. *Optical Engineering*, 43(2):319–329, 2004.

[90] M. Araki, K. Ogawa, K. Wakamori, K. Kodate, and S. Ito. Measurement and simulation of the effect of snowfall on free-space optical propagation. *Applied Optics*, 47(31):5736–5743, 2008.

[91] M.D. Audeh and J.M. Kahn. Performance evaluation of L-pulse-position modulation on non-directed indoor infrared channels. In *Proceedings of SUPERCOMM/ICC*, volume 2, pages 660–664, 1994.

[92] Joint ISO/CIE Standard, ISO 16508:1999/CIE S006.1/E-1998. Road traffic lights - photometric properties of 200mm roundel signals. 1998.

.1 Derivation of the Useful Signal Component and Intracell Interference

$$Z_u + Z_{intracell} = \int_0^{T_b} \left(r_u(t) + r_{intracell}(t) \right) m(t) dt$$

$$= \alpha_1 \varepsilon_1 P_1 \sum_{k=1}^{K} \sum_{i=0}^{N-1} \sum_{j=0}^{N-1} \int_0^{T_b} c_{1,j}^{(1)} \lambda_{1,k} \psi_1(t - iT_c - e_{1,i}^{(k)} \delta_1)$$

$$\left[\psi_1(t - jT_c - \delta_1) - \psi_1(t - jT_c) \right] dt$$

$$= \alpha_1 \varepsilon_1 P_1 \sum_{k=1}^{K} \sum_{i=0}^{N-1} \sum_{j=0}^{N-1} \int_0^{T_b} c_{1,j}^{(1)} \lambda_{1,k} \left[\frac{1 + a_{1,i}^{(k)}}{2} \psi_1(t - iT_c - \delta_1) + \frac{1 - a_{1,i}^{(k)}}{2} \psi_1(t - iT_c) \right]$$

$$\left[\psi_1(t - jT_c - \delta_1) - \psi_1(t - jT_c) \right] dt$$

$$= \alpha_1 \varepsilon_1 P_1 \sum_{k=1}^{K} \sum_{j=0}^{N-1} \int_0^{T_b} \lambda_{1,k} \left[c_{1,j}^{(1)} \frac{1 + a_{1,j}^{(k)}}{2} \psi_1^2(t - jT_c - \delta_1) - c_{1,j}^{(1)} \frac{1 - a_{1,j}^{(k)}}{2} \psi_1^2(t - jT_c) \right.$$

$$\left. - c_{1,j}^{(1)} a_{1,j}^{(k)} \psi_1(t - jT_c - \delta_1) \psi_1(t - jT_c) \right] dt$$

$$= \alpha_1 \varepsilon_1 P_1 \sum_{k=1}^{K} \sum_{j=0}^{N-1} \lambda_{1,k} c_{1,j}^{(1)} a_{1,j}^{(k)} q_0^{(1)} \left(1 - R_0^{(1)} \right)$$

$$= \alpha_1 \varepsilon_1 P_1 \sum_{k=1}^{K} \sum_{j=0}^{N-1} \lambda_{1,k} c_{1,j}^{(1)} s_{1,\lfloor j/N \rfloor}^{(k)}{}' c_{1,j}^{(k)} q_0^{(1)} \left(1 - R_0^{(1)} \right)$$

$$= \alpha_1 \varepsilon_1 P_1 \sum_{k=1}^{K} \lambda_{1,k} s_{1,0}^{(k)}{}' q_0^{(1)} \left(1 - R_0^{(1)} \right) \sum_{j=0}^{N-1} c_{1,j}^{(1)} c_{1,j}^{(k)}$$

$$= \alpha_1 \varepsilon_1 P_1 \left(N s_{1,0}^{(1)} q_0^{(1)} \left(1 - R_0^{(1)} \right) + \sum_{k=2}^{K} \lambda_{1,k} s_{1,0}^{(k)}{}' q_0^{(1)} \left(1 - R_0^{(1)} \right) \sum_{j=0}^{N-1} c_{1,j}^{(1)} c_{1,j}^{(k)} \right).$$

$$(.1)$$

Here

$$Z_u = N \alpha_1 \varepsilon_1 P_1 s_{1,0}^{(1)}{}' q_0^{(1)} \left(1 - R_0^{(1)} \right),$$

$$Z_{intracell} = \alpha_1 \varepsilon_1 P_1 \sum_{k=2}^{K} \lambda_{1,k} s_{1,0}^{(k)}{}' q_0^{(1)} \left(1 - R_0^{(1)} \right) \sum_{j=0}^{N-1} c_{1,j}^{(1)} c_{1,j}^{(k)} = 0.$$

$$(.2)$$